Chiral Luttinger Liquids and Their Use in Detecting Quantum Discord

by

Matthew Antony Hunt

A thesis submitted to
The University of Birmingham
for the degree of
DOCTOR OF PHILOSOPHY

Theoretical Physics Group
School of Physics and Astronomy
The University of Birmingham

February 28, 2018

Abstract

In this thesis we investigate the physics of chiral Luttinger liquids found at the edge of a 2D material in the quantum Hall regime. We focus specifically on the edge modes found in the relativistic quantum Hall in graphene, where the number of species is larger than in conventional 2D semi-conductors. This leads to interesting dynamics of chiral modes along the interface of a graphene PN junction in a high magnetic field. We address a series of conflicting experiments within this system, and unify them into one model where the differences between the experiments originate from disorder. The high mobility of electrons in graphene, paired with additional degeneracies of the material, lead to it being an ideal material for the fabrication of a high quality electronic Mach-Zehnder interferometer (MZI). We investigate how a MZI in graphene may differ from those built in other 2D semi-conductors, with a focus on the additional interactions we expect to be present in graphene. We make use of the electronic MZI in a quantum information setting, specifically with regards to detecting quantum discord. Due to the nature of discord as a entropic measure, it has proved difficult to construct an experimental protocol to quantify (or even detect) its presence in a system. Based on the MZI, we propose a robust protocol for detecting quantum discord, from which we construct an experimentally accessible measure of discord. We demonstrate that our measure bares a strong resemblance to discord, whilst bypassing the difficulties associated with measurement of an entropic quantity.

Acknowledgements

I'd like to extend my gratitude to my supervisor, Prof. Igor Lerner, for not only his help in a technical sense with regard to work in this thesis, but also his encouragement both academically and with regard to other areas of life. I'd also like to thank Prof. Mike Gunn, Dr. Martin Long, Dr. Igor Yurkevich and Prof. Yuval Gefen for many fruitful discussions. Their advice caused me to avoid following many wrong turns and vastly improved my understanding of a variety of topics. I'd also like to thank the great many friends I have made during my time at Birmingham. Without them to blow off steam with, I'm not sure I would have ever finished this thesis. In particular, thanks to Jack Gartlan for his useful advice. A special mention goes to Bethany Wells, to whom I owe a huge debt for keeping me sane during my PhD. Her reassuring presence and helpful advice have been invaluable throughout the process. A final thanks goes to my parents and sister for their immense support not just throughout my PhD, but with everything prior to it.

Contents

List of Figures

Introduction

Motivation

Parts of this thesis may seem disconnected from each other, for example, what does the quantum information topic of *quantum discord* have to do with chiral Luttinger liquids in graphene? The thread which ties these topics together is the 1D emergent physics found at the edge of a 2D material in the quantum Hall regime [1, 2, 3]. The physics of the quantum Hall effect is one of the richest found in condensed matter, the fractional quantum Hall effect [4, 5] gave birth to the hugely popular concept of *Topological Order* in condensed matter [6], as well *Composite Fermion* theory [7] and provided the first observation of a particle with fractional statistics [4, 8]. Furthermore the quantum Hall effect provided a physical experimental system which demonstrated true one-dimensional physics, an area of research which had long been considered the refuge of self-indulgent theorists. It it this one dimensional character we are interested in in this thesis.

At the edge of a quantum Hall sample the electronic physics is analogous to the *Luttinger Model*, a model which is exactly solvable even in the presence of many interacting bodies. Furthermore the nature of the energy bands at a quantum Hall boundary means these excitations are restricted to travel in one direction (that is, they are *chiral*), making their dynamics very conceptually accessible. We are in-

terested in applying this physics to the *relativistic quantum Hall effect* found in graphene, with a particular motivation to understand how to build coherent electronic devices using these chiral modes. Graphene has extremely high electron mobilities [9] and an extra degree of freedom not seen in conventional semi-conductors [10] which makes it well suited to the fabrication of such devices [11]. One of the greatest successes of building electronic devices in standard semi-conductor quantum Hall research was the fabrication of the electronic Mach-Zehnder [12, 13]. We wish explore the physics of such a device in graphene with a particular focus on a recent experimental success in the area [11].

One of the ways an electronic Mach-Zehnder can be useful outside of standard interferometry is by using it as a qubit, which might lead one to think about its uses within the field of *quantum information*. We consider the quantum correlations exemplified by *quantum discord* with the Mach-Zehnder as a physical realisation. Quantum correlations were previously considered synonymous with entanglement [14], but it turns out that this is only part of the story. Discord describes a much more generic class of quantum correlations of which entanglement is only a small aspect of. Quantum discord has seen a flurry of interest since its conception in 2001 [15, 16]. It has had suggested uses in a variety of quantum information contexts including entanglement-free quantum computation [17, 18], which might be expected to be more robust to decoherence then its entangled counterpart [19]. In spite of this interest, even detection of the presence of discord has proved non-trivial [20]. This provides a huge incentive for fabrication of a solid state discord-based device, in the hopes that it may boost the quest for detection of discord and provide an experimentally accessible system for quantum information devices.

Outline

In the first chapter of this thesis we examine the rich and interesting physics of the chiral modes found at a quantum Hall edge. We investigate how, by linearising the dispersion relation, to generate a model which is exactly solvable even within the presence of interactions. This is the *Luttinger* model [21, 22]. We investigate how its excitations may be treated using a technique called *bosonisation* [23, 24]. These chiral edge modes prove to be useful in a practical sense, allowing the fabrication of a powerful tool of interferometry - the electronic Mach-Zehnder interferometer (MZI) [12, 13]. After considering these chiral edge modes in conventional semi-conductors we go on to consider similar physics in graphene in Chapter 2. The physics is even richer in this material, with new species of chiral modes emerging in graphene [10, 25] which allow for more control of these systems in a material with higher electron mobilities. Graphene PN junctions within the quantum Hall regime proves to be a particularly interesting experimental system. In Chapter 3, we discuss experiments that have occurred in high magnetic field PN junctions since its first fabrication a decade ago [26, 27, 28, 29, 11]. Many of these works appear to be in direct contradiction. This leads to the first major piece of original work of this thesis in which we consider a model with a variable parameter describing disorder along the PN junction interface. By adjusting this parameter we are able to describe all (apart from one) of the seemingly contradictory experiments within this model and predict further measurements to test its validity. The particular experiment [11] we fail to capture the specifics of, observed a Mach-Zehnder style oscillatory dependence. This leads us to the second piece of original work in which we consider the additional interactions that might be expected to factor into an MZI in graphene that were irrelevant in the more standard semi-conductor case. We build on the work of others [30, 31] to consider a MZI model which includes

these additional features. In Chapter 4 we introduce the topic of quantum discord [15, 16, 32], discussing its formulation and properties. We also bring to light the difficulties that have been found in detecting whether discord is present in a system. We then, in Chapter 5, return to the electronic Mach-Zehnder. The MZI presents itself as an experimentally achievable two level system (a qubit), the basis of most quantum information discussions. This leads to us utilising this system to propose an original method to generate a solid-state system with a controllable amount of quantum discord. Furthermore we design a protocol based on cross-correlation functions between two coupled electron Mach-Zehnders which is able to detect discord. We extract a new measure of discord from this protocol which appears to bare a striking resemblance to discord in the examples we consider. Finally, we address the robustness of our protocol by subjecting it to more realistic experimental conditions such as many-electron flow and finite temperature.

Chapter 1

Physics at the Edge

As explained in the introduction, the chiral modes found at the edge of a semi-conductor in a high magnetic field are at the heart of this thesis. With this being the case we allocate this starting chapter to background on the quantum Hall effect and the different types of physics that can be seen at the edge. Specifically, we focus on the methods used to exactly solve 1D problems even when interactions are present. We demonstrate the theory behind how edge states have allowed for the creation of the electronic analogue to the quantum optical Mach-Zehnder interferometer [12]. This will lead us into the next chapter in which we apply similar considerations to the *relativistic* quantum Hall effect in graphene, where we discuss the surprising differences between edge physics in conventional semi-conductors and that found in graphene.

1.1 The Quantum Hall Effect

Discovery of the *quantum Hall effect* won Klaus Von Klitzing [33] the Nobel prize in 1985, his experiment confirmed that the Hall conductivity in a two dimensional electron gas was quantised. He won the Nobel prize by demonstrating that this

quantisation was precise to 1 part in 10^7. This incredibly precise quantisation stems from the fact that under application of a strong magnetic the dispersion spectrum is broken up into non-dispersive energy bands, known as Landau levels, with a huge degeneracy. Any electrons added to the sample occupy these insulating bands and therefore do not contribute to conductance. Such behaviour may be seen by writing down the Hamiltonian for an electron confined to two dimensions (x-y plane) in a perpendicular magnetic field (z-direction). Its Hamiltonian is given by

$$\hat{H} = \frac{1}{2m}\big(\mathbf{p} - e\mathbf{A}\big)^2, \qquad\qquad \mathbf{B} = \nabla \times \mathbf{A}. \tag{1.1}$$

The perpendicular magnetic field can be enforced by any appropriate choice of vector potential. We choose the gauge most suited to rectangular samples of quantum Hall materials which we will consider later, the *Landau gauge* $\mathbf{A} = -By\hat{\mathbf{x}}$. This choice of gauge leaves the Hamiltonian (1.1) translationally invariant in the x-direction meaning that momentum should be conserved in this direction and the plane wave ansatz for the wave function is appropriate [34],

$$\psi(x, y) = \frac{1}{\sqrt{L}} e^{ikx}\phi(y), \tag{1.2}$$

where L is the length of the sample in the x-direction. In which case Schrödinger's equation reduces to the following,

$$\left[\frac{p_y^2}{2m} + \frac{m\omega_c^2}{2}(y - y_0)^2\right]\phi(y) = \epsilon\phi(y), \qquad\qquad y_0 \equiv kl_B^2, \tag{1.3}$$

where the magnetic length is given by $l_B \equiv \sqrt{\hbar/eB}$ and the classical cyclotron frequency is defined as $\omega_c \equiv eB/m$. Ergo, the problem reduces to that of a series of degenerate harmonic oscillators centred on $y \equiv kl_B^2$ [35]. Eq. (1.3) can be solved using well known methods (e.g [36]) to give the the energy spectrum and wave

functions as below,

$$\epsilon_n = \left(n + \frac{1}{2}\right)\hbar\omega_c, \qquad \phi_n(y) = \exp\left(-\frac{(y-y_0)^2}{2l_B^2}\right) H_n\left(\frac{y-y_0}{l_B}\right), \tag{1.4}$$

where $H_n(\xi)$ are the Hermite polynomials with appropriate normalisation. Eq. (1.4) describe a series of flat energy band separated by $\hbar\omega_c$ (Landau levels). Essentially the electron states in the material are split into a series of harmonic wells with degenerate energies. The degeneracy of the bands is manifest in the lack of dependence on k in ϵ_n, this degeneracy can be approximated [37] from the number of harmonic traps which 'fit' into the sample by noting that the spacing between neighbouring states in k-space is given by $\Delta k = 2\pi/L$, which translates to neighbouring harmonic traps being separated by $\Delta y = \Delta k l_B^2 = 2\pi l_B^2/L$. Considering our rectangular quantum Hall material to have a width W in the y-direction, the number of available states is $N = W/\Delta y = A \times B\frac{e}{\hbar}$, where A in the area of the material i.e the degeneracy is equivalent to the number of flux quanta threading the sample.

The above gives a good description of what is seen in the bulk of a material in the quantum Hall regime. To describe the edges of the sample we also need to consider the effects a confinement potential has on an electron. We consider a rectangular 2D material in which the length in the x-direction is much larger than the width in the y-direction (and both lengths are much larger than than the magnetic length, $l_B \ll W \ll L$), in which case we can consider a confinement potential at the edges which is only y-dependent, $V(y)$. The model therefore maintains translational invariance in the x-direction and the Landau gauge chosen earlier, as well as the ansatz Eq. (1.2), are still good choices. The remaining Hamiltonian, including

the confinement potential, is given by,

$$\hat{H} = \frac{p_y^2}{2m} + \frac{1}{2}m\omega_c^2(y - y_0)^2 + V(y). \tag{1.5}$$

If we consider a potential which varies slowly ($\partial_y V(y) \ll \hbar\omega_c/l_B$) we may approximate the potential with its value at the centre of each of the harmonic states Eq. (1.4), y_0 [3]. This results in k-dependent (and therefore dispersive) energy bands described by,

$$\epsilon_{n,k} = \hbar\omega_c\left(n + \frac{1}{2}\right) + V(kl_B^2). \tag{1.6}$$

Assuming $V(y)$ monotonically increases as we approach an edge, $\epsilon_{n,k}$ must also monotonically increase with k, meaning $\partial\epsilon/\partial k$ is non-zero and of the same sign for all states close to a given edge. The electrons near the edge are therefore conductive and chiral. These edges will be predominant part of the quantum Hall effect that is of interest in this thesis, we therefore focus in on this part of the spectrum by linearising the energy spectrum about this point. Consider a situation in which the system is doped such that the Fermi energy, ϵ_F, sits between Landau levels but bisects some of the energy bands where $V(l_B^2 k)$ is non-zero. Providing the temperature is far less than the Landau level spacing (i.e, $k_B T \ll \hbar\omega_c$) we may expand Eq. (1.6) about the Fermi momentum of the excitations belonging to each band, k_{F_n}

$$\epsilon_{n,k} = \hbar\omega_c\left(n + \frac{1}{2}\right) + V(l_B^2 k_{F_n}) + \frac{1}{l_B^2}\frac{\partial V(kl_B^2)}{\partial k}\bigg|_{k=k_{F_n}}(k - k_{F_n})l_B^2 + ..., \tag{1.7}$$

where the Fermi momentum for the nth band is determined by $\epsilon_F = \hbar\omega_c(n + 1/2) + V(l_B^2 k_{F_n})$. Since $V(y_0)$ is always positive this equation also determines the number of energy bands which are accessible at the Fermi energy. If we assume only the states close to the Fermi level are relevant (those far above the Fermi energy are

inaccessible, whilst those far below are Pauli blocked), we may keep only terms up to those linear in $k - k_{F_n}$ in Eq.(1.7). Resetting the zero of the energy, $\epsilon_{n,k} \to \epsilon_{n,k} - \epsilon_F$ gives a spectrum of the form,

$$\epsilon_{n,k} \approx \hbar v_{Fn}(k - k_{Fn}), \tag{1.8}$$

where $v_{F_n} = \frac{1}{\hbar}\partial V(l_B^2 k)/\partial k\big|_{k=k_F}$. This linearisation process which takes us from Eq. (1.6) to Eq. (1.8) is illustrated in Fig. 1.1, for just the $n = 0$ Landau level.

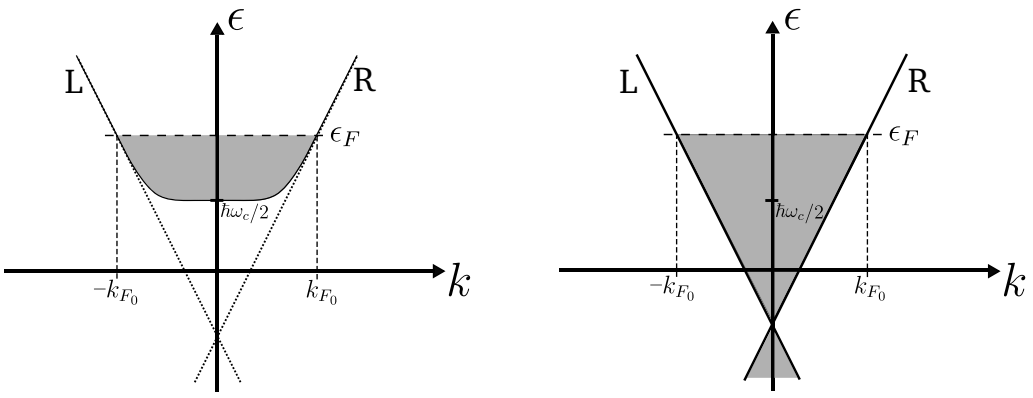

Figure 1.1: On the left is a sketch of the energy spectrum given by Eq. (1.6) where only the zeroth Landau level is shown, the spectrum is flat in the centre but bent upwards by $V(l_B^2 k)$, the grey proportion represents filled electronic states. The right image shows a sketch of the linear spectrum Eq. (1.8), we assume the two spectra have the same dynamics when the energy is close to ϵ_F, but are careful to note that by performing this linearisation we have introduced an infinite amount of negative energy states. This idea of linearisation of the energy spectrum to simplify the problem is one that is borrowed from the Luttinger-Tomonaga model [21, 22] which we will discuss in Section 1.3. L and R represent left and right movers.

We may then write down the fermionic Hamiltonian that satisfies the energy spectrum in Eq. (1.8)

$$H = \sum_{k,n} \hbar v_{F_n}(k - k_{F_n})\, c^\dagger_{k,n} c_{k,n} \tag{1.9}$$

where the fermionic exchange statistics are enforced by the anti-commutations of the operators,

$$\{c_i, c_j^\dagger\} = \delta_{ij}, \qquad \{c_i^\dagger, c_j^\dagger\} = \{c_i, c_j\} = 0. \tag{1.10}$$

There is one further subtlety that must be discussed, in Fig. (1.1) we see that when we linearise the spectrum we also introduce an infinite number of electron states. This means that acting the Hamiltonian (1.9) on the state which is filled to the Fermi level will return an infinite solution. To correct for this we must *normally order* our operators in order to correct for the infinities we introduced. We use the notation : : to mean subtraction of the vacuum expectation value e.g,

$$: c_k^\dagger c_k := c_k^\dagger c_k - \langle \Omega | c_k^\dagger c_k | \Omega \rangle \,, \tag{1.11}$$

$c_k^\dagger c_k$ may be replaced by any combination of fermionic operators here. $|\Omega\rangle$ defines the vacuum where each state up to the Fermi energy is filled, i.e $c_k |\Omega\rangle = 0$ for $k > k_F$ and $c_k^\dagger |\Omega\rangle = 0$ for $k \leq k_F$. This allows us to define a well behaved Hamiltonian as,

$$H_0 = \sum_{k,n} \hbar v_{F_n} (k - k_{F_n}) \ : c_{k,n}^\dagger c_{k,n} : \tag{1.12}$$

Resetting the zero of k to k_F and Fourier transforming to real space we produce the representation,

$$H_0 = -i \sum_n \hbar v_{F_n} \int dx \ : \psi_n^\dagger(x) \partial_x \psi_n(x) : \tag{1.13}$$

We are left with the Hamiltonian describing a one-dimensional n-species chiral Fermi liquid. Note that up to this point we've only considered one side of the Hall bar. One anticipates a full symmetry on the other side of the sample with the exception that

the confining potential acts in the opposite direction and therefore $v_{F_n} \to -v_{F_n}$ on the other edge. This gives us the partner left-mover to the right-mover described by (1.9). Since we will always consider situations where these left and right movers are separated by a large spatial difference, the two species may never communicate and therefore they are best thought of as two separate 1D *chiral* Fermi liquids. Unlike in standard 1D problems this interaction-less Fermi liquid description is usually considered a good one for low energy properties of quantum Hall edges [38, 39, 40, 6]. This is a result of the fact that interactions can only lead to forward scattering in a chiral 1D electron fluid and therefore only results in a, usually irrelevant, phase. In some systems this phase will be relevant however and we will see that interactions must be taken into account else the results of the model will fail to explain experiments, such a scenario is seen in the case of the *electronic Mach-Zehnder Interferometer* [13] which we will discuss in the next section.

1.2 Mach-Zehnders in Condensed Matter

From the one-dimensional electronic states given by Eq. (1.13), we may construct a Mach-Zehnder type system by inducing tunnelling between two points along the one dimensional channels. At the first of these we anticipate an electron will be put into a superposition; at the second the states recombine and we expect interference. This can be achieved (and has been by several groups [12, 13, 41, 42]) by cutting a Hall bar into the following geometry: one may use top gates to push two edges states close enough together that an electron can tunnel between the two points. The Hamiltonian describing the system depicted in Fig. (1.2) for non-interacting electrons is given by two copies of freely propagating chiral electrons,

$$H_0 \equiv -i\hbar v_F \sum_m \int dx \ : \psi_m^\dagger(x)\partial_x\psi_m(x) : . \tag{1.14}$$

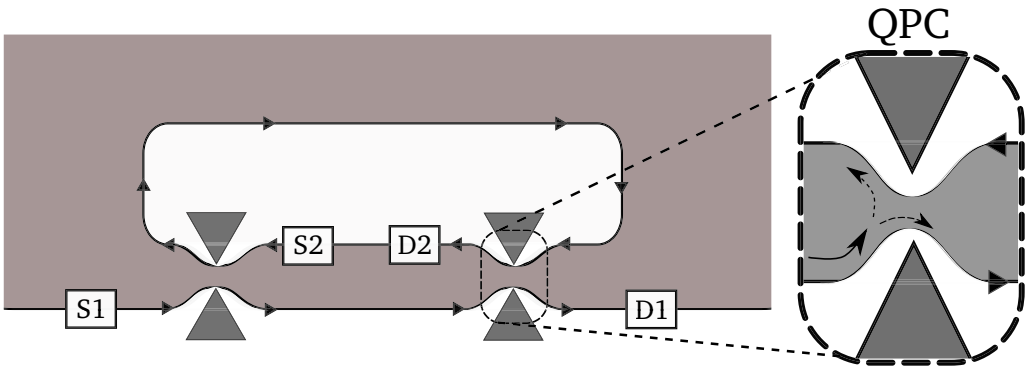

Figure 1.2: A block of 2D material in the quantum Hall regime with a section cut out, edge states are formed at all edges. We apply electrodes at $S1$ and $S2$ to act as sources and at $D1$ and $D2$ to act as drains. The grey triangles represent applied voltages which push the edge states further into the material and allow for tunnelling between edges - these are quantum point contacts (QPCs).

Then the tunnelling may be described by addition of a tunnelling Hamiltonian at the two QPC's which we assume to be point-like [43, 30],

$$H_{\text{tun}} \equiv \Gamma_a \psi_1^\dagger(0)\psi_2(0) + \Gamma_b \psi_1^\dagger(l_1)\psi_2(l_2) + \text{h.c}, \tag{1.15}$$

where $x = 0$ is the position of the first QPC on each arm, and $x = l_m$ is the position of the second QPC on arm-m. The full description of a non-interacting Mach-Zehnder is then given as $H = H_0 + H_{\text{tun}}$. This Hamiltonian can be diagonalised by incorporating the tunnelling terms into the eigenstates, we consider a wave function which freely propagates in all 3 regions away from the QPCs,

$$\psi_m(x) = \frac{1}{\sqrt{L}} \sum_k e^{ikx} \begin{cases} a_{k,m} & x < 0, \\ b_{k,m} & 0 < x < l_m, \\ c_{k,m} & l_m < x. \end{cases} \tag{1.16}$$

Then the tunnelling is included via a scattering matrix which relates the different fermionic operators,

$$\mathbf{b}_{k,m} = \mathcal{S}_a \mathbf{a}_{k,m}, \qquad \mathbf{c}_{k,m} = \mathcal{S}_b \mathbf{b}_{k,m}, \tag{1.17}$$

$$\mathcal{S}_a = \begin{pmatrix} r_a & t_a \\ -t_a^* & r_a \end{pmatrix}, \qquad \mathcal{S}_b = \begin{pmatrix} r_b & t_b \\ -t_b^* & r_b \end{pmatrix}, \tag{1.18}$$

with r_c and t_c $(c = a, b)$ describe the probability amplitude of an electron being reflected and transmitted respectively at QPC-c. The scattering matrices are assumed to be lossless $\mathcal{S}_c^\dagger \mathcal{S}_c = \mathbb{1}$ and k-independent. The first of these constraints mean that we anticipate no leaking of electrons to the environment at these points. We can choose the reflection coefficient to be real without loss of generality. Substituting into the Hamiltonian we can determine the coefficients of the scattering matrix are given by [44],

$$r_c = \frac{\left[(2\hbar v_F)^2 - |\Gamma_c|^2\right]}{\left[(2\hbar v_F)^2 + |\Gamma_c|^2\right]}, \qquad t_c = \frac{4i\hbar v_F \Gamma_c}{\left[(2\hbar v_F)^2 + |\Gamma_c|^2\right]}, \tag{1.19}$$

with $c = a, b$. There may be effects of different phase gains between the arms which may come from different accumulated orbital phases (i.e one arm of the interferometer is longer than the other) or the Aharonov-Bohm effect coming from the effect of flux penetrating the sliced out bit of our quantum Hall bar which sits between the two trajectories. We may include these by the shift $t_b \to t_b e^{i\phi}$ [45], with $\phi = k(\Delta l) + \Phi_{AB}$, $\Phi_{AB} = 2\pi \frac{\Phi}{\Phi_0}$ with $\Delta l = l_1 - l_2$ and Φ is magnetic flux penetrating the material and Φ_0 $(= \hbar/e)$ is the flux quantum. Note, that this does bring a k-dependence into the scatterer $\mathcal{S}_b$, albeit only in terms of a phase. The time dependence of the operators is then just that of the free fermion time evolution $a_{k,m}(t) = e^{-iv_F kt} a_{k,m}$. This formalisation can then be used to calculate expectation values, such as the current at the drains $(D1, D2)$ given some voltage bias at the

sources $(S1, S2)$. We will generally only consider one of the sources to be biased as this is usually the choice experimentally and, in any case, it is only the difference in voltages that will be relevant we will therefore take $V_1 - V_2 = V$, where V_1, V_2 are the voltages at $S1, S2$ respectively. The current operator takes a particularly simple form for a linear energy spectrum. Current measurement at a position x and time t in arm-m is given by

$$I_m(x,t) = ev_F : \psi_m^\dagger(x,t)\psi_m(x,t) :, \tag{1.20}$$

where we are again careful to normally order the operator with respect to the ground state to avoid unfortunate divergences. As an explicit example consider the current at the drain $D1$, which sits at x_0 on arm-1 (with $x_0 > l_1$). We represent the current operator as in Eq. (1.20) and the fermionic operators as in Eq. (1.16), and measurement time is taken at $t = 0$.

$$\langle I_1(x_0,0)\rangle = ev_F \frac{1}{L} \sum_{k_1,k_2} \langle : c_{1,k_1}^\dagger c_{1,k_2} : \rangle \, e^{i(k_2-k_1)x_0}. \tag{1.21}$$

We use the scattering matrices formulated in Eq. (1.18) to relate these fermionic operators to the ones at the sources.

$$\langle I_1(x_0,0)\rangle = ev_F \frac{1}{L} \sum_{k_1,k_2} \sum_{\alpha,\beta=1}^{2} \mathcal{A}_{\alpha 1}^\dagger \mathcal{A}_{1\beta} \, \langle : a_{\alpha,k_1}^\dagger a_{\beta,k_2} : \rangle \, e^{i(k_2-k_1)x_0}, \tag{1.22}$$

where $\mathcal{A}_{\alpha\beta}$ refers to the α, β elements of the transfer matrix $\mathcal{A} = \mathcal{S}_b \mathcal{S}_a$ which take us from the electron operators at the source to those at the drain. The a_k-operators are uncorrelated between different arm-spaces and momentum states; this reduces

Eq. (1.22) to,

$$\langle I_1(x_0,0)\rangle = ev_F\frac{1}{L}\sum_k\sum_{\alpha=1}^{2}\mathcal{A}^\dagger_{\alpha 1}\mathcal{A}_{1\alpha}\left\langle :a^\dagger_{\alpha,k}a_{\alpha,k}:\right\rangle . \tag{1.23}$$

We now make use of the assumption that the electrons at the sources are emitted from thermal reservoirs at different voltage biases, $V_1 = V$ and $V_2 = 0$. This assumption gives us that the expectation of the number operator $(a^\dagger_k a_k)$ are given by Fermi-Dirac distributions $\langle a^\dagger_{m,k}a_{m,k}\rangle = f_{\mu_m}(\hbar v_F k) \equiv f(\hbar v_F k - \mu_m)$ where $\mu_1 = eV$, $\mu_2 = 0$. The Fermi distribution is given by $f(x) \equiv (e^{\beta x}+1)^{-1}$ with $\beta = 1/k_B T$. Since we only consider arm-1 to be biased, the $\alpha = 2$ term in (1.23) is immediately killed by the vacuum contribution coming from normal ordering, and we only need to consider the $\alpha = 1$ part.

$$\langle I_1(x_0,0)\rangle = ev_F\frac{1}{L}\sum_k|\mathcal{A}_{11}|^2\big[f_{eV}(\hbar v_F k) - f_0(\hbar v_F k)\big], \tag{1.24}$$

where, $|\mathcal{A}_{11}|^2 = |r_a r_b - t_a t_b^* e^{\Phi_{AB}+k(l_1-l_2)}|^2$ and describes the probability that an electron with momentum k at $S1$ propagates to $D1$. To perform the summation over k we replace it with an energy integral $1/L\sum_k \to 1/(2\pi\hbar v_F)\int dE$. Then perform the different integrals in Eq. (1.24) using the identities in Appendix A.

$$\langle I_1(x_0)\rangle = \frac{eV}{h}\left[|r_a|^2|r_b|^2 + |t_a|^2|t_b|^2 - 2|r_a r_b t_a t_b^*|K(V,T)\cos\left(\Phi_{AB} + \frac{eV\Delta l}{2\hbar v_F}\right)\right], \tag{1.25}$$

with $K(V,T) = \frac{2\pi k_B T\sin\left(eV\Delta l/2\hbar v_F\right)}{eV\sinh(\pi k_B T\Delta l/\hbar v_F)}$, and we use $I(x_0) \equiv I(x_0,0)$. The features of the current are therefore dependent on ratio of three energy scales, the energy related to the potential bias eV, the thermal energy scale $\pi k_B T$ and the characteristic energy scale of the MZI, $E_c = 2\hbar v_F/\Delta l$. Most of the experiments we will consider are in the regime where $eV/k_B \sim 100mK$-$10mK$, $T \sim 1K$. The final scale proves slightly more tricky to broadly estimate since the velocity here is very dependent

on the confinement potential used (as well as the magnetic field) which can vary by a large degree between different experiments, we assume the velocity falls within the bounds given by several experimental measurements, $v \sim 10^4 ms^{-1}$-$10^5 ms^{-1}$ [41, 46, 47] and further assume that Δl is on the same scale as the whole experimental set-up which is of the order of μm, giving the natural thermal scale of the Mach-Zehnder of $E_c/k_B \sim 1K$-$100mK$.

We encounter some problems when we compare this to experiments performed on electronic MZIs however. These problems are easiest seen by considering the visibility of the differential conductance. The differential conductance is given by $\sigma(V) \equiv dI(V)/dV$ and its *visibility* describes the degree to which interference can be observed in it,

$$\mathcal{V}_\sigma[\Phi_{AB}] \equiv \frac{\sigma_{\max} - \sigma_{\min}}{\sigma_{\max} + \sigma_{\min}}, \tag{1.26}$$

where the optimisation is taken over Φ_{AB} i.e, the visibility describes the amplitude of oscillation with Φ_{AB}. One therefore obtains from Eq. (1.25) [30],

$$\mathcal{V}_\sigma[\Phi_{AB}] = \frac{2|r_a r_b t_a t_b^*|}{|r_a|^2|r_b|^2 + |t_a|^2|t_b|^2} \frac{\pi k_B T/E_c}{\sinh(\pi k_B T/E_c)}. \tag{1.27}$$

We see in the visibility the damping of the oscillation at high temperatures ($\pi k_B T \gg E_c$) as a result of thermal smearing, a feature which is notably absent, however, is any dependence on the voltage bias. In fact in the single particle picture we expect no dependence of this visibility on the voltage bias. Whilst this picture seems to be an accurate one in the limit $eV \ll E_c$, this is not what is seen experimentally outside of this regime [41, 13, 48, 49]. Thehese experiments show that the visibility oscillates with a dependence on V, with the interference disappearing entirely for some particular choices. The energy scale given by where the first minimum emerges

is roughly in the region of $10\mu V$ which is of approximately the same energy scale as E_c [50, 31]. This result lead to an array of theoretical papers [30, 51, 52, 53] trying to explain the results. The general consensus of these papers is the extra beating of the visibility was a result of interactions between the electrons within the arms. These papers aren't in complete agreement on which exact aspect of interaction is most important, and none seem to be able to wholly explain the effect.

The many-body effects that interactions bring in make the problem harder to solve, as seen from Eq. (1.29) they bring terms into the Hamiltonian that are density-density like. This means the full Hamiltonian is no longer quadratic in the electron operators.

$$H_{\text{int}} \equiv \int\int dxdx' \ :\psi^\dagger(x)\psi(x)U(x-x')\psi^\dagger(x')\psi(x'):, \tag{1.28}$$

$$\equiv \int\int dxdx' \ :\rho(x)U(x-x')\rho(x'): . \tag{1.29}$$

Fortunately bringing interactions into our 1D Fermi liquid model gives the well known Luttinger model, this model has the benefit that the natural interacting fermionic excitations can be mapped onto a free boson model. This model is completely quadratic in the bosonic operators and therefore entirely solvable. This process is called bosonisation and we will explore its construction in the next section.

1.3 Luttinger Liquids - Many Body Physics

The concepts discussed in Section 1.1, in which we examined the low energy properties of a one dimensional system via linearising its spectrum, is not a new one. A model in which the linearised Hamiltonian is taken as exact and interactions are

included is known as the Luttinger model [21]. The benefit of using the Luttinger model is that it is exactly solvable even with interactions. This solubility is not obvious when the Hamiltonian is written in the original fermionic operators where the model is clearly non-quadratic, see Eq. 1.29. It can, however, be shown that the problem can be mapped onto a free bosonic Hamiltonian, enabling us to find an exactly solvable form. This technique is known as *bosonisation* and is the product of successive works by a number of contributors [21, 54, 55, 56, 57, 58]. The bosonisation technique is one of the most useful tools that exist in handling 1D electronic physics, as such it will be the subject of the rest of this chapter.

1.3.1 Bosonisation

To convert our fermionic Hamiltonian into a bosonic one we utilise the work of von Delft and Schoeller [24] who wrote a particularly accessible review (*Bosonisation for Beginners*) based on the methods created by Haldane [58] and subsequent advancements in the area. Bosonisation aims to map all excitations in our fermionic system to ones which are bosonic in nature. To do so we start by spliting our Fock space into a direct sum of Hilbert spaces with fixed particle number N. Within these fixed number Hilbert spaces the only excitations that can occur are particle-hole ones, these are density-type terms and therefore boson-like. This leads to a complete representation of the excitations with a specific N which are purely bosonic. Finally we make use of *Klein operators* which act as ladder operators to move us between different fixed number Hilbert spaces, this allows us to create a complete representation of all excitations in Fock space in bosonic form.

1.3.2 Fixed Particle Number excitations

$|\overrightarrow{N}\rangle_0$ describes the ground state for an $\overrightarrow{N}$-particle system where $\overrightarrow{N} = (N_1, N_2, ..., N_M)$ where M is the total number of species and N_i is the number of particles of species i. 'Species' could, for example, describes our different Landau level indices or spin. We describe a $\overrightarrow{N}$-particle Hilbert space as a space in which the particle number of each species is fixed. In such a Hilbert space $|\overrightarrow{N}\rangle_0$ has no excitations, then to create an excitation we act some combination of particle-hole operators on it. I.e. providing we restrict ourselves to keep $\overrightarrow{N}$ constant all excitations are density like, we therefore attempt to build bosonic operators similar to density operators but with a normalisation chosen ($n_q = qL/2\pi$) so that they form bosonic commutation relations,

$$b^\dagger_{q,\eta} \equiv \frac{i}{\sqrt{n_q}} \sum_{k=-\infty}^{\infty} c^\dagger_{k+q,\eta} c_{k,\eta}, \qquad b_{q,\eta} \equiv \frac{-i}{\sqrt{n_q}} \sum_{k=-\infty}^{\infty} c^\dagger_{k-q,\eta} c_{k,\eta}, \tag{1.30}$$

$$[b_{q,\eta}, b^\dagger_{q',\eta'}] = \delta_{\eta,\eta'}\delta_{q,q'} \qquad [b_{q,\eta}, b_{q',\eta'}] = [b^\dagger_{q,\eta}, b^\dagger_{q',\eta'}] = 0, \tag{1.31}$$

Whilst it is not obvious all excitations on $|\overrightarrow{N}\rangle_0$ can be represented using the above operators Haldane [23] was able to prove that this is indeed the case for the linear Hamiltonian: by computing the grand partition function of the Hamiltonians in both the original fermionic and these new bosonic variables, he showed they are indeed equal and the representation is therefore complete. At this point it is useful to introduce bosonic field operators,

$$\varphi_\eta(x) \equiv -\sum_{q>0} \frac{1}{\sqrt{n_q}} e^{-iqx} b_{q,\eta} e^{-\epsilon q/2}, \qquad \varphi^\dagger_\eta(x) \equiv -\sum_{q>0} \frac{1}{\sqrt{n_q}} e^{iqx} b^\dagger_{q,\eta} e^{-\epsilon q/2}, \tag{1.32}$$

where ϵ is an infinitesimal constant included to regularise $q \to \infty$ divergences. We

also define their Hermitian combination,

$$\phi_\eta(x) \equiv \varphi_\eta(x) + \varphi_\eta^\dagger(x) = -\sum_{q>0} \frac{1}{\sqrt{n_q}} \big(e^{-iqx} b_{q,\eta} + e^{iqx} b_{q,\eta}^\dagger\big) e^{-\epsilon q/2}. \tag{1.33}$$

This field operator is particularly useful since we can define the normally ordered electron density easily from it,

$$\begin{aligned}
\rho_\eta(x) \equiv :\psi_\eta^\dagger(x)\psi_\eta(x): &= \frac{1}{L}\sum_q e^{-iqx} \sum_k :c_{k-q,\eta}^\dagger c_{k,\eta}:, \\
&= \frac{1}{L}\sum_{q>0} i\sqrt{n_q}\big(e^{-iqx} b_{q,\eta} - e^{iqx} b_{q,\eta}^\dagger\big) + \frac{1}{L}\sum_k :c_{k,\eta}^\dagger c_{k,\eta}:, \\
&= \frac{1}{2\pi}\partial_x \phi_\eta(x) + \frac{1}{L}\hat{N}_\eta, \qquad \text{(for } a \to 0\text{)}.
\end{aligned} \tag{1.34}$$

Equipped with the knowledge that we may represent all our excitations in terms of our bosonic variables we look to find this representation of Hamiltonian. We do so by utilising the fact that the properties of operators are fixed by their commutation relations [59]. If we can generate a Hamiltonian in terms of our bosonic variables which has the same commutation relation as when we consider the commutation with the fermionic Hamiltonian, the properties of the model must be the same.

$$[H_{0,\eta}, b_{q,\eta'}^\dagger] = \hbar v_F q \; b_{q,\eta}^\dagger \delta_{\eta,\eta'}, \tag{1.35}$$

the above implies an alternative representations of the Hamiltonian as $\sum_{q>0} \hbar v_F q \; b_{q,\eta}^\dagger b_{q,\eta}$ as well as additional terms which commute with $b^\dagger$. These additional terms can be

set by looking at the ground state energy,

$$E_{0,\eta}^{\overrightarrow{N}} = {}_0\langle\overrightarrow{N}|\, H_{0,\eta}\,|\overrightarrow{N}\rangle_0 = \frac{2\pi\hbar v_F}{L}\begin{cases}\sum_{n=1}^{N_\eta} n, & \text{if } N_\eta \geq 0,\\ -\sum_{n=N_\eta+1}^{0} n, & \text{if } N_\eta < 0,\end{cases} \tag{1.36}$$

$$= \frac{\pi\hbar v_F}{L} N_\eta(N_\eta+1). \tag{1.37}$$

These elements together gives us the bosonic Hamiltonian as,

$$H_{0,\eta} = \sum_{q>0} \hbar v_F q\; b_{q,\eta}^\dagger b_{q,\eta} + \frac{\pi\hbar v_F}{L} N_\eta(N_\eta+1), \tag{1.38}$$

$$= \int_{-L/2}^{L/2} dx\; \frac{\hbar v_F}{4\pi}\big(\partial_x\phi_\eta(x)\big)^2 + \frac{\pi\hbar v_F}{L} N_\eta(N_\eta+1), \tag{1.39}$$

$$= \pi\hbar v_F \int_{-L/2}^{L/2} dx\; \rho_\eta^2(x) + \frac{\pi\hbar v_F}{L} N_\eta, \tag{1.40}$$

where the second and third lines are found by substituting in Equations (1.33) and (1.34) respectively. Note that the cross terms of the form $\partial_x\phi_\eta(x)N_\eta$, originating from when we plug Eq. (1.34) into Eq. (1.40), are killed upon integration due to the periodicity of $\phi_\eta(x)$. We therefore end up with a representation of the Hamiltonian which is quadratic in density, since this is also the case for the interaction terms we arrive at a fully quadratic, and entirely solvable, Hamiltonian.

The above description is completely sufficient for any Hamiltonian which commutes with the particle number operator for each species. As interaction terms are particle number conserving, the above is (in general) sufficient even when these terms are present. When terms which can change particle number are introduced (such as those found in H_{tun}, Eq. (1.15)) we require an additional feature to increase the scope from the fixed particle Hilbert space, which the above description is valid for,

to enable us to span the entirety of Fock space. To do so we construct *Klein Operators*, ladder operators which take us between different fixed particle Hilbert spaces. These are often ignored as they are irrelevant for many purposes. They will prove to very important to the interacting Mach-Zehnder model however, and will also allow the conversion from fermionic to bosonic variables to be made entirely explicit.

1.3.3 Klein Operators

We wish to build ladder operators which have two properties, firstly these operators add (remove) one fermion of species η to (from) the lowest available momentum state, secondly we require they commute with the bosonic operators [24, 23]. This translates to mean that no matter the excitations of a particular state on which we act Klein operator on, it simply adds an electron to the lowest available state and the bosonic excitations are recreated on top of this. The first of our requirements can be satisfied for the ground state with the operator,

$$c^\dagger_{k_{N_\eta+1},\eta} \equiv \sum_k c^\dagger_{k,\eta}\delta(k - \frac{2\pi}{L}(\hat{N}_\eta + 1)) \tag{1.41}$$

$$= \frac{1}{L}\int_{-L/2}^{L/2} dx e^{i\frac{2\pi}{L}\hat{N}_\eta x}\left[\sum_k e^{-ikx}c^\dagger_{k,\eta}\right] \tag{1.42}$$

This works as desired when we act it on the vacuum. It doesn't, however, correctly fulfil the desired commutation relations, i.e if we choose our Klein operator $F^\dagger_\eta = c^\dagger_{k_{N_\eta+1}}$ it does not satisfy Eqs. (1.43), meaning that the operator acts differently on an excited state than it does on the ground state.

$$[b_{q,\eta}, F^\dagger_{\eta'}] = [b^\dagger_{q,\eta}, F^\dagger_{\eta'}] = [b_{q,\eta}, F_{\eta'}] = [b^\dagger_{q,\eta}, F_{\eta'}] = 0. \tag{1.43}$$

To rectify this Haldane suggested additional terms in the Klein factors, which then correctly produces the relations given by Eqs. (1.43),

$$F_\eta^\dagger \equiv \frac{\sqrt{2\pi\epsilon}}{L}\int_{-L/2}^{L/2} dx\; e^{i\frac{2\pi}{L}\hat{N}_\eta x} e^{-i\phi_\eta(x)}\left[\sum_k e^{-ikx} c_{k,\eta}^\dagger\right], \tag{1.44}$$

where $\phi_\eta(x)$ is defined by Eq. (1.33). This allows us to allow produce the Klein factor commutation relations as follows,

$$\begin{aligned} \{F_\eta^\dagger, F_{\eta'}\} &= 2\delta_{\eta,\eta'}, & \{F_\eta^\dagger, F_{\eta'}^\dagger\} &= \{F_\eta, F_{\eta'}\} = 0, \\ [\hat{N}_\eta, F_{\eta'}^\dagger] &= \delta_{\eta,\eta'} F_\eta^\dagger, & [\hat{N}_\eta, F_{\eta'}] &= -\delta_{\eta,\eta'} F_\eta. \end{aligned} \tag{1.45}$$

The final task to obtain the bosonic representation of the fermionic operator can then be obtained by inverting Eq. (1.44) [23],

$$\psi_\eta(x) = \frac{1}{\sqrt{2\pi\epsilon}} F_\eta\; e^{i2\pi\hat{N}_\eta x/L} e^{-i\phi_\eta(x)}. \tag{1.46}$$

This section has therefore provided us with a complete dictionary of mapping our interacting fermionic Hamiltonian to a free particle bosonic problem. We will make use of this in the later half of Chapter 3 when we consider interactions between 1D chiral modes in graphene. In Chapter 3 we will also consider what happens when we map an interacting electronic Mach-Zehnder model built of these modes in graphene onto bosonic variables. We further include the effect of previously unconsidered cross-channel interactions effects within the MZI model. Before this though we require the necessary background to understand the emergence and subtleties of these chiral modes in graphene. The next chapter therefore gives an overview of graphene and the origins of its 1D modes, as well as detaining the difference between these modes in graphene and those found in conventional semi-conductors.

Chapter 2

Relativistic Quantum Hall in Graphene

Graphene is the first truly 2D material to be observed in nature. Its discovery [60] won Andre Geim and Konstantin Novoselov the 2010 Nobel Prize. The technological implications of graphene are far reaching and have still yet to be fully exploited. It has the highest tensile strength of any material ever tested [61], extremely high electron mobilities [9] and the capacity to be used to construct electronic devices on a much smaller scales than any material prior to its discovery [62]. Our interest in graphene lies within its interesting dispersion relations at low-energies, where the electronic behaviour is analogous to massless relativistic fermions described by a 2D Dirac equation [63, 64]. Of particular interest is the impact of a high magnetic field on this dispersion as we enter the quantum Hall regime in graphene. Landau quantisation in graphene is different to that seen in conventional 2D semi-conductors [65, 66]. These differences, paired with the resemblance of graphene low-energy Hamiltonian to the Dirac equation, means that the discretisation of the energy spectrum in graphene is often referred to as the *relativistic quantum Hall effect*. In this section we explore the differences between the 1D chiral modes seen in the

quantum Hall regime in graphene and that seen in conventional 2D semi-conductors. We will particularly focus on the interesting features of these modes along a PN junction interface in a high magnetic field in graphene. This system has had an array of interesting, and seemingly contradictory, experiments performed on it in the last decade [26, 27, 29, 11]. We will, in this chapter, construct the formalism necessary to understand these experiments. We then proceed, in the chapter following this one, to present the first major piece of original research in this thesis in which we reconcile the apparent differences of these experiments into one model. We will also see that the high mobilities in graphene and additional degeneracies mean that the PN junction lends itself to construction of a *electronic Mach-Zehnder* which is far superior [11] to its analogues in conventional 2D semi-conductors discussed in section 1.2. This will lead us on to the second piece of original research in this thesis, in which we use the bosonisation technique (explained in section 1.3.1) to describe the additional interactions such a system brings in as compared to in conventional electronic MZI. We then utilise the resulting model to calculate current measurement with these previously unconsidered effects included. In this chapter, we begin with a lattice model of electrons in graphene and then proceed to develop a continuum description of their low energy properties. We then add a strong magnetic field, and finally, electrostatic potentials which will be used to describe both a PN junction and the edge of a sheet of graphene.

2.1 Deriving the Dirac Equation

Graphene is formed from carbon atoms which have solidified into a honeycomb structure which can equivalently be thought of as two triangular Bravais lattices occupied by two inequivalent atom sites which we label by A and B sub-lattices [63], cf. Fig.(2.1).

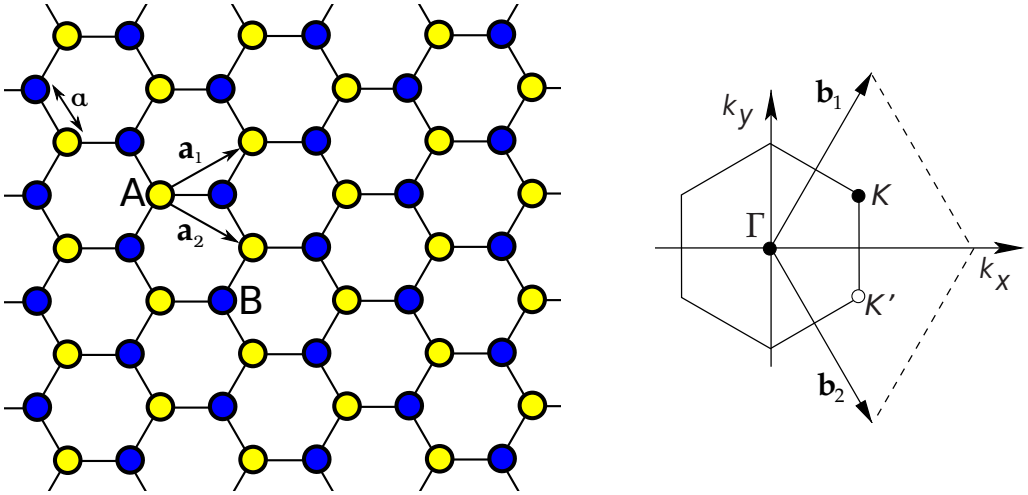

Figure 2.1: The left image gives a sketch of the atomic structure of graphene. Graphene's lattice sites are composed of two inequivalent atoms separated by an atomic distance a, these form two sub-lattices, A and B. The lattice vectors for these sub-lattices are given by $\mathbf{a}_1$ and $\mathbf{a}_2$ which are labelled on the sketch. On the right we have the reciprocal lattice centred on Γ, the two inequivalent corners of the Brillouin zone are labelled K and K'. The reciprocal lattice vectors $\mathbf{b}_1$ and $\mathbf{b}_2$ are also labelled.

A-B atoms sit at a nearest neighbour distance of $a = 0.142$nm from each other [64], we may describe the basis vectors which describe the underlying triangular structure of the lattice as,

$$\mathbf{a}_1 = \frac{a}{2}\big(3, \sqrt{3}\big), \qquad \mathbf{a}_2 = \frac{a}{2}\big(3, -\sqrt{3}\big). \tag{2.1}$$

The reciprocal-lattice vectors can then be calculated as,

$$\mathbf{b}_1 = \frac{2\pi}{3a}\big(1, \sqrt{3}\big), \qquad \mathbf{b}_2 = \frac{2\pi}{3a}\big(1, -\sqrt{3}\big). \tag{2.2}$$

Of particular interest will then be the points which describe the corners of the Brilluoin zone. These are two inequivalent points which we call K and K', their

respective positions in momentum space are given as

$$\mathbf{K} = \left(\frac{2\pi}{3a}, \frac{2\pi}{3\sqrt{3}a}\right), \qquad \mathbf{K}' = \left(\frac{2\pi}{3a}, -\frac{2\pi}{3\sqrt{3}a}\right). \tag{2.3}$$

With the basics of graphene structure determined, we can think about its dispersion relation. We consider the tight-binding model which describes an electron able to hop only from A atoms to B atoms and vice versa,

$$H = -t \sum_{\langle i,j\rangle,\sigma} \left(a^{\dagger}_{\sigma,i} b_{\sigma,j} + \text{H.c}\right) \tag{2.4}$$

where $a^{\dagger}_{\sigma,i}$ ($a_{\sigma,i}$) creates (annihilates) an electron with spin σ at site $\mathbf{R}_i$ on sub-lattice A ($b_{\sigma,i}$ operators describe the equivalent on sub-lattice B). Switching to the Fourier space representation of the electronic operators, the Hamiltonian may be written as,

$$H = \sum_{\mathbf{q},\sigma} \begin{pmatrix} a^{\dagger}_{q,\sigma} & b^{\dagger}_{q,\sigma} \end{pmatrix} \begin{pmatrix} 0 & -tf(\mathbf{q}) \\ -tf^{*}(\mathbf{q}) & 0 \end{pmatrix} \begin{pmatrix} a_{q,\sigma} \\ b_{q,\sigma} \end{pmatrix} \tag{2.5}$$

with $f(\mathbf{q}) = e^{-iq_x a} + 2e^{iq_x a/2}\cos\left(\sqrt{3}q_y a/2\right)$. Diagonalising this Hamiltonian produces the dispersion relation [67],

$$\epsilon_{\mathbf{k}} = \pm t|f(\mathbf{q})| \tag{2.6}$$

This dispersion is plotted in fig. (2.1). The negative and positive parts of the spectrum touch at 6 points in the figure though only two are inequivalent (the others are all accessible through an integer number of reciprocal lattice vectors from these two), these lie at the K and K' points given by Eq. (2.3).

The low energy physics is therefore governed by the states close to these points: this

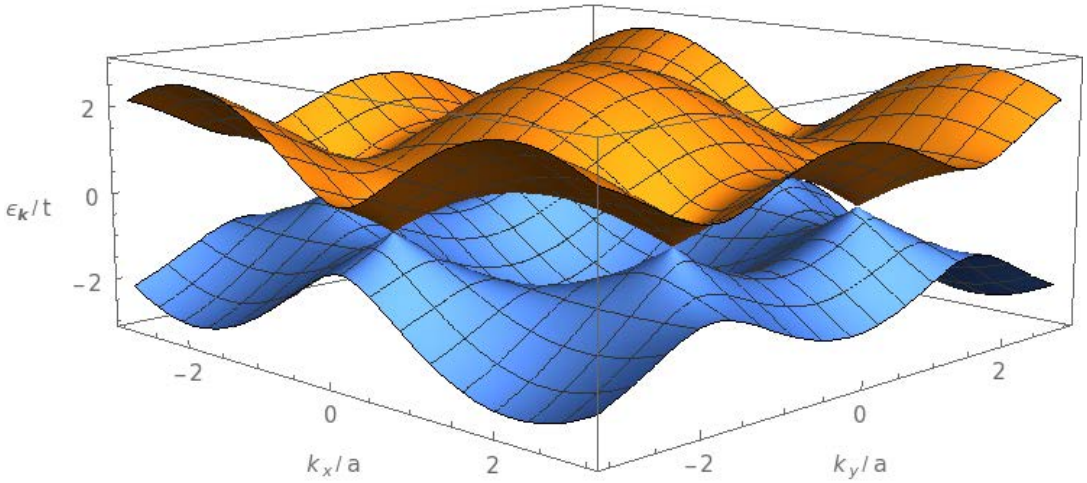

Figure 2.2: Dispersion spectrum of graphene, given by Eq. (2.6).

is the physics we are most interested in. We therefore break up our Fourier series into only the excitations close to these points [63],

$$a_n = \frac{1}{\sqrt{L}} \sum_{\mathbf{q}} e^{-i\mathbf{q}\cdot\mathbf{R}_n} a(\mathbf{q}), \tag{2.7}$$

$$\approx \frac{1}{\sqrt{L}} e^{-i\mathbf{K}\cdot\mathbf{R}_n} \sum_{\mathbf{k}} e^{-i\mathbf{k}\cdot\mathbf{R}_n} a(\mathbf{K}+\mathbf{k}) + \frac{1}{\sqrt{L}} e^{-i\mathbf{K}'\cdot\mathbf{R}_n} \sum_{\mathbf{k}} e^{-i\mathbf{k}\cdot\mathbf{R}_n} a(\mathbf{K}'+\mathbf{k}), \tag{2.8}$$

$$\approx a_{1,n} e^{-i\mathbf{K}\cdot\mathbf{R}_n} + a_{2,n} e^{-i\mathbf{K}'\cdot\mathbf{R}_n}. \tag{2.9}$$

By assuming there are restrictions on $\mathbf{k}$ so that $|\mathbf{k}| \ll |\mathbf{K} - \mathbf{K}'|$ (equivalent to assuming only low energy states are accessible), we see that $a_{1,n}$ and $a_{2,n}$ describe excitations close to K and K' respectively, where $\mathbf{k}$ just describe small variations in momentum about these points. We construct a representation for b_n (operators on the B sites) similarly. When we include the restriction that $\mathbf{k}$ is small, the

Hamiltonian reduces to the following,

$$H = \hbar v_F \sum_{\mathbf{k}} \begin{pmatrix} a_{K+k} \\ b_{K+k} \\ a_{K'+k} \\ b_{K'+k} \end{pmatrix}^{\mathbf{T}} \begin{pmatrix} 0 & k_x - ik_y & 0 & 0 \\ k_x + ik_y & 0 & 0 & 0 \\ 0 & 0 & 0 & k_x - ik_y \\ 0 & 0 & k_x + ik_y & 0 \end{pmatrix} \begin{pmatrix} a_{K+k} \\ b_{K+k} \\ a_{K'+k} \\ b_{K'+k} \end{pmatrix},$$

with $v_F = -3ta/2\hbar$ ($\approx 10^6 ms^{-1}$). The block matrix structure shown above tells us that eigenstates for excitations associated with different valley indices (K/K') are orthogonal. This leads us to draw parallel to that of spin indices and we will sometimes refer to excitations close to different Dirac points as having different *pseudo-spin*. Fourier transforming the Hamiltonian back to real space and taking the continuum limit,

$$H = \int d\mathbf{r} \big(\psi_K^\dagger(\mathbf{r})\ \psi_{K'}^\dagger(\mathbf{r})\big) \begin{pmatrix} H_K & 0 \\ 0 & H_{K'} \end{pmatrix} \begin{pmatrix} \psi_K(\mathbf{r}) \\ \psi_{K'}(\mathbf{r}) \end{pmatrix}, \tag{2.10}$$

$H_K = \mathbf{p} \cdot \boldsymbol{\sigma}, H_{K'} = \mathbf{p} \cdot \boldsymbol{\sigma}^*$ where $\mathbf{p}$ is the a 2D momentum operator $\mathbf{p} = (p_x, p_y)$ and $\boldsymbol{\sigma} = (\sigma_x, \sigma_y)$ are the standard Pauli matrices. ψ_K and $\psi_{K'}$ are 2 component spinors, whose elements represent the A and B sub-lattice. The full wave function is given by,

$$\Psi(\mathbf{r}) = \psi_K(\mathbf{r}) e^{-i\mathbf{K}\cdot\mathbf{r}} + \psi_{K'}(\mathbf{r}) e^{-i\mathbf{K}'\cdot\mathbf{r}}. \tag{2.11}$$

We will *only* consider the low energy properties of the electrons in graphene and therefore we assume that the Dirac equation-like Hamiltonian given by Eq. (2.10) contains all the physics that is relevant for us. In the next section we will see what happens when we add a strong magnetic field to our graphene sheet.

2.1.1 Graphene in a Strong Magnetic Field

As in Section 1.1 we can again include a magnetic field via minimal substitution $\mathbf{p} \to \mathbf{p} + e\mathbf{A}$ [68]. The geometry we consider is an infinite graphene sheet in the xy-plane with a magnetic field pointing out of the plane (z-direction). We use the Landau gauge for the choice of vector potential, $\mathbf{A} = -By\hat{\mathbf{x}}$, which generates the desired magnetic field. This choice also ensures the Hamiltonian remains translationally invariant in the x-direction so the form of the solution in this direction is (similarly to Section 1.1) given by the plane wave $\psi_K(\mathbf{r}) = e^{ikx}\Phi(y)$.

$$\begin{aligned} E^K\psi_K(\mathbf{r}) &= v_F[(\mathbf{p} + e\mathbf{A}) \cdot \boldsymbol{\sigma}]\psi_K(\mathbf{r}), \\ E^K\Phi(y) &= \frac{\hbar v_F}{l_B} \begin{pmatrix} 0 & l_B\partial_y + y/l_B - l_B k \\ -l_B\partial_y + y/l_B - l_B k & 0 \end{pmatrix} \Phi(y), \end{aligned} \tag{2.12}$$

where the magnetic length, $l_B = \sqrt{\hbar/eB}$. The eigenvectors and eigenvalues can then be found as [63],

$$\begin{aligned} E^K_{\pm,n} = \pm\hbar\omega\sqrt{n}, \qquad \Phi_{\pm,n} &= \begin{pmatrix} \phi_{n-1}(y - y_0) \\ \pm\phi_n(y - y_0) \end{pmatrix}, \qquad \text{for } n > 0, \\ E^K_0 = 0, \qquad \Phi_0 &= \begin{pmatrix} 0 \\ \phi_n(y - y_0) \end{pmatrix}, \qquad \text{for } n = 0, \end{aligned} \tag{2.13}$$

where $\phi_n(y - y_0)$ are the solutions of the 1D harmonic-oscillator centred on $y_0 = l_B^2 k$, see Eq. (1.4) and $\omega = \sqrt{2}v_F/l_B$. The energy spectrum near $\mathbf{K}'$ can be written in the same way, the wave function on K' are also similar with the only exception being that the components of the spinor in Φ' are reversed compared to Φ (where $\psi_{K'}(\mathbf{r}) = e^{ikx}\Phi'(y)$).

We see several immediate differences from the standard quantum Hall effect. Firstly graphene Hall spectrum is proportional to the square root of the magnetic field as opposed to linear in it as in the semi-conductor case. This leads to a vastly different intrinsic energy scale to the problem, in a semiconductor at a magnetic field of 10T the gap between different Landau levels is of the order of 10K, with the same field in graphene this leads to a gap of the 1000 K [63]. With such a large gap one can see the distinctive conductance curves characteristic of quantum Hall even at room temperatures [69]. A further difference between the 'relativistic' (so termed because of the similarity between graphene low energy Hamiltonian and that of that Dirac equation) quantum Hall effect and the standard one is the appearance of negative energy Landau levels which one can continuously dope the Fermi energy into from the positive levels. Landau levels effectively split the energy spectrum into discrete sections, these negative energy levels come from the part of the cone-like energy spectrum below the Dirac point being discretised. It is these negative levels that make the quantum Hall effect in graphene so interesting. We next consider the effect of putting a potential difference across a sheet of graphene in a high magnetic field and see that it leads to gapless energy bands much like the bands of the standard edge states seen in Section 1.1. What is particularly interesting in this case is when we put the potential on one side of the sheet above the Dirac point and the other side below, producing a PN junction. We will see that negative energy and positive energy edge modes which travel in opposite directions at the edge of the graphene sheet will copropagate along the PN junction, supplying the junction with excitations from different sources. This system is of interest to us as it is the basis of several very interesting experiments over the past decade. We describe these in depth in Chapter 3, but first we shall introduce the high magnetic field PN junction in graphene properly in the next several sections.

2.1.2 Addition of a spatially varying potential

We limit our potential so that it only varies in the y-direction, i.e $V(y)\mathbb{1}$. This choice allows us to continue to use a Bloch wave as the x-dependent part of the solution to the Hamiltonian. Here the $\mathbb{1}$ is the identity matrix in lattice space and valley space, and is simply a statement that we have taken the potential to act indiscriminately on A and B sub-lattices as well as the different valleys, as is expected for a spatially varying potential. Combining this with Eq. (2.12) we obtain the energy equation given by

$$E^K\Phi(y) = \frac{\hbar v}{l_B}\begin{pmatrix} \frac{l_B}{\hbar v}V(y) & l_B\partial_y + y/l_B - l_Bk \\ -l_B\partial_y + y/l_B - l_Bk & \frac{l_B}{\hbar v}V(y) \end{pmatrix}\Phi(y). \tag{2.14}$$

We can make a further simplification providing that the length scale over which the potential varies is much larger than the magnetic length ($\partial_y V(y) \ll \hbar\omega/l_B$). In which case we may try to approximate the potential its value at the center of harmonic oscillator states, $V(y_0)$. The energy spectrum can then be extracted as,

$$E^K_{\pm,n,k} = \pm\hbar\omega\sqrt{n} + V(y_0) \quad \text{for } n > 0, \qquad E^K_0 = V(y_0). \tag{2.15}$$

The eigenvectors of Eq. (2.14) are identical to those described by Eq. (2.13). If we pick a $V(y)$ as an experimentally [70] relevant function, we obtain an energy spectrum as shown in Fig. (2.3).

In the example shown in Fig. (2.3) we've chosen $V(y)$ as a hyperbolic tangent function. We see that the material remains an insulator at both $y \to \infty$ and $y \to -\infty$ due to the Fermi level lying between Landau levels ($E_F = 0$). It does however have conducting bands near $y = 0$, here the energy bands are bent upwards and intersect the Fermi energy, at which point gapless energy modes exist and therefore we have

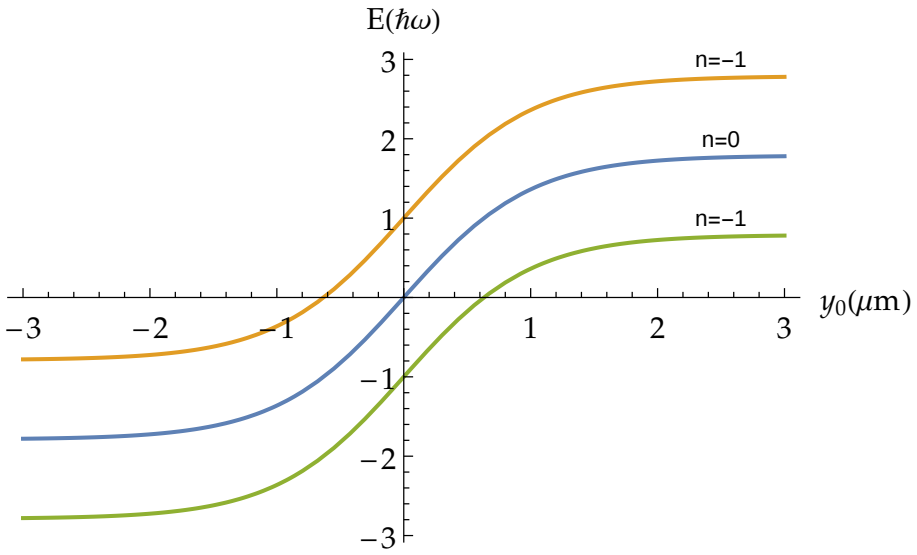

Figure 2.3: Example of the energy bands across $V(y) = eV_0 \tanh\left(\frac{y}{L}\right)$ with $V_0 = 0.2V$, and $L = 1\mu m$ (parameters chosen to be similar in scale to experiments on PN junctions in graphene [70]. Note that the label $n = -1$ is for ease of notation, strictly speaking it refers to $E^K_{-,1,k_x}$ from equation (2.15), i.e it is the negative solution with n=1.

conducting channels which are localised in the y direction but plane waves in x. The width of these states is given by the width of the harmonic oscillator states and proportional to l_B: we may essentially treat these modes as 1D conducting channels (we will prove this in the next section). We see that we can control exactly how many of these modes exist at the interface by altering of V_0. Using the form $V(y) = eV_0 \tanh\left(\frac{y}{L}\right)$ and then choosing $eV_0 = \hbar\omega\sqrt{n}$ will give $2n + 1$ gapless modes at the interface per spin per Dirac point (i.e in total we'd have $4 \times (2n + 1)$ modes if we include all degeneracies).

An interesting feature of a type of potential like $V(y)\mathbb{1}$ is that it utterly fails to confine electrons to low potential regions. No matter how large we make $V(y)$ or what form it takes, there are always Landau levels that can be bent up and cut the Fermi level. This implies that there are always available states, many of which far

from the low potential region, for the electron to tunnel into. Consider the exponentially spatially varying potential shown in Fig. (2.4), since all bands are bent in the same direction one can envision how if we included the $\lambda = -$, $n > 1$ levels we would see bands that are still available at $E = 0$ far into the high potential region. This is a signature of *Klein tunnelling* [71, 72, 73] in a high magnetic field. The type of potential used above which is the same across lattice and valley spaces can therefore not be used to confine an the electron to the graphene sheet and we must consider an alternative description. In the next section we consider such an alternative in order to get a working description of what is happening to the electron at the edge of a sheet of graphene in a high magnetic field.

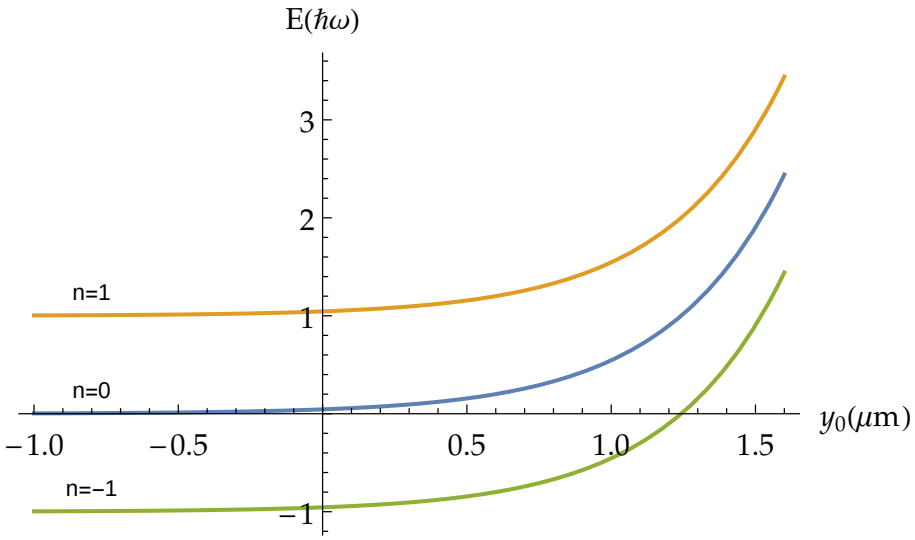

Figure 2.4: Potential of the form $V(y) = eV_0e^{y/L}$, with $V_0 = 0.01V$ and $L = 0.4\mu m$ using a simple spatially varying $V(y)\mathbb{1}$ potential. We see that this potential fails to confine the electron due to the existence of available energy bands no matter how far from the origin we travel. We only show down to $n = -1$ here for clarity, but the effect of all negative Landau levels as we take $n \to -\infty$ means there are infinite bands for the electrons to occupy even in the extremely high potential regions. Once again we are using the notation $n = -1$ to mean $\lambda = -, n = 1$.

2.1.3 Confinement Potential

Instead of the potential previously considered, which acts indiscriminately on all of the vector subspaces of the problem we could generate an effective confinement potential by utilising a potential of the form $V(y)\sigma_z$ [74], where the Pauli matrix is in the A-B space. This potential acts with a different sign on the difference lattice subspaces, this type of confinement is sometimes referred to as *mass confinement*, as it is equivalent to adding a mass term into a relativistic energy spectrum. Under such a potential, and using the the same approximation as in the case of the symmetric potential (i.e, that the potential varies slowly on the scale of the magnetic length, $\partial_y V(y) \ll \hbar\omega/l_B$), one can use similar techniques to in the previous section and the energy levels can be extracted as,

$$E^{K/K'}_{\pm,n,k} = \pm\hbar\omega\sqrt{n + \big(\frac{V(y_0)}{\hbar\omega}\big)^2}, \qquad n > 0, \tag{2.16}$$

$$E^{K}_{0,k} = -V(y_0) \qquad E^{K'}_{0,k} = V(y_0). \tag{2.17}$$

Again with the exact same eigenvectors as in the previous two sections, Eq. (2.13). This generates qualitatively the same spectrum produced by numerical calculations directly using the tight binding model with a finite lattice (see [63, 75]), although the numerical calculations show that the specifics of the dispersion depend on the edge geometry. Since the potential generates the correct dispersion relation we assume that it includes the correct physics, although all we really need is that it provides the correct number of energy bands crossing the Fermi energy (which it does). We therefore see that this peculiar splitting leads to a number of edge modes given by,

$$\nu = \pm 2(2n + 1), \tag{2.18}$$

where the $2n$ comes from the valley degeneracy of each level. This symmetry is

broken at $n = 0$ where one energy band is bent upwards and one downwards. This is the origin of the $+1$ in ν. The extra factor of 2 is a result of spin degeneracy.

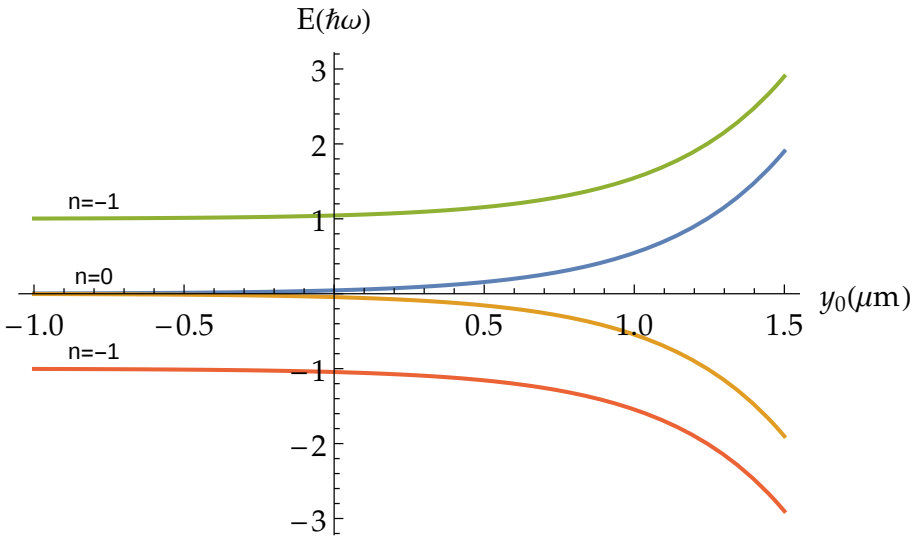

Figure 2.5: Potential of the form $V(y) = eV_0e^{y/L}$, with $V_0 = 0.01V$ and $L = 0.4\mu m$, identical to that shown in Fig. (2.4) but this time using mass confinement potential, $V(y)\sigma_z$. This potential (in contrast to Fig. 2.4)) bends negative energy Landau levels down and positive energy Landau levels up. This means that, for any finite chemical potential, states only exist where the centre of the cyclotron motion y_0 is close to the origin.

A particularly interesting feature of the E_0 energy levels is that the Landau levels corresponding to one of Dirac points bend upwards ($\partial E/\partial k > 0$) in the presence of the confinement potential, whilst near the other Dirac point they bend downwards ($\partial E/\partial k < 0$) (again this is confirmed by numerical solutions [63, 75]). This results in excitations with opposite velocities. If we once again envision ourselves to be in the situation described at the end of the previous section where the sheet of graphene is doped so that on one side $\nu > 0$ and on the other $\nu < 0$ (i.e a PN junction) then the excitations at the edge of the graphene sheet on opposite sides of the junction travel in the opposite direction to each other. We may, therefore, set this up so the excitations on either side of the junction travel towards each

other, cf. Fig.(2.6). At the interface, the two channels meet and are directed into the artificial edge states created by the PN potential. The two channels then co-propagate according to Equation (2.29). We assume this process to be an adiabatic one, and so K-excitations are directed into the states with momenta close to K of the junction, and similarly for K'. We can therefore utilise the different origins of these two excitations to supply them from different reservoirs (labelled as $S1$ and $S2$ in the Figure (2.6)). At the other edge of the sheet the excitations again split up and now propagate away from each other towards the drains $D1$ and $D2$.

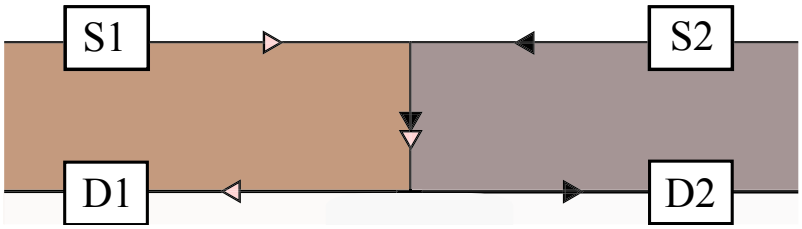

Figure 2.6: Figure showing a sheet of graphene with a potential creating a PN junction across it, the red side has a negative top gate potential acting on it whilst the grey has a positive one, this results in excitations from $S1$ and $S2$ having opposite velocity at the true edge (bordering the white), these excitations then co-propagate along the junction interface, which then separate again when they hit the other edge and head towards the drains $D1$ and $D2$.

The main take away point from the above section is that if we apply a spatially varying potential along a sheet of graphene in a strong magnetic field we obtain 1D chiral modes which can then be supplied from the 1D modes from the physical edge. The argument for the fact they are 1D is relatively clear: the states are localised in one direction and plane waves in the other, implying 1D nature. In the next section we treat these excitations more carefully in order to generate a Hamiltonian describing the excitations which form the chiral currents along the edge and junction interface. We then use ideas similar to in Chapter 1 to see that a linearised version of 1D excitation spectrum of these excitations is a valid description in the low energy

limit.

2.2 1D modes along the PN interface

The goal of this section is to use the previously extracted wave functions which describe excitations of graphene under a slowly varying potential to obtain the Hamiltonian which describes the emergent 1D physics at the edge of the graphene sheet and along the PN junction interface.

We start by explicitly noting the eigenvectors of the Dirac Hamiltonians with the addition of slowly varying potentials $V(y)\mathbb{1}$ and $V(y)\sigma_z$ which correspond to the energy eigenvalues Eq. (2.17, 2.15) respectively.

$$\psi_{\pm,n,k}(x,y) = e^{ikx}\Phi_{\pm,n}(y-y_0), \qquad \psi'_{\pm,n,k}(x,y) = e^{ikx}\Phi'_{\pm,n}(y-y_0), \quad (2.19)$$

$$\Phi_0(\xi) = \begin{pmatrix} 0 \\ \phi_0(\xi) \end{pmatrix}, \qquad \Phi_{n,\pm}(\xi) = \frac{1}{\sqrt{2}}\begin{pmatrix} \phi_{n-1}(\xi) \\ \pm\phi_n(\xi) \end{pmatrix}, \quad (2.20)$$

$$\Phi'_0(\xi) = \begin{pmatrix} \phi_0(\xi) \\ 0 \end{pmatrix}, \qquad \Phi'_{n,\pm}(\xi) = \frac{1}{\sqrt{2}}\begin{pmatrix} \pm\phi_n(\xi) \\ \phi_{n-1}(\xi) \end{pmatrix}. \quad (2.21)$$

$\phi_n(\xi)$ describe the usual 1D harmonic oscillator solutions given by Eq. (1.4), and upper and lower elements of Φ refer to AB sub-lattices respectively and it important to remember that K and K' wave function refer to different vector spaces. The full solution close to a particular Dirac point is then given as,

$$\psi_{K^{(\prime)}}(\mathbf{r}) = \frac{1}{\sqrt{L}}\left[\sum_k e^{ikx}\Phi_0^{(\prime)}(y-l_B^2k)c_{K_x^{(\prime)}+k} + \sum_{\substack{\lambda=\pm,\\ n,k}} e^{ikx}\Phi_{n,\lambda}^{(\prime)}(y-l_B^2k)c_{K_x^{(\prime)}+k,n,\lambda}\right], \quad (2.22)$$

where L is the length of the junction interface. $c_{K_x^{(\prime)}+k,n,\lambda}$ operators describe the annihilation of an excitation with momenta k near the $K^{(\prime)}$ Dirac point in the nth Landau level (with $n > 0$). The λ index tells us if we are above ($\lambda = +$) or below ($\lambda = -$) the Dirac point. For the $n = 0$ Landau level we have dropped both the n and λ indices as there is only one level in this case. These operators also ensure the field operator obey fermionic exchange statistics:

$$\{c_i, c_j^\dagger\} = \delta_{i,j}, \qquad \{c_i, c_j\} = \{c_i^\dagger, c_j^\dagger\} = 0. \tag{2.23}$$

The full low energy wave function can then be obtained by putting these back into Eq. (2.11), so that

$$\Psi(\mathbf{r}) = \psi_K(\mathbf{r})e^{-i\mathbf{K}\cdot\mathbf{r}} + \psi_{K'}(\mathbf{r})e^{-i\mathbf{K}'\cdot\mathbf{r}}. \tag{2.24}$$

From which we may construct the Hamiltonian which described our low energy excitations,

$$\begin{aligned} H &= \int dxdy\ \Psi^\dagger(\mathbf{r})\hat{H}\Psi(\mathbf{r}), \\ &= H_K + H_{K'} \end{aligned} \tag{2.25}$$

Orthogonality between the different valleys spaces kills any matrix elements between excitations close to different Dirac points, integration over x is trivial to perform and then integration over y can be done by utilising the orthogonality of Hermite polynomials, $\int dy\ \phi_n(y - y_0)\phi_m(y - y_0) = \delta_{n,m}$. This leaves us with two separate Hamiltonians describing excitations with momentum close to the K and K' points.

For K excitations this is given by

$$H_K \equiv \sum_k E^K_{0,k} c^\dagger_{K_x+k} c_{K_x+k} + \sum_{\lambda=\pm} \sum_{k,n} E^K_{k,n,\lambda} c^\dagger_{K_x+k,n,\lambda} c_{K_x+k,n,\lambda}, \tag{2.26}$$

and similarly for $H_{K'}$ with $K \to K'$ in Eq. (2.26).

Eq. (2.25) and (2.26) therefore describe the fermionic excitations in graphene in a high magnetic field coupled with any slowly varying potential (including a mass confinement style potential), where the specifics of the potential are built into the dispersion spectrum $E_{k,n,\lambda}$. We are most interested in the one dimensional physics close to the the real edge of graphene and along the PN interface. We anticipate finding chiral 1D modes at these points. When the Fermi energy is doped so that it bisects the energy bands which describe electron in these modes, we expect these modes to be the only position at which excitations can exist at low temperatures. We zoom in on the dynamics in this region by expanding the energy spectrum close to the Fermi level. Considering the PN potential, we first imagine the simplest situation, where the potential is chosen such that it pushes the $n = 1, \lambda = -$ Landau level below the Fermi energy for any y and below the equivalent positive energy state $n = 1, \lambda = +$, i.e $E_{-,1,k} < \epsilon_F < E_{+,1,k}$. Finally we choose $V(y)$ so that one side of the junction E_k is below the Fermi level, but on the other it is above, this situation is shown in Fig. (2.7).

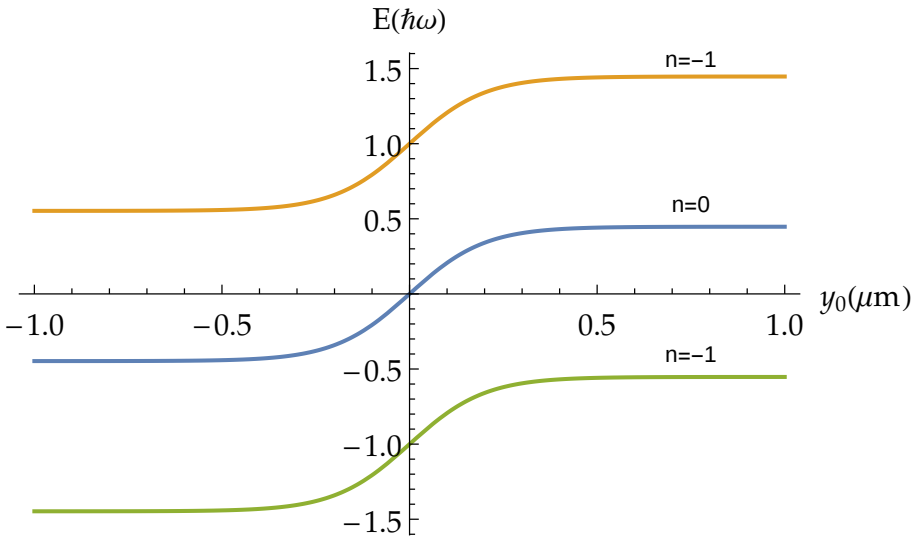

Figure 2.7: Example of the energy bands of electron in a high magnetic field in graphene under a potential $V(y)\mathbb{1}$ with $V(y) = eV_0 \tanh\left(\frac{y}{L_V}\right)$ with $V_0 = 0.05V$, and $L_V = 0.2\mu m$. The Fermi level sits at $E = 0$ therefore only the $n = 0$ Landau level is bisected and this gives rise 1 chiral modes per Dirac point and spin travelling in the same direction along the junction. We may linearise the spectrum about this point for small temperatures, to obtain Eq. 2.29. Note the difference between this dispersion relation and the one found in Fig. (2.3); in that figure, had the Fermi level again been at $E = 0$, we would see 3 chiral modes (per Dirac point and spin) travelling along the junction interface.

These conditions mean that the only excitations which can exist close to the Fermi energy come from the E_0 energy band, of which there is one per Dirac point (two if we include spin). The E_0 band corresponds to to the lowest (non-negative) Landau level, $E_{0,k}^{K/K'} = V(l_B^2 k)$. Assuming temperature to be low we may then expand this close to $\epsilon_F = V(l_B^2 k_F)$,

$$E_{0,k} = V(l_B^2 k_F) + \left.\frac{\partial V(l_B^2 k)}{\partial k}\right|_{k=k_F} (k - k_F) + \mathcal{O}\big((k - k_F)^2\big) + \ldots \quad (2.27)$$

$$\approx \epsilon_F + \hbar v_F (k - k_F). \quad (2.28)$$

Writing the velocity as $v_F = \frac{1}{\hbar}\left.\frac{\partial V}{\partial k}\right|_{k=k_F}$, which, since V monotonically increases with k is always either positive or zero (positive along the interface, zero deep in the

bulk). The Hamiltonian which describes the low lying excitations in the system we have presented is (with ground state energy (ϵ_F) subtracted off),

$$H_0 = \sum_k \hbar v_F (k - k_F) \big[: c^\dagger_{K_x+k} c_{K_x+k} : + : c^\dagger_{K'_x+k} c_{K'_x+k} : \big] \tag{2.29}$$
$$= -i\hbar v_F \sum_{m=1,2} \int dx \ : \psi^\dagger_m(x) \partial_x \psi_m(x) :, \qquad \psi_{1(2)}(x) = \frac{1}{\sqrt{L}} \sum_{k \sim K_x^{(\prime)}} e^{ikx} c_k,$$

where we have been careful to normally order to take care of the infinities introduced upon linearisation. The above is very similar to the Hamiltonian Eq. (1.9) describing the emergent 1D behaviour in semi-conductors, but here we see that two states are available at the Fermi level, one for each Dirac point, separated by a distance $K_x - K'_x$ in momentum space. This difference in one component of the position of Dirac points can be taken to zero by choosing certain orientations of the sheet of graphene (see next section). This might lead one to the surprising conclusion that it is easier to mediate tunnelling between the two states along the junction if such an orientation is chosen for the PN junction. We will show this is not the case in the next section. We can perform this procedure of linearisation on the other Landau bands about their respective Fermi momentum, these values may be determined from $\epsilon_F = \pm\hbar\omega\sqrt{n} + V(l_B^2 k_{F_{n,\pm}})$. Linearising about $k_{F_{n,\lambda}}$ and carefully resetting the zero of each band ($E_{k,n,\pm} \to E_{k,n,\pm} - \epsilon_F$), we obtain the full linearised Hamiltonian describing the chiral modes which propagate along the PN junction as,

$$H_{PN} = \sum_k \hbar v_F (k - k_F) \big[c^\dagger_{K_x+k} c_{K_x+k} + c^\dagger_{K'_x+k} c_{K'_x+k} \big]$$
$$+ \sum_{k,n,\lambda} \hbar v_{F_{n,\lambda}} (k - k_{F_{n,\lambda}}) \big[c^\dagger_{K_x+k,n,\lambda} c_{K_x+k,n,\lambda} + c^\dagger_{K'_x+k,n,\lambda} c_{K'_x+k,n,\lambda} \big], \tag{2.30}$$

where, in order to use this Hamiltonian we make sure to keep only the bands where the Fermi level bisects the bands i.e when $\epsilon_F = \pm\hbar\omega\sqrt{n} + V(l_B^2 k_{F_{n,\pm}})$ can be sat-

isfied. We stress once more here that our sum over k is only for small momentum, $|k|, |k_F| \ll |K_x - K'_x|$.

Similarly, we can utilise a virtually identical procedure with a confinement potential of the form described in Section 2.1.3. In which case the predominant difference between the two types of potential is seen in the velocity, in the confinement case the $n = 0$ Landau levels acquires opposite velocities and, for all other levels, a factor of $\lambda = \pm$ is added, the velocity (being determined by the form of the potential) is of course different at the edge than along the interface so we label the velocity as u_F in this case.

$$H_E = \sum_k \hbar u_F (k - k_F) \left[c^\dagger_{K_x+k} c_{K_x+k} - c^\dagger_{K'_x+k} c_{K'_x+k} \right] \tag{2.31}$$

$$+ \sum_{k,n,\lambda} \lambda \hbar u_{F_{n,\lambda}} (k - k_{F_{n,\lambda}}) \left[c^\dagger_{K_x+k,n,\lambda} c_{K_x+k,n,\lambda} + c^\dagger_{K'_x+k,n,\lambda} c_{K'_x+k,n,\lambda} \right], \tag{2.32}$$

Since our description is as an approximate one and we will not usually be able to determine the velocity in either case we will usually assume that $u_F = v_F$ when an excitation travels from the edge to the PN junction interface.

In the next section we consider rotating our sample so that the x-axis always travels along the junction interface or sample edge. We see that this rotation has an impact on the distance $|K_x - K'_x|$, since this describes the proximity of the different excitations described by Equations (2.29) and (2.32). We consider whether it can also control the degree to which the modes hybridise.

2.3 PN Junction at any Orientation.

We can change our description of the PN-potential and confinement potential to fit any orientation by simply resetting our x-axis to run parallel to the junction interface or edge respectively. Doing so rotates the orientation of our Brillouin zone and therefore the location of K and K' as follows. We rotate our real space variables

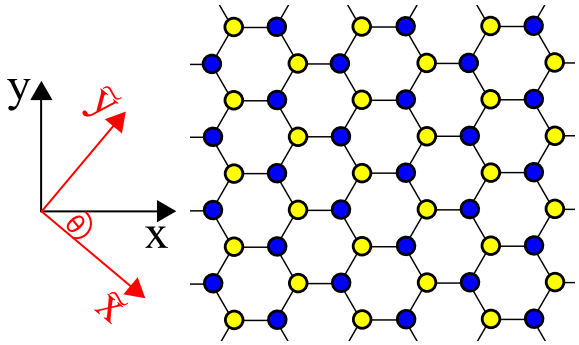

Figure 2.8: A sketch of a sheet of graphene. We rotate the sheet to position the PN junction's interface parallel to the x-axis. The rotated frame is then at an angle θ to how we originally defined it.

so that,

$$\tilde{x} \equiv x\cos\theta - y\sin\theta, \tag{2.33}$$

$$\tilde{y} \equiv x\sin\theta + y\cos\theta. \tag{2.34}$$

We can then apply the same rotation to our reciprocal space,

$$\begin{aligned}
\tilde{\mathbf{K}} &= \big(K_x\cos\theta - K_y\sin\theta, K_x\sin\theta + K_y\cos\theta\big), && (2.35)\\
&= \big(\frac{2\pi}{3a}(\cos\theta - \frac{\sqrt{3}}{3}\sin\theta), \frac{2\pi}{3a}(\sin\theta + \frac{\sqrt{3}}{3}\cos\theta)\big), && (2.36)\\
\tilde{\mathbf{K}}' &= \big(K'_x\cos\theta - K'_y\sin\theta, K_x\sin\theta + K_y\cos\theta\big), && (2.37)\\
&= \big(\frac{2\pi}{3a}(\cos\theta + \frac{\sqrt{3}}{3}\sin\theta), \frac{2\pi}{3a}(\sin\theta - \frac{\sqrt{3}}{3}\cos\theta)\big), && (2.38)\\
\tilde{\mathbf{K}} - \tilde{\mathbf{K}}' &= \big(-\frac{4\pi}{3\sqrt{3}a}\sin\theta, \frac{4\pi}{3\sqrt{3}a}\cos\theta\big), && (2.39)
\end{aligned}$$

where the components $\mathbf{K}^{(\prime)}$ are defined by Eq. (2.3). We can now follow through the same procedures detailed in Sections 2.1.2 and 2.1.3 in our rotated variables to find the solution for the edges/PN-junction at any orientation. Therefore substituting the x-components of these tilded variables (2.39) in for the non-tilde ones in Equations (2.29) and (2.32) provides us with the linearised Hamiltonian describing junctions and edges in any direction. Furthermore we may also assume it provides a reasonable description for a non-straight junction/edge providing the orientation is changed adiabatically.

We then see that the dispersion spectrum for the two types of excitations, K and K' are identical providing $\theta = 0$, and separated by a very large ($\sim 1/a$) distance in momentum space in the situation where the junction is such that $\theta = \pi/2$. The reason for this apparent difference is that momentum in the x-direction (parallel to the junction/edge) is a conserved quantity while in perpendicular (y) direction, it is not.

$$[p_x, H^{K/K'} + \hat{V}(y)] = 0, \qquad [p_y, H^{K/K'} + \hat{V}(y)] \neq 0, \tag{2.40}$$

where $\hat{V}(y) = V(y)\mathbb{1}$ for the junction potential and $\hat{V}(y) = V(y)\sigma_z$.

So, having shown that we can change the distance in momentum space the excitations described by Eq. (2.29) and (2.32) are from each other, we return to the question posed at the start of this section: can the orientation of the the PN junction make a difference to how the excitations hybridise? The answer is 'probably not', while when we integrate out the y-components all dependence on the y-momentum seems to disappear (eventually leaving us with Equations (2.29) and (2.32)). We must consider any matrix elements which determine the hybridisation *before* this

point. Any term of this form is weighted by a extremely fast oscillating $e^{i(\mathbf{K}-\mathbf{K}')\cdot\mathbf{r}}$ term which quickly drops to zero when integrated, *unless* the matrix element is also paired with an additional external potential which varies on the scale of lattice length. We investigate this further in the next chapter. The reason we do not answer the above question definitively is that the orientation does tell us which direction we require this external potential to be compact within in order to accommodate tunnelling. In the absence of any such potential, the two excitations corresponding to K and K' in Eq. (2.29,2.32) are therefore still distinct even when it is the case that $\tilde{K}_x = \tilde{K}'_x$.

2.4 Broken Symmetries

In all previous discussion we have neglected symmetry breaking terms within our description meaning the degeneracy of the Landau levels is such that the number of edge states jumps by 4 (corresponding to a two fold degeneracy for both spin and valley indices) every time our Fermi energy crosses a Landau level. For low magnetic fields this appears to be a reasonable description, however for higher magnetic fields experiments [10, 76] show Hall plateaus which corresponds to observing an increase by 1 edge state as the Fermi-energy is moved through the dispersion spectrum. This is attributed to a full breaking of the four-fold spin-valley symmetry. Breaking of the spin degree of degeneracy is a result of a well known Zeeman effect, where the magnetic moments of the electrons couple to the field, giving an energy bonus to those electrons whose spin align with the field. Such an effect is easy to put into the framework we have constructed, the Zeeman Hamiltonian is simply given [64] by,

$$H_Z = \Delta_Z\big(\mathbb{1}_{\text{valley}} \otimes \mathbb{1}_{AB} \otimes \sigma^z_{\text{spin}}\big), \tag{2.41}$$

i.e it reverses sign for opposite spins but has no changes on the other vectors spaces (the subscripts *valley* and AB refer to the valley and sub-lattices spaces respectively). It simply leads to an energy spectrum of the form $E^{K/K'}_{k,n,\lambda,\sigma} = E^{K/K'}_{k,n,\lambda} \pm_\sigma \Delta_Z$, where the postive or negative sign is determined by which of $\sigma = \uparrow, \downarrow$ aligns with the field. Similarly, we can envision a "Valley-Zeeman" (VZ) Hamiltonian which breaks the valley symmetry by coupling to only this degree of freedom,

$$H_{VZ} = \Delta_{VZ}\big(\sigma^z_{\text{valley}} \otimes \mathbb{1}_{AB} \otimes \mathbb{1}_{\text{spin}}\big), \tag{2.42}$$

The addition of such a term in the full Hamiltonian results in the desired breaking of the K/K' symmetry, $E^{K/K'}_{k,n,\lambda} \to E^{K/K'}_{k,n,\lambda} +/- \Delta_{VZ}$. The problem with this description is that there is no obvious physical field which couples directly to the pseudo-spin. It has been suggested that such an effect may be achievable using strain-induced fields [77, 78], and we may also induce similar effects in $n = 0$ Landau levels by coupling to the sub-lattice using the mass-confinement style potential discussed earlier ($H_M = V\big(\mathbb{1}_{\text{valley}} \otimes \sigma^z_{AB} \otimes \mathbb{1}_{\text{spin}}\big)$), this is specific to the $n = 0$ Landau level where the K/K' states are restricted to occupy the A/B sub-lattices respectively. However, the symmetry breaking effect with the highest energy scale [64], and therefore most likely origin of that which is experimentally observed, is electron-electron interactions effects. The many-body effects mean that this description is much more involved then our simple, single particle H_{VZ}, this complexicity is mirrored by the number of works written on the area [79, 80, 81, 82, 83, 84, 85, 86, 87, 88]. These investigations are beyond the scope of this thesis and we instead make the assumption that even in the event of valley symmetry breaking our chiral 1D Fermi liquid description, given by Eq. (2.29) and (2.32), is a reasonable one (albeit with a renormalised velocity). The energy difference between the two valleys is taken into account when we linearise the energy spectrum, from this we can determine the effective position in y-space an

electron sitting at the Fermi level is localised about ($y_0 = l_B^2 k_F$). We see that due to the energy difference of the two pseudospins (meaning $k_F^K \neq k_F^{K'}$), an insulating gap emerges between the different chiral modes, just as is the case between edge states corresponding to different Landau levels, cf. Fig. (2.3). The difference in energy of the different valleys is therefore reflected in their positions in real space.

In this chapter we have demonstrated that much like in a standard 2D semi-conductor we see the emergence of Landau levels in graphene in a strong magnetic field. Similarly to semiconductors, at low temperatures and under a slowly varying potential these insulating bands transform into conductive 1D chiral modes. In graphene, these modes do have some interesting distinctions from the standard case, principal to these is the feature that different chiral modes can be made to travel in opposite directions at the same sample edge using a PN junction. At the junction interface the modes co-propagate before being forced to separate again as they collide with the other sample edge. In the next section we describe a series of apparently conflicting experiments within such a system. We find that utilising the descriptions generated in this sections and inputting secondary effects, we can describe all these experiments within one model using only one parameter to describe the differences. This model therefore reconciles the apparent contradictions seen in the experiments. We then go on to catalogue and discuss the effects of interactions between different chiral modes at the PN interface, with a particular focus on these effects within a recent experiment [11] which saw an MZI-type visibility effect within the system under discussion. The nature of the modes along the PN interface naturally leads us to approach a previously unconsidered (to the best of our knowledge) model of an electronic Mach-Zehnder in which interaction also occur between different channels of the interferometer.

Chapter 3

Chiral Modes on a PN Junction

In the previous chapter we demonstrated the interesting excitations that emerge within a graphene PN junctions in the quantum Hall regime. In this chapter we describe the seemingly contradictory experiments that have taken place in these systems and propose a simple model where a variable disorder potential is able to reconcile the apparent experimental differences. We give some discussion about the possible interactions that can exist along the PN interface and consider what differences this could bring into using a PN junction to fabricate a graphene MZI.

3.1 Experiments on Graphene PN Junctions

As previously discussed we can create a PN junction in a high magnetic field as shown in Fig (2.6), red and grey sides are held at different potentials by top gates. In the regime where $\nu_1 < 0$ (refers to left side of Fig. (2.6)) and $\nu_2 > 0$ (right side of Fig. (2.6)) excitations at the real edge travel in opposite direction due to the dispersion spectrum having opposite gradients on either side (see Section 2.1.3). Along the junction interface, the energy spectrum of every Landau level is bent in the same direction (see Section 2.1.2), those excitations that travelled in opposite

directions along the true edge now co-propagate along the interface. As such these PN junctions lend themselves as a nice tool to analyse the edge-like physics which occur in graphene. Initial current experiments [26] in a high magnetic field PN junction in graphene saw that if a bias is put on $S1$ whilst $S2$ is left grounded, the current is split equally across the edge modes at the PN interface. So if, for example, we have one edge mode on either side of the junction the current input at $S1$, e^2V/h (where V is the bias attached to $S1$) is split equally between these modes along the interface. The current detected at $D1$ and $D2$ is equal to half of that input, $e^2V/2h$. This experiment was explained [89] in a frame work which assumes full equilibration of channels travelling parallel to each other along the junction. Defining conductance as g between $S1$ and $D2$. This leads to a quantised value of conductance (in units of e^2/h)) given by:

$$g_{pn} = \frac{|\nu_1||\nu_2|}{|\nu_1| + |\nu_2|} = 1, \frac{3}{2}, 3, \frac{5}{3}, ..., \tag{3.1}$$

$$g_{nn} = g_{pp} = \min(|\nu_1|, |\nu_2|) = 2, 6, 10..., \tag{3.2}$$

where the values of ν increase according to Eq. (2.18), i.e spin and valley symmetry breaking weren't observed in this experiment. g_{pn} is the $S1 \rightarrow D2$ conductivity when the top gate potentials are set so the Fermi energy is above the Dirac point on one side of the junction and below on the other (a PN junction), whereas g_{pp}, g_{nn} describes the situations where the graphene sheet is doped to have a Fermi energy where both sides are above or both sides are below the Dirac point respectively. This description coincides strikingly well with the plateaus for the conductance observed in the first experiment performed in these systems [26]. Whilst this model gives the correct results of this experiment (as well as several subsequent experiments [28, 90, 27]), we find the microscopic details behind the model lacking, what, for example, are the origins of the mode mixing? Some discussion of this is given in

Ref. [89] but not in great depth. Furthermore the model fails to explain more recent experiments [29], where the conductance in the bipolar regime was found to not be quantised, and in fact quickly tends towards zero as the magnetic field is increased. Even more interestingly, experiments performed in 2017 were able to observe an interferometric style current pattern indicating that tunnelling only occurs at two points along the junction [11]. We attempt to give a possible resolution to the apparent differences between these experiments via disorder mediated hybridisation between the modes on different sides of the junction.

3.2 Disorder Mediated Tunnelling

Considering just the case where we have $|\nu_1| = |\nu_2| = 1$ (where $\nu_{1(2)}$ are the number of edge states on the two sides of the PN junction). We model Figure (2.6) as two quantum wires, the Hamiltonian of which is given by Eq. (2.29). An electron near K is not free to hybridise with an excitation on the other side of the boundary due to a large momentum difference ($\sim |\mathbf{K} - \mathbf{K}'|$) leaving the two states on the different side of the interface orthogonal. If we wish to reproduce Eq. (3.1) we must include a mechanism to couple our quantum wires, which will transfer this momentum away from the electron. We consider a disorder potential $\Gamma(\mathbf{r})$ which will play this role. In the following we will see when this disorder is relevant and then consider an approximate model which we can solve to provide current and noise calculations for the system. We find that these calculation, for the most part, reproduce the different experiments, with the variability between them coming from different regimes of $\Gamma(\mathbf{r})$.

3.2.1 Obtaining the Hamiltonian

In order for K/K' modes to couple we consider a disorder potential given by $\Gamma(\mathbf{r})$. If we assume the amplitude of this potential is small on the scale of the Fermi energy, we may include it within our energy considerations in terms of the eigenstates of Eq. (2.24) as a first order correction,

$$H_\Gamma \equiv \int_0^l dx \int dy\, e^{i(\mathbf{K}-\mathbf{K'})\cdot\mathbf{r}} \psi_K^\dagger(\mathbf{r})\Gamma(\mathbf{r})\psi_{K'}(\mathbf{r}) + h.c, \tag{3.3}$$

where l is the length of the PN interface. We see to couple the two Dirac points, $\Gamma(\mathbf{r})$ must have a large enough Fourier component to hop an electron from close to K to close K'. Such disorder needs vary over a length scale similar to that of the lattice parameter, else integration over $\mathbf{r}$ paired with the fast oscillating $e^{i(\mathbf{K}-\mathbf{K})\cdot\mathbf{r}}$ term would leave the term irrelevant. Therefore only disorder effects which are of the form,

$$\Gamma(\mathbf{r}) = \sum_i \Gamma_i^{nn'} \delta(y - y_i)\delta(x - x_i), \tag{3.4}$$

can couple different Landau levels (n, n' refer to nth and n'th Landau levels). The integration over y then simply renormalises the amplitude based on the degree to which the wave functions overlap at y_i, and adds a phase. For disorder which couples the zeroth Landau levels ($\Gamma_i \equiv \Gamma_i^{00}$), the amplitude of disorder is altered as below,

$$\Gamma_i \to \Gamma_i e^{i(K_y - K'_y)y_i} \phi_0^*(y_i - y_0)\phi_0(y_i - y'_0), \tag{3.5}$$

One can see that for the harmonic oscillator states that are separated by many magnetic lengths, $\Gamma_i^{nn'}$ drops to zero very quickly ($\sim e^{-(y_0-y'_0)^2/2l_B^2}$). We therefore require that $y_0 \sim y'_0$ or equivalently $k \sim k'$. In other words, proximity of the states in the y-direction, *enforces* that an electron close to K with momentum $K + k$ can

only tunnel to a state with momenta close to $K' + k$. Under this shift of Γ_i the Hamiltonian (3.3) reduces to,

$$H_\Gamma = \int_0^l dx \sum_{k,q\sim 0} \Gamma(x) e^{i\left(K'_x - K_x + q\right)x} c^\dagger_{1,k-q} c_{2,k} + h.c, \tag{3.6}$$

$$= \sum_{k,q\sim 0} \tilde{\Gamma}_{q+K_x-K'_x}\ c^\dagger_{1,k-q} c_{2,k} + h.c. \tag{3.7}$$

One can then see that the Hamiltonian is equivalent to that of our excitations on the either side of the junction coupled by an x-dependent disorder potential $\Gamma(x) \equiv \sum_{q\sim K_x - K'_x} \tilde{\Gamma}_q\ e^{iqx} = \sum_i \Gamma_i \delta(x - x_i)$.

$$H_\Gamma = \int_0^l dx\ \Gamma(x)\ \psi^\dagger_1(x)\psi_2(x) + h.c \tag{3.8}$$

We can combine this with the Hamiltonian describing excitations along the junction, Eq. (2.29), to obtain a full description of the edge mode excitation combined with the disorder mediated hoping, $H = H_0 + H_\Gamma$. We will, however, solve a simpler problem which assumes the tunnelling is 'spread' equally over the length of the hybridisation region and instead use $\Gamma = \frac{1}{l}\int_0^l dx\ \Gamma(x)$. An illustration of this approximation is given by Fig. (3.1). The Hamiltonian (which corresponds to Eq. (2.29) in real space plus a hybridisation region) of such a configuration is described by Eq. (3.9).

$$H \ = \ -i\hbar v_F \sum_{m=1,2} \int dx\ :\psi_m(x)\partial_x\psi_m(x): + \left[\Gamma \int_0^l dx\ \psi^\dagger_1(x)\psi_2(x) + h.c.\right]. \tag{3.9}$$

Neither the above Hamiltonian nor $H_0 + H_\Gamma$ can lead to any localisation effects. The modes along the junction are chiral and co-propagate, back scattering is therefore forbidden. We anticipate the most important feature of the system to be the number of times the electron tunnels. Since our simplified model is in agreement with the original model on this, we expect that the dynamics to be broadly the

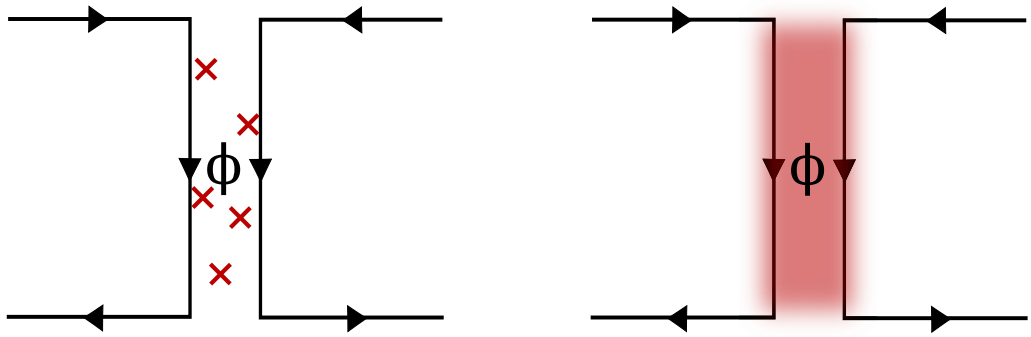

Figure 3.1: A sketch of how we approximate the disorder potential along a PN interface, the black lines represent paths of our chiral modes. The left image shows how we expect the physical PN interface to look, it is described by a disorder potential as in H_Γ, Eq. (3.8). Disorder is given by a series of delta function-like impurities $\Gamma(x) = \sum_i \Gamma_i \delta(x - x_i)$, we represent the impurities as red crosses along the junction interface. An electron from one chiral mode can tunnel into the other at these points. We approximate the problem as in the right image, the tunnelling is taken to be spread over a hybridisation region, as described by Eq. (3.9), we shade the hybridisation region in red. In both cases the gap separating the $\nu = -1$ and $\nu = 1$ modes is threaded by a magnetic flux, ϕ.

same as, some details (such as specifics of interference) may be lost. We therefore anticipate that Eq. (3.9) will describe the situation where coherences become less important, such as when the electron is likely to tunnel many times ($\Gamma/\hbar v_F \gg 1/l$) along the interface of the junction, relatively well. We also note that our simplified model is identical to the original in the limit $\Gamma \to 0$. In the intermediate regime, where the electron tunnels just a handful of times $\Gamma/\hbar v_F \sim 1/l$ we would expect some differences due to the specifics of the interference which are lost in our model. We will see that, in the limit where a tunnelling rate is similar to the length of the junction, we may find a solution to the $H_0 + H_\Gamma$ model in the limit where the impurities are separated by a distance much greater than the Fermi length.

There exists far more rigorous methods of handling the addition of H_Γ which we will briefly touch on now. Typically one could, in a more controlled way than in our description, side step the issue of not knowing the exact form of $\Gamma(x)$ by taking it to

be random and described by some probability distribution which is usually assumed to be Gaussian [91]. In which case we may write the expectation of some operator O averaged over disorder as,

$$\overline{\langle O \rangle} = \frac{\int \mathcal{D}\Gamma e^{-\int dx dx' \, \Gamma(x) D^{-1}(x-x')\Gamma(x)} \langle O \rangle_\Gamma}{\int \mathcal{D}\Gamma e^{-\int dx dx' \, \Gamma(x) D^{-1}(x-x')\Gamma(x)}}, \tag{3.10}$$

where $\langle O \rangle_\Gamma$ describes the expectation of O for some specific realisation of $\Gamma(x)$, and $D(x-x') \equiv \overline{\Gamma(x)\Gamma(x')}$ is the average correlation between the disorder potential at x and x'. In our case we demonstrated that only very compact disorder contributes to the coupling of different chiral modes, which implies $D(x-x') = C\delta(x-x')$ (where C is a constant) is likely a good approximation. We then try to integrate out the $\Gamma(x)$-dependence in the Hamiltonian $H_0 + H_\Gamma$ which determines $\langle O \rangle_\Gamma$ (or usually the corresponding action, as this is easiest done in the path integral formulation). This can be achieved using techniques such as the replica method [91]. Whilst this leaves the remaining Hamiltonian quartic in electronic operators we have eliminated the unknown $\Gamma(x)$-parameters, and we can then approach the problem using techniques from Section 1.3.1. Given more time it would have been interesting to explore this more rigorous description, and this lends itself as a good direction for further work. However, since we anticipate that the most important aspect of the system is that the electron will, on average, tunnel the correct amount of times and our model Eq. (3.9) captures this, we believe Eq. (3.9) to be a sufficient description of the problem.

3.2.2 Solving the Hybridisation Hamiltonian

We find the eigenstates of Eq. (3.9) by splitting it into 3 parts, region 1 ($x < 0$) and 3 ($x > l$) represent where excitations on either side of the junction are spatially separate and therefore propagate with no tunnelling or interaction. Region 2 ($0 <$

$x < l$, with $l \gg 1/k_F$) is the interface of the junction where the edge states on either side overlap and allow excitations to hybridise with a Γ-dependence. Region 1 and 3 are already diagonal in channel indices, the eigenvectors are therefore given by the plane waves:

$$\psi_m(x) = \begin{cases} \frac{1}{\sqrt{L}} \sum_k e^{ikx} a_{k,m} \text{ if } x < 0, \\ \frac{1}{\sqrt{L}} \sum_k e^{ikx} c_{k,m} \text{ if } x > l, \end{cases} \tag{3.11}$$

in the second region ($0 < x < l$, i.e along the interface) the Hamiltonian is not diagonal in channel index, we can, however, rotate to a diagonal basis given by

$$\psi_{1/2}(x) \to \psi_{\pm}(x) = \frac{1}{\sqrt{L}} \sum_k e^{ikx} b_{\pm,k}(x), \qquad \text{if } 0 < x < l. \tag{3.12}$$

$b_{\pm}(x)$ can be described in terms of superposition of annihilation operators in the channels $m = 1$ and $m = 2$ on either side of the interface these operators can be written as

$$b_{+,k}(x) = \frac{1}{\sqrt{2}} \big[e^{\frac{-i|\Gamma|x}{\hbar v_F}} b_{1,k} + e^{\frac{+i|\Gamma|x}{\hbar v_F}} b_{2,k} \big], \tag{3.13}$$

$$b_{-,k}(x) = \frac{1}{\sqrt{2}} \frac{|\Gamma|}{\Gamma} \big[e^{\frac{-i|\Gamma|x}{\hbar v_F}} b_{1,k} - e^{\frac{+i|\Gamma|x}{\hbar v_F}} b_{2,k} \big]. \tag{3.14}$$

The additional phase on these operators acts to shift k and ensures that $E = \hbar v_F k$. Furthermore we can include the effects of the flux penetrating the gap between the two modes by taking $b_{2,k} \to e^{i\phi x/l} b_{2,k}$, where $\phi = eBlw/\hbar$ is the total flux enclosed between the two modes along the junction interface and w is the separation of the two modes. We then join the two solutions at $x = 0$ by determining the $b_{\pm,k}(x)$ operators in terms of $a_{1/2,k}$-operators by ensuring the wave function is continuous

at $x = 0$,

$$\mathbf{b}_k(x) = \mathcal{S}(x)\mathbf{a}_k, \qquad \mathbf{b}_k = \begin{pmatrix} b_{+,k} \\ b_{-,k} \end{pmatrix}, \quad \mathbf{a}_k = \begin{pmatrix} a_{1,k} \\ a_{2,k} \end{pmatrix}, \tag{3.15}$$

$$\mathcal{S}(x) = \mathcal{S}_\Gamma(x)\mathcal{S}_\phi(x), \quad \mathcal{S}_\phi(x) = \begin{pmatrix} 1 & 0 \\ 0 & e^{i\phi x/l} \end{pmatrix}, \quad \mathcal{S}_\Gamma(x) = \begin{pmatrix} r(x) & t(x) \\ -t^*(x) & r(x) \end{pmatrix}, \tag{3.16}$$

with $r(x) = \cos\left(\frac{|\Gamma|x}{\hbar v_F}\right)$, $t(x) = \frac{i\Gamma}{|\Gamma|}\sin\left(\frac{|\Gamma|x}{\hbar v_F}\right)$. As expected $\mathcal{S}(x)\mathcal{S}(x) = \mathbb{1}$ as should be the case for any lossless scattering. Finally we ensure the wave function is continuous at $x = l$ and extract

$$\mathbf{c}_k = \mathcal{S}(l)\mathbf{a}_k, \qquad \mathbf{c}_k = \begin{pmatrix} c_{1,k} \\ c_{2,k} \end{pmatrix}. \tag{3.17}$$

This demonstrates an oscillatory interference pattern from the effect of hopping between the wires which is dependent on the length of the interface. We may then calculate the expected current using these eigenstates:

$$\langle I_i(x,t)\rangle \;=\; ev_F \langle : \psi_i^\dagger(x,t)\psi_i(x,t) : \rangle \tag{3.18}$$

To calculate the current at the drains (e.g $D1$) we input the eigenstates determined in Eq. (3.11) at the position of the detector, $x = x_{D1}$ with $x_{D1} > l$. We then relate the eigenstates back to the source using Eq. (3.17). At the source, the electrons are in contact with a thermal reservoir held at a chemical potential $\mu_1 = eV$ at $S1$ and

$\mu_2 = 0$ at $S2$,

$$\begin{aligned}\langle I(x_{D1},t)\rangle &= ev_F\frac{1}{L}\sum_{k_1,k_2}\mathcal{S}^{\dagger}_{\alpha 1}\mathcal{S}_{1\alpha}\left\langle :a_{k_1,\alpha}(t)a_{k_2,\beta}(t):\right\rangle \\ &= \frac{e^2V}{2\pi\hbar}|r|^2 \\ &= \frac{e^2V}{2\pi\hbar}\cos^2\left(\frac{|\Gamma|}{\hbar v_F}l\right) \end{aligned} \tag{3.19}$$

Note that $\mathcal{S}_{\alpha\beta}$ refers to the α,β element of the matrix $\mathcal{S}(l)$ given by Eq. (3.17) i.e $r = r(l)$. Three regimes appear here, the first corresponds to very weak tunnelling, $\Gamma/\hbar v_F \ll 1/l$, where we expect very few excitations to cross the junction. The current at $D2$ therefore remains close to that which we put in e^2V/h, from current conservation we determine the current at $D2$ to be zero. This is in agreement with the results of the experiments of [29].

In the regime where $|\Gamma|/\hbar v_F$ is comparable to $1/l$, this gives the interference regime. Single particle interference becomes the predominant determining factor for where each excitation emerges, the amount of current is very sensitive to the length of the junction. Experiments which are able to directly observe single particle interference via visibility fringes dependent on the magnetic flux between different channels [11], indicate they are likely in the interference regime. Though, as suspected for this particular regime, our simplified model is unable to fully reproduce the results of this experimental dependence on the magnetic flux. We can better replicate this regime by using a model in which impurities are treated independently which is appropriate providing they are separated by a length much greater than that of the Fermi length. We will look at this model in greater depth later.

When $|\Gamma|/\hbar v_F \gg 1/l$ the excitations oscillate from side to side many times across

the junction. Very slight changes in the gate voltages or magnetic field which will change the length of the interface/ the impurity landscape by small amounts resulting in large fluctuations to the probability of emerging at $D1$. Experimentally, the oscillatory $\cos^2$ averages out to $1/2$ and we obtain the current corresponding to a $50/50$ beamsplitter, $e^2V/2\hbar$ at both $D1$ and $D2$. We term this limit as the full hybridisation regime. Our model therefore implies that the experiments which found a quantised conductance [26, 28], are in this regime. The disorder potential in these experiment therefore meets the following condition,

$$\frac{1}{l}\int_0^l dx\, \Gamma(x) \gg \hbar v_F/l. \tag{3.20}$$

Similarly this averaging with a greater number of input channels leads directly to the equilibration indicated by Eq. (3.1). Within this scattering formulation we can also consider the noise across the junction using Eq. (3.16). We proceed to do so in the next section.

3.2.3 Noise Across a PN Junction

More can be learnt about the system from noise measurements, and therefore a better image of whether the model we put forward is correct can be learnt from this. The zero frequency cross-current noise can be expressed as,

$$S_{\alpha,\beta} \equiv \lim_{\tau\to\infty}\int_{-\tau/2}^{\tau/2} dt\, \langle I_\alpha(x_\alpha,t)I_\beta(x_\beta,0)\rangle - \langle I_\alpha(x_\alpha,t)\rangle \langle I_\beta(x_\beta,0)\rangle\,. \tag{3.21}$$

The current operators can then be expressed as,

$$I_\alpha(x,t) = ev_F : \psi_\alpha^\dagger(x,t)\psi_\alpha(x,t) : . \tag{3.22}$$

We evaluate the current noise at $D1$, given by S_{11} below,

$$\begin{aligned} S_{11} &= (ev_F)^2 \int dt \Big[\langle : \psi_1^\dagger(x_0,t)\psi_1(x_0,t) :: \psi_1^\dagger(x_0,0)\psi_1(x_0,0) : \rangle \\ &\quad - \langle : \psi_1^\dagger(x_0,t)\psi_1(x_0,t) : \rangle \langle : \psi_1^\dagger(x_0,0)\psi_1(x_0,0) : \rangle \Big] \\ &= (ev_F)^2 \int dt \Big[\langle \psi_1^\dagger(x_0,t)\psi_1(x_0,0) \rangle \langle \psi_1(x_0,t)\psi_1^\dagger(x_0,0) \rangle \Big]. \end{aligned} \tag{3.23}$$

We use the form of $\psi(x,t)$ given in the previous section and relate the operators at $D1$ back to the input states via elements of the scattering matrix. We then relate the expectations of the operators at the $S1$ and $S2$ to their given occupation value corresponding to a voltage of V coming from the reservoir attached to $S1$ and a grounded reservoir at $S2$, the entire system is assumed to be under a constant temperature.

$$\begin{aligned} S_{11} &= (ev_F)^2 \int dt \sum_{k_1,k_2,k_3,k_4} \mathcal{S}^\dagger_{\alpha 1}\mathcal{S}_{1\beta}\mathcal{S}_{1\gamma}\mathcal{S}^\dagger_{\delta 1} \langle a^\dagger_{\alpha,k_1}(t) a_{\beta,k_2}(0) \rangle \langle a_{\gamma,k_3}(t) a^\dagger_{\delta,k_4}(0) \rangle , \\ &= \frac{e^2}{2\pi\hbar} \big[eV|r|^2|t|^2 \coth\big(\frac{eV}{2k_BT}\big) + (|r|^4 + |t|^4) k_BT \big], \\ &= \frac{e^2}{2\pi\hbar} \big[eV \cos^2(\frac{|\Gamma|l}{\hbar v_F}) \sin^2(\frac{|\Gamma|l}{\hbar v_F}) \coth\big(\frac{eV}{2k_BT}\big) + (\cos^4(\frac{|\Gamma|l}{\hbar v_F}) + \sin^4(\frac{|\Gamma|l}{\hbar v_F})) k_BT \big], \end{aligned} \tag{3.24}$$

Note that $a_k(t)$ is simply an annihilation operator with a free fermion time dependence, $a_{\alpha,k}(t) = e^{-iv_Fk} a_{\alpha,k}$. The second, linear in temperature, term in Eq. (3.24) comes from equilibrium thermal fluctuations and is known as *Nyguist-Johnson* noise [92]. The first terms (referred to as shot noise) is the non-equilibrium contribution resulting from the discreteness of the electrons charge. We used that the a-operator are diagonal in momentum space and uncorrelated as to the source they originate from, i.e $\langle a^\dagger_{\alpha,k_1}(t) a_{\beta,k_2}(t) \rangle = \langle a^\dagger_{\alpha,k_1}(t) a_{\alpha,k_2}(t) \rangle \, \delta_{\alpha,\beta}\delta_{k_1,k_2}$. At constant temperature we may subtract off the Nyguist noise and discuss just the shot noise (excess noise). In

this case, it is useful to consider the Fano factor [92] given by,

$$F \equiv \frac{S}{e\,\langle I\rangle} \tag{3.25}$$

For our intermediate regime where, $\frac{|\Gamma|}{\hbar v_F}$ is comparable to $1/l$ we obtain a Fano factor given by the heavily length dependent term,

$$F = \sin^2(\frac{|\Gamma|l}{\hbar v_F}) \tag{3.26}$$

For the full hybridisation regime we assume that the shot noise tends toward its average value. Oscillatory terms in the shot noise and current average out and the Fano factor is given by the ratio of these averages,

$$F = \frac{1}{4} \tag{3.27}$$

We now are able to see a difference between our hybridisation region and a simple 50/50 beamsplitter (which would give $F = 1/2$). A distinction between the two would be impossible to make from a simple current measurement at the drains.

In the zero current transfer regime the shot noise term is reduced to zero and the Fano factor ceases to become a useful quantity. The linear temperature term becomes more important, our noise just reduces to the Nyguist-Johnson term describing equilibrium thermal fluctuations,

$$\lim_{|\Gamma|l/\hbar v_F \to 0} S_{11} = \frac{e^2 k_B T}{2\pi\hbar}. \tag{3.28}$$

We compare these results to experiment in the next section.

3.2.4 Comparison with Experiment

Probably the most in-depth experiment on shot noise for a PN junction in graphene in a high magnetic field was carried out by the Roulleau group [28]. They perform experiments for several lengths of junction interface ranging from $l = 5\mu$m to 100μm, with the primary focus being how much the length of the interface affects the noise and to see if the noise replicates that of a beamsplitter. As in the original experiments [26] they find that current in the bipolar regime is split equally over the number of edge modes i.e their experiments follow Eq. (3.1). In our analysis, this would suggest they were within the full hybridisation regime. Two graphs taken from their paper showing their results are given in Fig. (3.2).

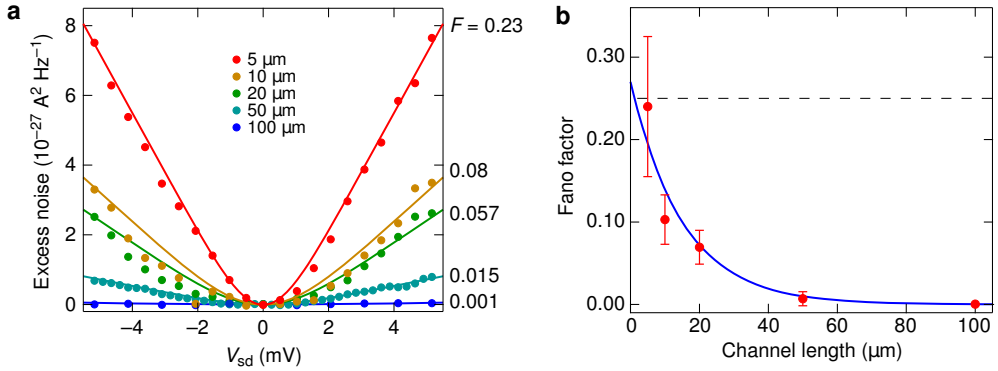

Figure 3.2: Graphs taken from [28] detailing the results of shot noise measurements on a PN junction with $|\nu_1| = |\nu_2| = 2$, graph (a) gives the excess noise ($\delta S \equiv S_{11} - S_{11}(V = 0)$) plotted against different biases (V_{sd}) applied to S1 for various length junctions, the Fano factors for each are plotted next to the best fit curves. The curves are assumed to fit a model [93] which assumes the distribution function is made up of a ratio of Fermi-Dirac functions where the ratio is determined by the number of edge modes originating from each source. Our model in the full hybridisation regime would similarly give this sort of distribution function, and therefore both models give the coth curves of the form $\delta S_{11} = 2eFgV \coth(eV/2k_BT)$. F, the Fano factor, is used as the fitting parameter. These Fano factors are then plotted in (b) against the length of the interface with a curve of best fit.

We first see that the best fit curves Figure (3.2a) are a good fit to coth curves, as our model would predict in the full hybridisation regime. We see that if they are

indeed within this regime then the Fano factor corresponding to $5\mu m$ ($F = 0.23$) is a good fit to what we predict ($F = 0.25$). Going to longer lengths the fit is less good, this probably an indicator that the assumptions that are in built into our scattering theory begin to fail. The authors [28] suggest the lowering of the Fano factor is due to the energy distribution coming from the two different sources relaxing into a equilibrium distribution in the centre of the junction. From just this 'cold' Fermi-Dirac distribution only thermal noise can emerge and the Fano factor goes to zero. This points us to where our assumptions break down, in Eq. (3.16) we assumed that an electron remains at the same energy when lower energy states are available. Realistically the electron is likely to relax into lower energy states by losing energy to environment and this is more likely to happen the longer the electron remains in the junction. The relaxation length must be larger than $l = 5\mu m$ however, and our single particle theory seems to fit well for lengths shorter than this.

It is worth pointing out that our calculations are at $|\nu_1| = |\nu_2| = 1$, i.e only the spin polarised $n = 0$ edge state is considered, where the other spin state is assumed to be pushed above the Fermi energy by Zeeman splitting. In the aforementioned experimental paper [28] the authors do not go to high enough resolution to observe Zeeman splitting and therefore use $|\nu_1| = |\nu_2| = 2$. Fortunately, in the absence of any magnetic impurities we can assume that spin is conserved in our edges so that an electron with spin-down can not be transmitted into the spin-up edge state. Under this assumption, this additional edge is trivial to include and simply gives double the noise and current, but leaves the Fano factor unchanged.

Unfortunately, to the best of our knowledge, experiments for noise within the interference and zero-current transfer regimes do not exist. From our analysis we can anticipate that one would expect to see large differences from the experiments of

Ref. [28]. In the zero current transfer regime we expect only Nyquist-Johnson noise, whilst in the interference regime we anticipate a large range of heavily l-dependent Fano factors i.e Eq. (3.26). In the most recent experiments on PN junctions in graphene published towards the end of 2017 [11] (measurements of current indicate they are in the interference regime) they provide compelling argument that the exchange between the two edge states only takes place at the entrance and exit of the junction in their set-up, i.e the tunnelling happens at the real edges. We may use this to improve our model by taking only two non-zero Γ_i's for $\Gamma(x) \equiv \sum_i \Gamma_i \delta(x - x_i)$in H_Γ (3.3), at $x_{1,2} = l, 0$, this identically returns the Mach-Zehnder model that was discussed in Section 1.2. As such it replicates the current calculations performed in this section, the results of which are given by Eq. (1.25) with $\Delta l \to 0$ as we assume the lengths of the different are equal in this case, due to them being equivalent to the length of the interface. These results are in line with the flux dependence in the current that ref. [11] see in their results. Had they performed noise experiments we would anticipate the measurement to coincide with results we expect from this model, to be complete we produce this, as well as the Fano factor, below. We again use the expression for S_{11} given by Eq. (3.23) but this time employing the eigenfunctions given by Eq. (1.16) to obtain,

$$S_{11} = \frac{e^2}{2\pi\hbar}\big[(|\mathcal{A}_{11}|^4 + |\mathcal{A}_{12}|^4)k_BT + |\mathcal{A}_{11}|^2(1 - |\mathcal{A}_{11}|^2)\coth\big(\frac{eV}{2k_BT}\big)\big]. \tag{3.29}$$

The calculation to produce this is given in depth in appendix B. As explained in the appendix, the matrix $\mathcal{A}$ describes the transfer matrix which maps excitations at the drains back to those at the sources. Here $\mathcal{A} = \mathcal{S}_B\mathcal{S}_A$ with $\mathcal{S}_{A,B}$ given by Eq. (1.18). We can therefore determine the elements which appear in Eq. (3.29) as,

$$\mathcal{A}_{11} = r_A r_B - t_A^* t_B e^{i\Phi_{AB}}, \qquad \mathcal{A}_{12} = t_A r_B + r_A t_B e^{i\Phi_{AB}}. \tag{3.30}$$

Considering just the 'excess noise' (i.e subtracting off the linear temperature contribution) we can obtain a Fano factor given by Eq. (3.31)

$$\begin{aligned} F &= (1-|\mathcal{A}_{11}|^2)\coth\big(\frac{eV}{2k_BT}\big), \\ &= \big[|r_A|^2|t_A|^2+|r_A|^2|t_B|^2+2|r_Ar_Bt_At_B|\cos(\Phi_{AB})\big]\coth\big(\frac{eV}{2k_BT}\big), \end{aligned} \tag{3.31}$$

The same concepts shown here in the MZI model can be used for any number of impurities providing that the distance between each impurity is much greater than the Fermi length. Representing each impurity as a scatterer is therefore a good tool for analysis in the intermediate limit ($|\Gamma| \sim \hbar v_F/l$) where we expect our hybridisation model fails to be a good description. Of course, this approach also requires knowledge of the specifics of the impurities. If this is not the case, we must refer to the methods given by Eq. (3.10).

In conclusion, we are able to unify several apparently conflicting experiments within one model where the apparent differences are the result of a variability in the value of $\Gamma(y_0, y_0')$, Eq. (3.5), which is based upon the distance two modes are from each other as well as amount of (lattice-length scale) disorder. Whilst we find broader disorder is not directly relevant to the coupling of edge modes of different pseudo-spins, it does play a role, along with temperature, magnetic field and top/bottom gate potentials, in broadening of individual modes. This results in a greater overlap between modes of different pseudo-spin and therefore a larger Γ. We predict what further experiments on noise would expect to see within different regimes. So the final question to ask is why is Γ so different for the different subsets of experiments?

3.2.5 Variability of Disorder Induced Tunnelling

The simplest answer one is drawn to is to say that the experiments performed in the quantised regime are simply more disordered and therefore have a larger Γ than those in the interference/zero current transfer regimes, we believe this to be only part of the truth. Actually an important difference between those in the quantised regime and those that are not is the amount of individual edge states they are able to resolve. Quantised current experiments [26, 28, 90], all show results where the lowest number of edge states they give data for is $|\nu| = 2$, that is they do not observe the Zeeman splitting of the Landau levels. Experiments *not* in the quantised regime [29, 11] do not only observe Zeeman splitting, i.e they can resolve $|\nu| = 1$, they also observe the full effect of K/K' symmetry breaking meaning they observe a Hall plateau which corresponds to $\nu = 0$. The 'width' of each Landau level (and therefore the ease to which we can distinguish them) is based on three factors, the most obvious of these is the magnetic field. $l_B \propto 1/\sqrt{B}$ directly appears in the electronic wave function and determines how 'spread' each state is, a lower magnetic results results in a greater overlap of neighbouring states and therefore a higher $\Gamma(y_0, y_0')$. The other two factors result in broadening of the edge modes by making a broader range of neighbouring states within the same energy band branch more accessible, these are: the temperature (we estimate this broadening to be $\propto T \times l_B$) and the amount of long-length scale disorder (resulting from impurities and scattering from the lattice). Additionally if we discuss specifically the artificial edge modes along the PN junction (rather than the states at the physical edge) there is another factor based upon the length scale at which the voltage between top and bottom gate changes, a more abrupt change will allow temperature and disorder broadened state to have a greater overlap between different 1D modes.

Let us consider which of these factors could be the largest contributor in the case

of these experiments. All experiments were performed at roughly the same field strength (7-14 T), l_B is therefore unlikely to play a role. Using mobility as a measure of disorder, we can compare the amount the disorder in graphene samples used in the original quantised experiments [26] (mobility given by $\mu = 7 \times 10^4 \text{cm}^2/\text{Vs}$ in this case) and $\mu = 1.2 \times 10^5 \text{cm}^2/\text{Vs}$ in the zero quantised regime results found by [29]). This improvement in quality (due to the 7 year gap between the papers) may have an effect on the original papers results but for more recent quantised work [28, 90] it seems unlikely to explain the differences. Temperature may play a role here, the experiments of Ref.[28, 90] were performed at 4K, at least an order of magnitude greater than the un-quantised conductance seen by [29, 11] (with Wei *et al.* going as low as 20mK for some of their results). Other differences particularly those between the MZI-style current [11] and that with no current transfer [29] may result from the voltage profile of the top gates, as was pointed out by [11] they use a sharper changing electrical potential which may result in the tunnelling seen in this case. In the next section of this thesis we proceed to discuss Wei *et al.* [11] results in greater depth. We particularly focus on what differences we might expect from an electronic Mach-Zehnder in graphene and those already built in other 2D semi-conductors [12, 41, 94].

3.3 Mach-Zehnder Interferometer in Graphene

The rest of this chapter is dedicated to the Mach-Zehnder in graphene. We first consider the results of Ref. [11] (thus far the first and only experiment which has been able to produce such a device) and comment on some key differences from what is seen in MZI's in semi-conductors. We then we go on to consider a previously unconsidered (to the best of our knowledge) extension to the model for an electronic MZI. Models for MZI where interactions could take place within the same channel

drew quite a lot of interest [30, 50, 31, 95, 51, 53], we extend this to also include interactions within different arms. We believe this, unlike in semi-conductor MZI where different arms are well separated, may play a role in the MZI in graphene. One of the most interesting features of paper [11] is the staggering visibility, Eq. (5.14), they are able to reach. After 15 years of improvements of Mach-Zehnders in conventional 2D semi-conductors the visibility of the devices (probably the best quantifier of their quality) has improved from 65% in the original experiments [42] to 95% in experiments performed more recently [49]. We can contrast this to the *first* (and only) experiments in graphene where they observe a visibility of 98% [11]. This seem likely to be result of the fact the different channels/arms in the graphene Mach-Zehnder take very similar routes unlike those in conventional semi-conductors. In graphene the two channels co-propagate and any longer length-scale phonons and impurities will interact with both channels. Since these interact with the electrons in both channels in a similar way it means any defects carry less information about the position of the electron then would be the case in semi-conductors and therefore cause less dephasing. Interacting electrons in graphene in a high magnetic field have been discussed [64, 68, 96, 97, 78] mostly as an explanation for the K/K' Landau level splitting which has been observed in experiments [10, 11, 29, 76]. There has been some discussion of Luttinger liquid at the graphene edge [98, 25], but since it can only result in forward scattering it is not usually very relevant. Interactions within the one dimensional channel along the graphene PN junctions have not been discussed however so we will begin this section with consideration of the relevant interactions.

3.3.1 Including Interaction

This section provides formalism which allows for the inclusion of interactions both across (inter-channel interaction) channels and within the same same channel (intra-

channel interaction) of the modes which flow down the PN junction interface in graphene. This provides a framework where all different interactions may be considered, we then go on in the section following this one to consider in depth the simplest case in which we only have a single channel on each side of the junction, $\nu_1 = -1, \nu_2 = 1$.

Having extracted that at low temperature and low energies our excitations along the PN junction are indeed those of one dimensional fermionic channels, we may wonder what effect interactions can have on this. Forgetting, for a moment, the K/K' symmetry breaking discussed in Section 2.4, if we consider the $\nu_1 = 1, \nu_2 = -1$ case the K/K' sit *on top* of each other; we might therefore expect that the cross channel interactions to have an effect on the dynamics. In reality, of course, we see that this symmetry is invariably broken and N and P channels will be separated, the degree to which they are separated will then determine the strength of the interaction via the overlap in the y-direction that will originate in these matrix elements (e.g for coupling the zeroth Landau levels the matrix elements are weighted by a term $\sim \int dy\ \phi_0^*(y - y_0)\phi_0(y - y_0'))$. This leads to another interesting feature of the system; we can, to some degree, control the strength of interaction between different valleys, by manipulation of the magnetic field and applied potential as this will determine the overlap of the wave functions. From Section 1.3.1 we are equipped with the knowledge of how one can deal with interacting 1D Hamiltonians. The bosonisation technique should allow us to bring an interacting Hamiltonian into quadratic form. This is detailed in the section following this one. First we will catalogue the different interactions in a formalism sometimes referred to as *g-ology* [99]. We consider only *chiral* interactions, the opposite direction movers are largely spatially separated so what are usually considered the standard g_1, g_2, g_3-processes (which just refer to interactions between electrons moving in different directions)

drop to zero. Since interaction between different L/R movers are irrelevant in our case we will re-purpose this notation to refer to interaction matrix elements between different chiral states. In this notation we have a set of possible interactions described by $\{\mathbf{g}\} = \{\mathbf{g}_1, \mathbf{g}_2, \mathbf{g}_3, \mathbf{g}_4\}$ which are depicted in Fig. (3.3). Each type of interaction can then be broken up into those between states belonging to different Landau levels (described by i and j), pseudo-spins (n or m) and spins (σ and σ') e.g $\mathbf{g_2} \equiv g_2^{ij,nm,\sigma\sigma'}$. In the next section we will again focus our attention on the simplest situation of the lowest two levels, this is given by the zeroth Landau level $i = j = 0$, opposite pseudo-spin $n = K, m = K'$ and same spin modes $\sigma = \sigma'$, we will refer to this set of interaction variables without any mode indices, $g = \{g_1, g_2, g_3, g_4\}$. Of this set the g_3 describes an umklapp style process [91] where a pair of electrons close to one Dirac point are scattered outside of the Brillouin zone into states close to a different Dirac point. Such an interaction (for any excitations with different pseudospin) cannot be reconciled with momentum conservation and therefore we may always take $g_3 = \mathbf{g}_3\big|_{n\neq m} = 0$. In fact of the components of $\mathbf{g}_3$ the only terms that are in general allowed by momentum conservation are those that are completely diagonal in energy band indices, since these terms are identical to $\mathbf{g}_4$ type terms we may simply absorb those $\mathbf{g}_3$ processes into $\mathbf{g}_4$, we will therefore exclude $\mathbf{g}_3$ processes from now on.

Whilst we have thus far not made any assumptions about the range of these interactions, from now on we will consider only contact interactions (δ-function like in space). For cross-valley interactions this is easy to justify, the cross-valley interaction matrix elements (similar to our disorder mediated tunnelling terms) are always accompanied by a fast oscillating term, $e^{i(\mathbf{K}-\mathbf{K}')\cdot\mathbf{\Delta r}}$ where $\mathbf{\Delta r}$ describes the distance between the interacting excitations. Any long range potential is therefore killed upon interaction with this term and only contact interactions can survive. Where

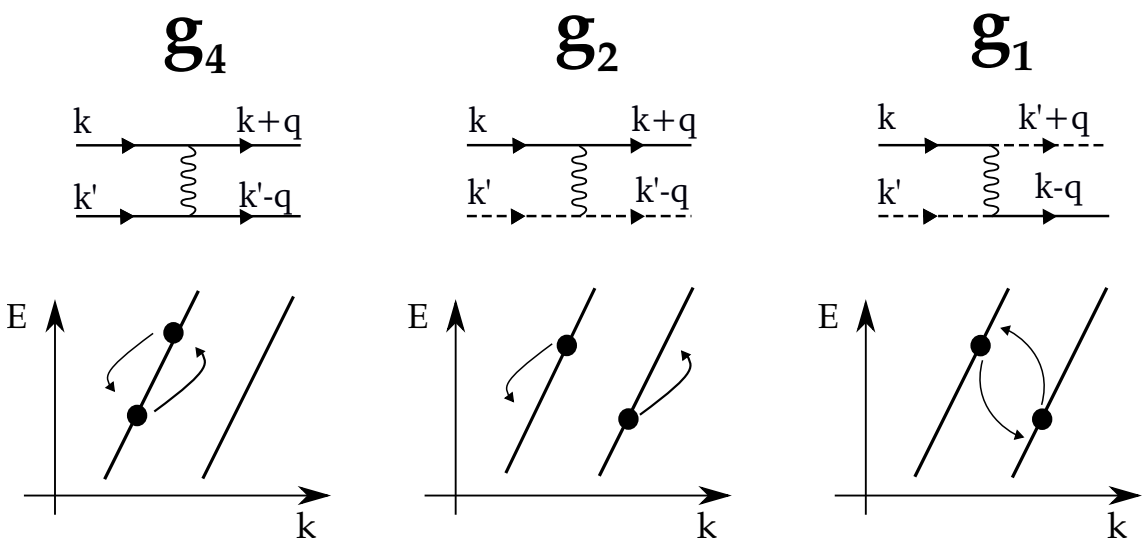

Figure 3.3: Three different types of interactions are depicted above $\mathbf{g}_4, \mathbf{g}_2$ and $\mathbf{g}_1$. The bottom set of images depicts two energy bands which may correspond to different Landau levels, different pseudo-spin or different spin. $\mathbf{g}_4$ is diagonal in these indices meaning that it describes interactions where the excitations belong to the same energy band, $\mathbf{g}_2$ describes interactions between excitations on different energy bands but where the excitations remain close to their original momentum after interaction. $\mathbf{g}_1$ processes also describe excitations belonging to different branches, but in this case the excitations swap branches upon interaction. For $\mathbf{g}_1$ processes involving different K/K' branches, this is a large momentum transfer process. The upper row of images depicts the momentum transfer for these styles of interaction, where the solid/dashed black lines denotes that the electron states belong to different energy bands. Not depicted here are the $\mathbf{g}_3$-interactions, which scatter electrons outside of the Brillouin zone.

interacting excitations aren't separated by a large distance in reciprocal space (e.g $\mathbf{g}_4$ processes) it is not so obvious that such an argument still holds. However, providing we consider only the low energy properties, small momentum transfer interactions (contact interactions in real space) are still likely to be the dominant type of interaction and therefore this assumption is still reasonable. In the next section we use the formulation built above to consider how interaction is included in the Hamiltonian describing the simplest example along the PN junction, $\nu_1 = -1, \nu_2 = 1$. We calculate the interacting correlation function along the PN junction in this case, we then proceed to use this in the following section to calculate the current in model

of an electronic Mach-Zehnder with previously unconsidered interactions included.

3.3.2 The Interacting Correlation Function

We first consider the Hamiltonian describing the electrons as they propagate down the centre of our PN junction. For now we leave out the effects of tunnelling. The Hamiltonian can essentially be split into three parts. H_1 and H_2 describe the particles on either side of the junction which we write via Eq. (1.40) in bosonised form in terms of the density. This is given by Eq. (3.32), where g_4 describes the strength of interactions of electrons of the same pseudo-spin (inter-channel interaction strength). H_{int} then describes the interaction across the junction, with g_2 and g_1 describing the only relevant cross-channel interactions ($g_3 = 0$ due to momentum conservation).

$$H_m = \pi v_F \int dx \rho_m^2(x) + \frac{g_4}{2} \int dx \rho_m^2(x) + \frac{\pi \hbar v_F}{L} \hat{N}_m \tag{3.32}$$

$$H_{\text{int}} = \int dx (g_2 - g_1) \rho_1(x) \rho_2(x) \tag{3.33}$$

$$H_0 = H_1 + H_2 + H_{\text{int}} \tag{3.34}$$

It is easy to see in this form that the effect of intra edge interactions simply renormalises the velocity $u = v_F + \frac{g_4}{2\pi}$, immediately giving a route to solving the inter-channel only MZI model. In ourcase, we still have a problem with the non-diagonal g_1, g_2 terms however. To continue, we wish to switch to a basis in which the Hamiltonian is diagonal, in this spirit we introduce the variables:

$$\rho_+(x) = \frac{1}{\sqrt{2}}(\rho_1(x) + \rho_2(x)), \qquad \rho_-(x) = \frac{1}{\sqrt{2}}(\rho_1(x) - \rho_2(x)). \tag{3.35}$$

$\rho_+(x)$ describes the total density in both edges at a position x, where as $\rho_-(x)$ describes the difference between densities on either side of the junction (this can

also be thought of as 'total pseudospin' or the density disparity between electrons near K and those near K', it also relates to the current at a particular drain since K and K' electrons supply different drains). The Hamiltonian is diagonal in this basis, but these fields acquire different velocities, $u_\pm = u \pm \frac{g_2-g_1}{2\pi} = v_F + \frac{g_4}{2\pi} \pm \frac{g_2-g_1}{2\pi}$.

$$H_0 = \pi u_+ \int dx \rho_+^2(x) + \pi u_- \int dx \rho_-^2(x) + \sum_m \frac{\pi \hbar v_F}{L} \hat{N}_m \tag{3.36}$$

One can then convert this Hamiltonian into the language of bosonic operators by recalling the standard *bosonisation dictionary* produced in section 1, specifically here we refer to Eq. (1.34).

$$\rho_\eta(x) = \partial_x \phi_\eta(x) + \frac{2\pi}{L} \hat{N}_\eta \tag{3.37}$$

Here one makes use of the commuting fields which can be defined as follows,

$$\phi_\pm = \frac{1}{\sqrt{2}} \big[\phi_1(x) \pm \phi_2(x)\big], \qquad \big[\phi_n(x), \partial_y \phi_m(y)\big] = -2\pi i \delta_{nm} \delta(x-y). \tag{3.38}$$

This allows the construction of the Hamiltonian in terms of the bosonic operators as below,

$$H_0 = \sum_\pm \frac{\pi \hbar u_\pm}{L} \hat{N}_\pm (\hat{N}_\pm + \frac{2v_F}{u_+}\delta_+) + \sum_{q>0} \sum_\pm \hbar u_\pm q \; b_\pm^\dagger b_\pm, \qquad \hat{N}_\pm = \frac{N_1 \pm N_2}{2}. \tag{3.39}$$

We can simplify this slightly if we take it to be the case that the fluctuations of $\hat{N}_{1,2}$ are small, in which case we may linearise the $\hat{N}_\pm$ about their expectation value $\langle \hat{N}_\pm \rangle = \frac{L\mu_\pm}{2\pi\hbar v_F}$. In this case, and omitting unnecessary constants, the Hamiltonian is given by,

$$H_0 = \sum_\pm \frac{u_\pm}{v_F} \mu_\pm \hat{N}_\pm + \sum_{q>0} \sum_\pm \hbar u_\pm q \; b_\pm^\dagger b_\pm, \tag{3.40}$$

Whilst Klein factors do not appear here, it will prove useful to also define a new set of these operators describing the new '+/-' excitations as follows,

$$F_- = F_2^\dagger F_1, \qquad\qquad F_+ = F_1 F_2. \tag{3.41}$$

In this case these operators satisfy the same commutations relations as before,

$$[\hat{N}_n, F_m^\dagger] = \delta_{nm} F_m^\dagger, \qquad\qquad [\hat{N}_n, F_m] = -\delta_{nm} F_n, \tag{3.42}$$

where $n, m = +, -$. We therefore have all the necessary framework to construct a fermionic field operator in the diagonal basis which is related to the above Klein Factors and bosonic field in the usual way,

$$\psi_m(x) = \frac{F_m}{\sqrt{2\pi\epsilon}} e^{i2\pi \hat{N}_m x/L} e^{i\phi_m(x)}, \qquad\qquad m = +, -. \tag{3.43}$$

Using techniques from [30] we may then use the form of the field operator above to calculate the Greens function for these $\pm$-excitations,

$$\begin{aligned} G_\pm(x,t) &= \langle \psi_\pm^\dagger(x,t)\psi_\pm(x,t)\rangle\,, & (3.44)\\ &= \frac{1}{2\pi\epsilon} e^{-i\mu_\pm x/(\hbar v_F)} \langle F_\pm^\dagger(t) F_\pm(0)\rangle \langle e^{i\phi_\pm(x,t)} e^{i\phi_\pm(0,0)}\rangle\,. & (3.45)\end{aligned}$$

We can then evaluate the two expectation values separately. We will use the interaction representation so that the time dependence of an operator is given by $\mathcal{O}(t) = e^{iH_0 t/\hbar}\mathcal{O}e^{-iH_0 t/\hbar}$. The expectation value of the Klein operators can be performed by permuting the $\hat{N}$ dependent part of the time evolution operator past the Klein factors using the relations in Eq. (3.42) to give,

$$\langle F_m^\dagger(t) F_m(0)\rangle = e^{i(u_m/v_F)\mu_m t/\hbar}, \tag{3.46}$$

The bosonic part of the correlator (3.45), is slightly more involved but nonetheless can be evaluated using standard techniques.

$$g_m(x,t) = \frac{1}{2\pi\epsilon}\langle e^{i\phi_m(x,t)}e^{-i\phi_m(0,0)}\rangle \equiv \frac{1}{2\pi}e^{S_m(x,t)}. \tag{3.47}$$

S_m can then be written in the form below by using that the Hamiltonian is quadratic in the bosonic variables [91]. S_m may then be explicitly evaluated.

$$\begin{aligned} S_m(x,t) &= -\ln\epsilon - \frac{1}{2}\langle\big[\phi_m(x,t)-\phi_m(0,0)\big]^2\rangle + \frac{1}{2}\big[\phi_m(x,t),\phi(0,0)\big], & (3.48)\\ &= -\ln\epsilon - \sum_{q>0}\frac{1}{n_q}e^{-\epsilon q}\big[1-e^{-iq(x-u_m t)}\big], \qquad T\to 0, & (3.49)\\ &= -\ln\big[i(x-u_m t)+\epsilon\big], & (3.50) \end{aligned}$$

Here we have substituted the mode expansion of ϕ_m, given by Eq. (1.33) and evaluated the bosonic expectation values as a Bose-Einstein distribution at $T \to 0$ in order to obtain the second line (more details of this calculation can be found Appendix C). We then made use of Eq. (C.3) to perform the summation to obtain the third line. From the above we can finally deduce the interacting, zero temperature, Greens function for the $\pm$ excitations as,

$$G_m(x,t) = \frac{1}{2\pi i}\frac{e^{i\mu_m(x-u_m t)/\hbar v_F}}{x-u_m t - i\epsilon}, \tag{3.51}$$

i.e it is the same as what we expect for non-interacting electrons but with the velocity altered by interactions. In the next section we will add tunneling between channels perturbatively and see if the cross channel interactions have any effect on the interference patten.

3.3.3 Current in Mach-Zehnder with Cross Channel Interactions

As was previously the case, to build our Mach-Zehnder model we add a tunnelling term to couple the two interacting quantum wires,

$$H_{\text{tun}} = \Gamma_a \psi_1^\dagger(0)\psi_2(0) + \Gamma_b \psi_1^\dagger(l)\psi_2(l) + \text{h.c.} \tag{3.52}$$

Here we fix the location of the tunnelling points to be the same place, as the junction is the same length for both excitations. From this we can construct our full Hamiltonian by $H = H_0 + H_{\text{tun}}$, where H_0 is given by Eq. (3.34). We then wish to see the impact the cross-channel interaction may have on the interference pattern, as such we are interested in the current at the drains, $D1$ and $D2$. For the rest of this section we heavily rely on the work of ref. [30] who considered a similar model to ours but with only intra-channel interactions. Following their method, we may deduce the current at the drains by obtaining the tunnelling current describing electron current going from channel 1 to channel 2,

$$\begin{aligned} \hat{I} &= -e\frac{d}{dt}\hat{N}_1 = -\frac{-ie}{\hbar}[H, \hat{N}_1] = \frac{ie}{\hbar}[H, \hat{N}_2] && (3.53)\\ &= \frac{e}{\hbar}\big\{i\Gamma_a \psi_1^\dagger(0)\psi_2(0) + i\Gamma_b \psi_1^\dagger(l)\psi_2(l) + \text{h.c}\big\} && (3.54) \end{aligned}$$

Using the form of the charge operator and the commutation relations given below

$$\hat{N}_m = \int dx \hat{\rho}(x),$$

$$\{\psi_m(x), \psi_{m'}^\dagger(x')\} = \delta_{m,m'}\delta(x - x') \qquad \{\psi_m(x), \psi_{m'}(x')\} = 0,$$

The expectation value for current at time t is then given by,

$$I(t) = \langle \mathcal{U}(-\infty, t)\hat{I}(t)\mathcal{U}(t, -\infty)\rangle \,. \tag{3.55}$$

Where $\mathcal{U}(t_2, t_1)$ describes the time evolution, which in the representation we are using is given as $\mathcal{U}(t_2, t_1) = T_t \exp\left[\frac{i}{\hbar}\int_{t_1}^{t_2} H_{\rm tun}(t)dt\right]$, we treat tunnelling perturbatively and expand to lowest order in Γ. Taking our measurement time of the current to be $t = 0$ gives

$$I(t=0) = -\frac{i}{\hbar}\int_{-\infty}^{0} dt\, \langle[\hat{I}(0), H_{\rm tun}(t)]\rangle \,. \tag{3.56}$$

This boils down to the combination of two point correlation functions of the form below, which we then calculate by switching to the diagonal bosonic representation,

$$\begin{aligned} & \langle\psi_1^\dagger(x,t)\psi_2(x,t)\psi_2^\dagger(x',t')\psi_1(x',t')\rangle \\ = \;& \frac{1}{(2\pi\epsilon)^2} e^{-i\frac{\mu_-}{\hbar v_F}(x-x')} (\langle F_-^\dagger(t)F_-(t')\rangle \, \langle e^{i\sqrt{2}i\phi_-(x,t)} e^{-i\sqrt{2}\phi_-(x',t')}\rangle \,, \\ = \;& e^{-i\frac{\mu_-}{\hbar v_F}(x-x'-u_-(t-t'))} \big[g_-(x-x', t-t')\big]^2. \end{aligned} \tag{3.57}$$

We may then deduce the current at $D2$ by expressing the correlation functions which will ultimately appear in the expression given by Eq. (3.56) as,

$$\begin{aligned} I_V &= -\frac{2e}{\hbar}\int_{-\infty}^{\infty} dt\, \left[\big(|\Gamma_a|^2 + |\Gamma_b|^2\big)e^{-iu_-\mu_- t/\hbar}\right](i)\mathrm{Im}\big[g_-(0,t)^2\big], \\ &\quad + \big\{\Gamma_a\Gamma_b^* e^{i\mu_- l/v_F\hbar} e^{-iu_-\mu_- t/v_F\hbar}](i)\mathrm{Im}[g_-(l,t)^2\big] + c.c\big\} \\ &= \frac{e^2 V}{h}\left[|\tilde{t}_a|^2 + |\tilde{t}_b|^2 + 2|\tilde{t}_a\tilde{t}_b|\cos(\Phi)\right]. \end{aligned} \tag{3.58}$$

where $\tilde{t}_c \equiv \Gamma_c/\hbar v_F$ is the tunnelling probability to first order in Γ_c, see Eq. (1.19), and we've taken $\mu_- \equiv \mu_1 - \mu_2 = eV$, finally we also used $|\Gamma_a\Gamma_b| = \Gamma_a\Gamma_b e^{i\Phi}$. The time integrals can be performed by evaluating the residue at the second order poles

coming from $g^2_-(x,t)$. Comparison to Eq. (1.25) reveals that there aren't any differences made by including the interactions to first order in tunnelling. We simply replicate the MZI current in the limit that $\Delta l, T \to 0$ and tunnelling is small. Since, as detailed in our discussion earlier, we only expect contact interactions to be relevant for any cross-valley interactions, we conclude that cross channel interactions cannot influence the current at the drains in the small tunnelling limit.

This problem lends itself to several interesting extensions which we unfortunately do not have time to explore, one example being similar to the work of Ref. [50], in which the authors solved *exactly* (i.e with tunnelling not treated perturbatively) a model of interacting MZI for which interactions (intra channel only) existed only between the two scatterers for certain choices of interaction. They did so by *refermionising* [24] their bosonic Hamiltonian into a new set of fermionic variables for which the Hamiltonian was quadratic and diagonal. It would have been interesting to see if such an exact solution could have also been found for our problem, and whether cross-channel interactions would have had more of an effect in the non-perturbative limit. A further interesting addition would have been to see the effects longer range inter-channel interactions had on these results. This was considered in the intra-channel only MZI model in Ref. [30], and produced results which were much more experimentally relevant than a simple contact interaction only model. However the similarities of Eq. (3.58) to that calculated in Ref. ([30]) would imply that inclusion of long-range cross channel interaction to their results would make very little difference and furthermore, as previously stated, we expect any long range cross channel interactions to be totally irrelevant along the PN interface.

3.4 Conclusion

In this section we have made use of the 1D modes that were shown to exist in chapter 2 to describe a PN junction in a strong magnetic field in graphene from source to drain. We found that this model was insufficient to explain experiments observed in these systems and inferred the presence of a disorder potential, $\Gamma(\mathbf{r})$ which could couple the modes at the junction interface. In Section 3.2.1, we considered a simplified version of a model with disorder in which we averaged $\Gamma(\mathbf{r})$ along the junction interface. We found that this model well replicates experiments in the limit the disorder along interface is very strong or very weak and its variability succeeds in explaining the differences appearing in several conflicting experiments. The model does fail to capture some of the intricacies of the system in the immediate limit (specifically it doesn't replicate interference effects well). In this case we proposed to use a description similar to the standard model of an electronic MZI (the detail of which were discussed in Section 1.2) and proposed the noise measurements which experiments in this limit should see if this model is an accurate description.

We proceeded to discuss which interaction effects are most relevant along a PN junction in graphene and from this produced the correlation function for the natural (diagonal) excitations which propagate along the PN interface in the case where we have $\nu_1 = -1, \nu_2 = 1$. We found that additional interactions might be relevant to a graphene MZI model, which are not relevant to an MZI in a conventional semi-conductor. We considered whether these effects would have any impact on the current. In the small tunnelling limit we found they did not, and that such cross-channel interactions do not appear to have much more of an impact on the system than intra-channel only interactions do.

In the next chapter we encroach on the world of quantum information and introduce the recently popularised topic of *quantum discord*. Having introduced the topic we will, in Chapter 5, make use of the extensively discussed electronic MZI to propose a completely original way of generating and detecting quantum discord in a solid-state systems.

Chapter 4

Quantum Discord

Our previous in depth discussion of building an electronic *Mach-Zehnder* in condensed matter may leave an especially cynical reader with one increasing overwhelming question: *"What's the point?"* The author would feel a little deflated by such a question, we would hope that the rich physics which has been demonstrated to go into creating such a device is reason enough for an interest in it. But nonetheless, we are quick to illustrate where such a device would come in handy. Just as the birth of the field of *Quantum Optics* led to an array of interesting quantum phenomena being displayed, *Quantum Electro-Optics* can do the same. Electrons have one very important advantage over photons: they are charged. This means our electronic Mach-Zehnders can be used as very sensitive measuring devices for anything involving charged particles [44, 100, 94, 101, 102]. As a further demonstration as to where our Mach-Zehnder might be useful we encroach on the realm of quantum information, specifically a recently popularised topic which has received a great deal of attention, *quantum discord* [103]. Despite the recent flurry of activity in the field, construction of a measure to detect its presence in a system has proven difficult [20]. The propositions that do exist are limited in scope [20, 104] or very complex [105] which has led to limited experimental progress [106, 107]. Within the frame

work of the electronic Mach-Zehnder we are able to propose a way in which one can build states which have a controllable degree of discord, and then, by observation of cross-correlation functions, we devise a protocol which will determine if the state is discorded or not. From this protocol we build a measure which bears a surprisingly strong resemblance to discord. In this initial chapter we introduce what is meant by the terms 'quantum correlated' and 'quantum discord', and give some background to *discord witnesses*. The following chapter will then return to using our beloved electronic Mach-Zehnder as a tool to detect discorded states in a solid state set-up.

4.1 Correlations in Classical Probability Theory

Quantum discord has its origin routed in classical probability theory. In classical information theory we quantify how much uncertainty there is around a random variable before we measure it in terms of its *Shannon Entropy* [108]. Consider the random variable A which may take the values a_i, our *ignorance* about what value the variable will take prior to measuring it can be quantified by

$$H(A) \equiv -\sum_i p_{A=a_i} \log p_{A=a_i} \tag{4.1}$$

The correlation between two random variables A and B, described by a joint probability distribution $p_{A,B}$, may by quantified by the degree to which the uncertainty about one of these variables is reduced when we have knowledge of the other. The reduction in our ignorance of A, given knowledge of B's probability distribution, is given by the *mutual entropy*,

$$J(A:B) \equiv H(A) - H(A|B), \tag{4.2}$$

where $H(A|B) = \sum_i p_{B=b_i} H(A|B = b_i)$ is the conditional entropy of A given B. The single variable probability distribution can be derived from the joint one by tracing out the unused variable,

$$p_A \equiv \sum_i p_{A,B=b_i}, \qquad p_B \equiv \sum_i p_{A=a_i,B}. \tag{4.3}$$

The conditional probability is then obtained via Bayes' theorem,

$$p_{A|B=b_i} = p_{A,B=b_i}/p_{B=b_i}. \tag{4.4}$$

It is this distribution we may substitue into Eq. (4.1) to obtain $H(A|B = b_i)$. Furthermore we can use Bayes' theorem to obtain an alternative (but completely equivalent) expression for the mutual entropy,

$$I(A : B) \equiv H(A) + H(B) - H(A, B) \tag{4.5}$$

where $H(A, B) = -\sum_i \sum_j p_{A=a_i,B=b_j} \log p_{A=a_i,B=b_j}$. So equivalently we can describe the degree of correlation between A and B random variables by considering the amount of uncertainty we have about them separately minus the amount of uncertainty their joint probability distribution gives. For an uncorrelated pair of random variables $H(A, B) = H(A) + H(B)$, and the mutual entropy just returns zero.

4.2 Correlations in Quantum Theory

The idea of Olivier and Zurek [109, 15] and, independently Henderson and Vedral [16], was to generalise the above concepts to quantum systems in order to be able to characterise the correlations between two parts of a composite system. Shannon

entropy is used to describe the uncertainty associated with a probability distribution for a classically random variable. The uncertainty about a given quantum state ρ can be described by the Von Neumann Entropy [110]:

$$S(\rho) \equiv -\operatorname{Tr}(\rho \log \rho) \tag{4.6}$$

Using this, we may then construct the 'quantum version' of mutual entropy. We first make use of the analogue to our reduced probabilities, Eq. (4.3), which give us the reduced density matrices,

$$\rho^A \equiv \operatorname{Tr}_B\{\rho^{AB}\}, \qquad \rho^B \equiv \operatorname{Tr}_A\{\rho^{AB}\}. \tag{4.7}$$

Physically it is not obvious that these operators necessarily correspond to anything meaningful in terms of a description of the individual subsystem, the justification is that they give the correct results for measurements which impact one of the subsystems only [108]. For example, an operator which only impacts the B-subsystem can be represented as $\hat{\mathbf{O}}^B = \hat{O}^B \otimes \mathbb{1}^A$, taking the full trace with this operator is equivalent to taking the trace over B on the reduced density operator with $\hat{O}^B$, i.e. the reduced density matrix gives the correct dynamics for operators that only impact the B-subsystem.

The analogue of the expression for $I(A:B)$, Eq. (4.5), is then easily obtained,

$$\mathcal{I}(\rho^{AB}) \equiv S(\rho^A) + S(\rho^B) - S(\rho^{AB}). \tag{4.8}$$

In the quantum context we will continue to refer to this quantity as *mutual entropy*. The quantity gives a description of the total correlation between the A and B subsystems. The quantum analogue of the conditional probabilities present a slight

difficulty, the result of a 'measurement' will depend on the basis we pick for our measurement projectors. Nonetheless we can define a density matrix conditional on some measurement on B as follows [109, 15],

$$\rho_{A|\Pi_i^B} \equiv \frac{\Pi_i^B \rho^{AB} \Pi_i^B}{\mathrm{Tr}_{A,B}\{\Pi_i^B \rho^{AB}\}} \tag{4.9}$$

Where the denominator normalises the conditional density matrix. The operator $\Pi_i^B = |b_i\rangle \langle b_i|$ is a projector which enforces the detection state onto the density matrix. The denominator is therefore the probability of finding the state of B as $|b_i\rangle$, it is therefore the QM representation of the classical probability $p_{B=b_i}$,

$$p_{B=b_i} \to p_i^B \equiv \langle b_i| \rho^B |b_i\rangle = \mathrm{Tr}_{A,B}\{\Pi_i^B \rho^{AB}\} \tag{4.10}$$

Using this conditional state, Eq. (4.9), we may extract the entropy $S(\rho_{A|\Pi_i^B})$ which gives us the uncertainty about the sub-system A that remains having projected B onto the state $|b_i\rangle$. We may then obtain the conditional entropy given a complete set of measurements on B, $\{\Pi_i^B\}$,

$$S(A|\{\Pi_i^B\}) \equiv \sum_i p_i^B S(\rho_{A|\Pi_i^B}) \tag{4.11}$$

From this the generalisation of $J(A:B)$, Eq. (4.2), can be constructed,

$$\mathcal{J}_{\{\Pi_i^B\}}(\rho^{AB}) \equiv S(\rho^A) - S(A|\{\Pi_i^B\}) \tag{4.12}$$

This quantity has one undesirable trait however, it is dependent on the basis we pick for the measurement projectors. In order to get rid of this dependence we pick the *best* measurement basis (that is the one where we are able to reduce our ignorance

about subsystem A the most).

$$\mathcal{J}_B(\rho^{AB}) \equiv S(\rho^A) - \max_{\{\Pi_j^B\}} S(A|\{\Pi_j^B\}). \tag{4.13}$$

This quantity was termed the *classical correlation* [16], as it represents the amount our ignorance on A is reduced having made a full set of the most informative measurements on B. It represents the amount we can learn about A from B by projecting B onto some detection basis. Unlike in the classical case, this need not be equivalent to the quantum mutual entropy $\mathcal{I}(\rho^{AB})$, which represents the total correlation between the two subsystems. The discrepancy between the two describes the correlation between the two subsystems that is inaccessible to our measurements, what can be thought of as the quantum part of the correlations. It is this quantity that was termed the *quantum discord* [109].

$$\mathcal{D}_B(\rho^{AB}) \equiv \mathcal{I}(\rho^{AB}) - \mathcal{J}_B(\rho^{AB}). \tag{4.14}$$

4.2.1 Properties of Discord

Discord admits the following properties [32],

1. It is not, in general, symmetric i.e, $\mathcal{D}_B(\rho^{AB}) \neq \mathcal{D}_A(\rho^{AB})$. This is a product of the fact that performing the measurement on A and B is an entirely different operation.

2. Discord is positive valued $\mathcal{D}_A, \mathcal{D}_B \geq 0$, a consequence of $S(A|\{\Pi^B\}) \geq S(\rho^{AB}) - S(\rho^B)$ [111]. Physically this describes how optimal measurements may remove, at best, only the uncertainty about B from the total system.

3. Discord is bounded from above by the inequality $\mathcal{D}_B(\rho^{AB}), \mathcal{D}_A(\rho^{AB}) \leq \mathcal{I}(\rho^{AB})$. Which describes that two subsystems may not be more *quantum* correlated

than they are correlated.

4. It is invariant under local unitary transformation i.e. discord of the ρ^{AB} is the same as for $(U_A \otimes U_B)\rho^{AB}(U_A \otimes U_B)^\dagger$. The only difference being that the optimal set of measurement is also rotated $\{\Pi^B\} \rightarrow \{U_B \Pi^B U_B^\dagger\}$, but of course since we carefully ensured that discord was measurement independent this has no effect on $\mathcal{D}_B$.

Prior to the seminal papers on discord [109, 15, 16], the term *quantum correlations* was considered synonymous with entanglement [14]. Whilst entangled states are necessarily discorded, the converse is a not true. Separable states which are, by definition [14], unentangled may also exhibit discord. A generic non-entangled state can be defined by the following density matrix

$$\rho^{AB} = \sum_i p_i \rho_i^A \otimes \rho_i^B. \tag{4.15}$$

For a state to have zero B-discord it *must* [15] be possible to write the state in the form of Eq. (4.15), but with the additional constraint that $\{\rho_i^B\}$ is made up of a set of orthogonal projectors i.e $\rho_i^B = |i\rangle \langle i|^B$, where $\{|i\rangle^B\}$ are a set of orthogonal states (similar condition hold in order for the state to have zero A-discord). Another way to state this condition is to say that a state has zero B-discord only if each of $\{\rho_i^B\}$ are diagonalisable in the same basis (similarly for A). This makes the condition to have zero discord much tighter than the condition for zero entanglement. States with entirely zero discord ($\mathcal{D}_A, \mathcal{D}_B = 0$) may *always* be written in the form,

$$\rho^{AB} = \sum_i p_i \, |i\rangle \langle i|^A \otimes |i\rangle \langle i|^B \,, \tag{4.16}$$

where both $\{|i\rangle^A\}$ and $\{|i\rangle^B\}$ describe sets of orthogonal vectors on their respective sub-space. A density matrix of the form of Eq. (4.16) is sometimes referred to

as *classical-classical* density matrices [32] as they admit no quantum correlations what-so-ever. Since the specific case defined by Eq. (4.16) occupies a very small volume of the possible Hilbert space spanned by Eq. (4.15), we can conclude that almost all non-entangled states are discorded [112, 113], and therefore admit some quantum correlations.

4.3 Density Matrix with Quantum Correlations

To understand the meaning of discord we briefly consider an example density matrix to give us a better understanding of the distinction of *mutual entropy*, Eq. (4.8), and *classical correlation*, Eq. (4.13).

Consider a density matrix of the form,

$$\rho^{AB} = \frac{1}{2} |00\rangle \langle 00| + |1\theta\rangle \langle 1\theta| , \qquad 0 \leq \theta < \pi. \tag{4.17}$$

We use the notation such that the first element of, e.g, $|ab\rangle$ refer to a state on the A-subspace and the second refer to a state on the B-subspace. i.e $|ab\rangle \langle ab| \equiv |a\rangle \langle a|^A \otimes |b\rangle \langle b|^B$. $|0\rangle , |1\rangle$ refer to two orthogonal states and $|\theta\rangle = \cos\theta |0\rangle + \sin\theta |1\rangle$. The state described by (4.17) is therefore of the form of Eq. (4.15) i.e unentangled. Since the states on the A-system are orthogonal $\mathcal{D}_A = 0$, the B-discord, $\mathcal{D}_B$, however will depend on the value of θ. For $\theta = 0, \pi/2, \pi$ the density matrix described by Eq. (4.17) is of the form of Eq. (4.16) and therefore $\mathcal{D}_B = 0$, but otherwise the state cannot be written in this form and $\mathcal{D}_B > 0$.

In figure (4.1) we plot, $\mathcal{I}(\rho^{AB})$, $\mathcal{J}_B(\rho^{AB})$ and $\mathcal{D}_B(\rho^{AB})$ for the density matrix described by Eq. (4.17). The figure confirms what was stated earlier, discord drops to zero for $\theta = 0, \pi/2, \pi$, but we can also now see that these zeros have different origins.

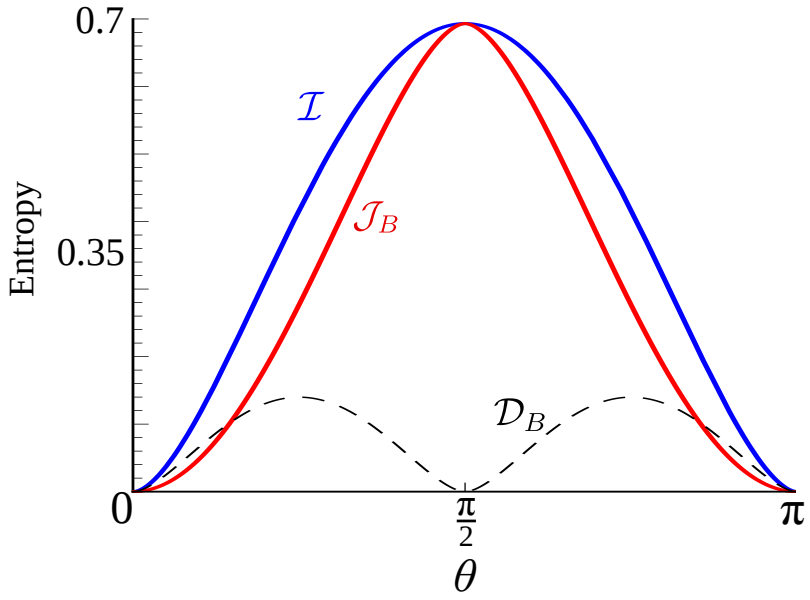

Figure 4.1: Mutual Entropy (blue), classical correlations (red), and quantum discord (black dashed) as a function of θ for the state described by Eq. (4.17). We perform the maximisation in the definition of $\mathcal{J}_B$ Eq. (4.2) numerically.

The zeros at $\theta = 0, \pi$ come from the fact the two sub-systems are completely uncorrelated ($\mathcal{I} = 0$) and therefore no quantum correlations can exist. Discord is again zero at $\theta = \pi/2$, but here the states are maximally correlated, the correlations are all classical however ($\mathcal{I} = \mathcal{J}_B$) and therefore $\mathcal{D}_B = 0$. For all other points $\mathcal{J}_B < \mathcal{I}$, meaning there exists correlations between the two subsystems which we are unable to measure. It is these correlations that are quantified by quantum discord.

4.4 Discord Witnesses

The quantum correlations manifest in discord have attracted a great deal of interest with it being suggested that it is discord (and not just entanglement) that is a necessary resource for a variety quantum information processes, including the speed up associated with quantum computation [18, 114] and the distribution of quantum information to many parties [115, 116]. This combined with the fact discord is rather

robust to decoherence in comparison to entanglement [19], has raised the stakes in experimentally fabricating a controllable discorded system. In spite of this, even a suggestion of a *witness* of discord has proved an illusive concept. As shown in Eq. 4.14, discord is defined in terms of conditional entropies. Direct evaluation therefore requires full tomographic characterisation of the density matrix, which is generally hard to implement and noisy [117]. The idea of a discord witness is to avoid directly evaluating the discord and just acts to identify its presence. They are inspired by entanglement witnesses such as Bell's inequality [118, 119], which are able, by measurement of specific correlation functions, to distinguish between a state which is entangled and one that is not. For example, we may propose a Hermitian operator $\hat{W}$ that satisfies $\mathrm{Tr}\{\hat{W}\rho_{sep}\} \geq 0$ where ρ_{sep} is a separable state but gives $\mathrm{Tr}\{\hat{W}\rho_{ent}\} < 0$, where ρ_{ent} is an entangled state. Measurement of such an operator would act as an entanglement witness. Discord witnesses prove less simple to define in this way. We may envision our discord witness, again given by a Hermitian observable $\hat{W}_D$. For a pure, separable state (and therefore non-discorded) ρ_i, we expect to create the operator so it has the property,

$$\mathrm{Tr}\{\hat{W}_D\rho_i\} \geq 0, \tag{4.18}$$

However we may sum two separable pure states together weighted by some valid probabilities and create a discorded state in which case we hope that our witness gives $\sum_i p_i \,\mathrm{Tr}\{\hat{W}_D\rho_i\} < 0$, which is obviously impossible from the statement given by Eq. (4.18) and that p_i are all positive [20]. This feature has meant that many discord witnesses suggested are only *sufficient* conditions for discord and fail as necessary conditions [20, 104, 120]. Those that succeed as necessary witnesses are complex and require the protocol to be performed on numerous replicas of the density matrix simultaneously [105]. In the next chapter, we propose a simple method to generate a

pair of qubits with a controllable degree of discord within a condensed matter setting. We then suggest a protocol that can be used to check for the existence of discord within these systems, we find that we can construct an experimentally accessible measure from these results. This measure appears to behave rather similarly to discord.

Chapter 5

Observing Discord

The work in this chapter is all original its purpose is twofold, firstly we demonstrate how a controllable discorded quantum state can be created in a solid state system. Specifically we generate a bipartite system out of a pair of two-level systems (qubits), which are realised by electronic Mach-Zehnders. Next we develop a protocol which is designed to test whether an unknown state in this system is discorded or not. We aim to highlight that our protocol is experimentally accessible within today's technology and that the measure we can extract from it is remarkably similar to discord. We illustrate the protocol with several examples. Once we have demonstrated the protocol for a single particle, zero temperature scenario, we introduce more realistic experimental conditions by considering the difference finite temperature makes, as well as many-body aspects.

5.1 State preparation

A pair of quantum point contacts (QPCs) correlated by a classical computer are well predisposed to create separable states such as those described by (4.15) with each ρ_i^A, ρ_i^B describing a qubit.

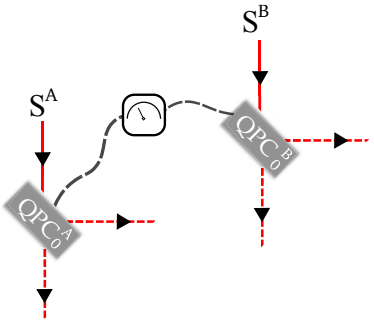

Figure 5.1: Initial Quantum Point Contacts (QPCs) on A and B are connected by a classical computer, this allows us to generate ρ^{AB} of the form of (4.15).

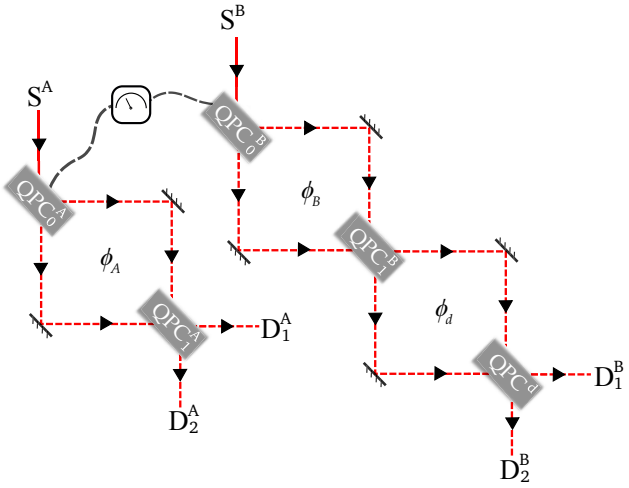

Figure 5.2: QPC_0^A and QPC_0^B shown in Fig. (5.1) form the entrance to MZI^A and MZI^B with Aharanov-Bohm fluxes ϕ_A and ϕ_B threading the loops respectively. Acting on the B-system there is an additional QPC (QPC^d) and Aharonov-Bohm Flux (ϕ_d) which form a *detecting* Mach-Zehnder, MZI^d.

We may create this generic bipartite separable state using two complimentary QPC's which we refer to as QPC_0^A and QPC_0^B (corresponding to A and B subsystems respectively) in Fig. (5.1), these act as beam-splitters. A state input into these QPC's may go into one of either the upper ($|\uparrow\rangle$) or lower ($|\downarrow\rangle$) arms. After the QPC's, the probability amplitudes in each arm are governed by the reflection and transmission probabilities at the QPC's and will in general be some superposition of $|\uparrow\rangle$ and $|\downarrow\rangle$. The QPCs are controlled by the attached classical computer. This computer simultaneously changes the reflection/transmission amplitudes at both point contacts with some pre-programmed probability. It therefore determines the density matrix which emerges from the initial QPC's (QPC_0^A and QPC_0^B) and assigns the probability of being in each state, this corresponds to the p_i's of equation (4.15). It is only through this entirely classical computer, and the probabilities it assigns,

that the subsystems of A and B may be correlated, this ensures that the state is indeed separable and may be represented as in equation (4.15). One can therefore, by changing the scattering matrices of the QPCs, produce states with a controllable amount of discord.

The other QPC's shown in the full set-up (Fig. (5.2)) will be used to determine whether the constructed state is B-discorded or not. Notice that we have chosen the set-up as asymmetric to just focus on observing B-discord; we could extend the A-subspace to include a detecting MZI if we also wished to observe A-discord, but for simplicity we only focus on one subspace. We determine if the state is B-discorded by using QPC_1^B to try to diagonalise all ρ_i^B's with the same scattering matrix; this is only possible if the state is not B-discorded (see discussion after Eq. (4.15)). Using this property we will see that the dependence on ϕ_d in a cross-correlator describing joint detection drains on A and B (e.g D_1^A and D_1^B respectively) can tell us whether the state is discorded or not. Such a dependence is amenable to measurement and our protocol therefore provides a witness for discord which is accessible within existing technologies.

5.2 State Propagation

A density matrix which describes our state *after* the initial QPC_0^A and QPC_0^B is described by ρ^{AB}. Propagation towards the drains is then represented via the transfer matrix $\mathcal{S}$, this describes the cumulative effects of phase gains from the Aharonov-Bohm effect as well as the scattering matrices at the QPCs. Its full description is given by,

$$\mathsf{S} \equiv \mathsf{S}^A \otimes \mathsf{S}^d \mathsf{S}^B. \tag{5.1}$$

These S-matrices are the products of the scattering at the QPCs and the phase difference accumulated along the different MZI arms, e.g. $\mathsf{S}^B = \mathcal{S}^B\mathcal{S}^B_\phi$, where

$$\mathcal{S}^B = \begin{pmatrix} r_B & t_B \\ -t_B^* & r_B \end{pmatrix}, \qquad \mathcal{S}^B_\phi = \begin{pmatrix} e^{i\phi_B} & 0 \\ 0 & 1 \end{pmatrix}. \tag{5.2}$$

Similar expression hold for S^A and S^d. We will find it useful to further parametrise the coefficients of the $\mathrm{QPC}_1^{A,B}$ scattering matrices as follows, $r_A = \cos(\alpha), t_A = e^{i\varphi_A}\sin(\alpha)$ and $r_B = \cos(\beta), t_B = e^{i\varphi_B}\sin(\beta)$.

5.3 Visibility

Information on how A and B is correlated is easiest analysed via a cross correlator. We look at the cross correlator describing joint detection at a detector on the A-subspace (D_1^A or D_2^A) and one on the B-subspace (D_1^B or D_2^B). We arbitrarily choose D_1^A and D_1^B and represent the measurement projectors at this point via the operators $\hat{N}^A$ and $\hat{N}^B$ respectively,

$$\langle \hat{N}^A\hat{N}^B\rangle = \mathrm{Tr}\{\hat{N}^A\hat{N}^B\mathsf{S}\rho^{AB}\mathsf{S}^\dagger\}. \tag{5.3}$$

The probability of an A-electron (electron in MZI^A) in state ρ_ν^A emerging at D_1^A is given by,

$$N_\nu^A = \mathrm{Tr}_A\{\hat{N}^A\mathsf{S}^A\rho_\nu^A(\mathsf{S}^A)^\dagger\}, \tag{5.4}$$

Defining the density matrix conditioned on detection at A as $\rho^{B|A} \equiv \sum_\nu p_\nu N_\nu^A\rho_\nu^B$ or, equivalently $\rho^{B|A} \equiv \mathrm{Tr}_A\{\hat{N}^A\mathsf{S}^A\rho^{AB}(\mathsf{S}^A)^\dagger\}$, allows us to represent Eq. (5.3) as

follows,

$$\langle \hat{N}^A \hat{N}^B \rangle = \mathrm{Tr}_B\{\hat{N}^B \mathsf{S}^d \mathsf{S}^B \rho^{B|A} (\mathsf{S}^B)^\dagger (\mathsf{S}^d)^\dagger\}. \tag{5.5}$$

Due to interference between $|\uparrow\rangle$ and $|\downarrow\rangle$ states in MZI^d, the value of $\langle \hat{N}^A \hat{N}^B \rangle$ will, in general, depend on ϕ_d. If the electron is not in a superposition of the arms in MZI^d, this dependence disappears. There is therefore no ϕ_d-dependence for the choice of S^B, $\mathsf{S}^B = \mathsf{S}_0^B$, which diagonalises the Hermitian matrix $\rho^{B|A}$ in the up/down basis i.e. $\tilde{\rho}_0^{B|A} \equiv \mathsf{S}_0^B \rho^{B|A} (\mathsf{S}_0^B)^\dagger$ is a diagonal matrix and therefore, $\mathcal{S}_\phi^d \tilde{\rho}_0^{B|A} (\mathcal{S}_\phi^d)^\dagger = \tilde{\rho}_0^{B|A}$ must be ϕ_d-independent. It is obvious from the definition of $\rho^{B|A}$ that if all ρ_ν^Bs are simultaneously diagonalisable (i.e ρ^{AB} is not B-discorded) then S_0^B is independent of the values $\{N_i^A\}$ and therefore independent of α and ϕ_A. We will prove later (Section 5.4) that it is also the case that if S_0^B does depend on one of these parameters of the A-subspace, the state is B-discorded. To check whether the state is B-discorded we may therefore extract the parameters describing S_0^B and see if they are dependent on the parameters from the A-subspace.

One can identify S_0^B by finding where the visibility defined by,

$$\mathcal{V}[\phi_d] = \frac{\max_{\phi_d}[\langle \hat{N}^A \hat{N}^B \rangle] - \min_{\phi_d}[\langle \hat{N}^A \hat{N}^B \rangle]}{\max_{\phi_d}[\langle \hat{N}^A \hat{N}^B \rangle] + \min_{\phi_d}[\langle \hat{N}^A \hat{N}^B \rangle]}, \tag{5.6}$$

vanishes. We may obtain an expression for where $\mathcal{V}[\phi_d] = 0$ by explicitly defining the terms in Eq. (4.15). We define $\rho_\nu^B \equiv |B_\nu\rangle \langle B_\nu|$, $\rho_\nu^A \equiv |A_\nu\rangle \langle A_\nu|$ and then use the general expressions

$$|A_\nu\rangle \equiv \cos\theta_{A_\nu} |\uparrow\rangle_A + e^{i\Phi_{A_\nu}} \sin\theta_{A_\nu} |\downarrow\rangle_A , \tag{5.7}$$

$$|B_\nu\rangle \equiv \cos\theta_{B_\nu} |\uparrow\rangle_B + e^{i\Phi_{B_\nu}} \sin\theta_{B_\nu}) |\downarrow\rangle_B . \tag{5.8}$$

The conditional density matrix after QPC_1^B is given by $\tilde{\rho}^{B|A} \equiv \mathsf{S}^B \rho^{AB} (\mathsf{S}^B)^\dagger$, or equivalently in terms of the parameters which describe the S-matrices,

$$\tilde{\rho}^{B|A} \equiv \begin{pmatrix} X(\alpha,\beta,\phi_A,\phi_B) & Y(\alpha,\beta,\phi_A,\phi_B) \\ Y^*(\alpha,\beta,\phi_A,\phi_B) & Z(\alpha,\beta,\phi_A,\phi_B) \end{pmatrix}, \tag{5.9}$$

$$\equiv \sum_\nu p_\nu N_\nu^A(\alpha,\phi_A) \begin{pmatrix} x_\nu(\beta,\phi_B) & y_\nu(\beta,\phi_B) \\ y_\nu^*(\beta,\phi_B) & 1-x_\nu(\beta,\phi_B) \end{pmatrix}, \tag{5.10}$$

where we have noted the explicit dependencies of the elements of this matrix on the parameters of $\mathsf{S}^B(\beta,\phi_B)$ and $\mathsf{S}^A(\alpha,\phi_A)$. These functions in terms of the states given in Eq. (5.7,5.8) are then given by,

$$\begin{aligned} N_\nu^A &= |\cos(\theta_{A_\nu})\cos(\alpha)e^{i(\phi_A+\Phi_{A_\nu})} + \sin(\theta_{A_\nu})\sin(\alpha)|^2, \\ x_\nu &= |\cos(\theta_{B_\nu})\cos(\beta)e^{i(\phi_B+\Phi_{B_\nu})} + \sin(\theta_{B_\nu})\sin(\beta)|^2, \\ y_\nu &= \frac{1}{2}\big[\cos 2\beta \sin 2\theta_{B_\nu}\cos(\Phi_{B_\nu}+\phi_B) - \sin 2\beta \cos 2\theta_{B_\nu} \\ &\quad + i\sin 2\theta_{B_\nu}\sin(\Phi_{B_\nu}+\phi_B)\big], \end{aligned} \tag{5.11}$$

then the parameters described in Eq. (5.9) are given by $X \equiv \sum_\nu p_\nu N_\nu x_\nu$, $Y \equiv \sum_\nu p_\nu N_\nu y_\nu$, and $Z \equiv \sum_\nu p_\nu N_\nu (1-x_\nu)$. Where we've made shifts such that $\phi_{A,B} \to \phi_{A,B} + \varphi_{A,B}$. From this one can deduce,

$$\langle \hat{N}^A \hat{N}^B \rangle = |r_d|^2 X + |t_d|^2 Z + 2|t_d r_d| \mathrm{Re}\{Y e^{i\phi_d}\}, \tag{5.12}$$

where we've also made a final simple shift, $\phi_d \to \phi_d + \varphi_d$. In agreement with that which was stated earlier $\langle \hat{N}^A \hat{N}^B \rangle$ is independent of ϕ_d *only if* $Y = 0$, i.e if $\tilde{\rho}^{B|A}$ is diagonal. To obtain the visibility, we find the stationary points with respect to ϕ_d,

as $\phi_d = \frac{1}{2}\ln\left(\frac{Y}{Y^*}\right), \frac{1}{2}\left[\ln\left(\frac{Y}{Y^*}\right) + 2\pi\right]$. This gives the visibility as shown below:

$$\mathcal{V}[\phi_d] = \frac{4|r_d t_d||Y|}{2|r_d|^2 X + 2|t_d|^2 Z}, \tag{5.13}$$

$$= \frac{2|Y|}{X+Z}, \qquad \text{if } |r_d|^2 = |t_d|^2 = 1/2, \tag{5.14}$$

where $X + Z = \sum_\nu p_\nu N_\nu^A$, i.e the visibility is proportional to the magnitude of the off-diagonal elements of the matrix (5.9). QPC^d is required only to allow interference to occur in MZI^d, we therefore fix it as a $50:50$ beamsplitter in Eq. (5.14) and from now on. S^B can be chosen so that $|Y| = 0$ for any ρ^{AB} (i.e any Hermitian matrix can be diagonalised) but we find that this can only be done independent of N_ν^A if $\mathcal{D}_B(\rho^{AB}) = 0$. In the following section we will first prove this statement. Then in Section 5.5 we will make use of this feature to propose a protocol which acts as a signature of discord and allows extraction of a quantifier which appears to match discord remarkably well.

5.4 Lines of Zero Visibility as a Witness of Discord

In this section we show the zero visibility condition of $\mathcal{V}[\phi_d]$ (which equate to $Y = 0$, see Eq. (5.14)) is independent of choice of measurement on A if, and only if, the initial density matrix ρ^{AB} is non B-discorded. Dependence on A enters the equation $|Y| = |\sum_\nu p_\nu N_\nu^A y_\nu| = 0$ via the coefficients N_ν^A. The dependence vanishes in two cases, the first describes where all $N_\nu^A = N^A$ i.e they are all equivalent. In this case a solution to $N^A|\sum p_\nu y_\nu| = 0$ can be found which is independent of N^A. This describes the trivial case where all ρ_ν^A are equivalent, in which case ρ^{AB} is uncorrelated between different subsystems and the state has zero discord.

The second case is where all y_ν are the same up to a sign, $|y_\nu| = y$, in which

case the condition $|Y| = 0$ factorises into,

$$(\pm p_1 N_1^A \pm p_2 N_2^A \pm ... \pm p_n N_n^A) y = 0, \tag{5.15}$$

which is satisfied for any choice of measurement on A only if $y = 0$. Therefore both real and imaginary parts of y, or equivalently y_ν, Eq. (5.11), must vanish for each ρ_ν^B. This gives the following equations that must be satisfied simultaneously for all ν,

$$\sin(2\theta_{B_\nu}) \sin(\Phi_{B_\nu} + \phi_B) = 0, \tag{5.16}$$

$$\cos(2\beta) \sin(2\theta_{B_\nu}) \cos(\Phi_{B_\nu} + \phi_B) - \sin(2\beta) \cos(2\theta_{B_\nu}) = 0. \tag{5.17}$$

One solution to the first of these equations is $\sin(\Phi_{B_\nu} + \phi_B) = 0$, which determines the ϕ_B-tuning required for finding a zero-visibility line of a given in-state, given by $\phi_B = n\pi - \Phi_{B_\nu}$ where n is an integer. With this solution to the first equation we then require, in order to satisfy the second, that $\tan(2\theta_{B_\nu}) = \pm \tan(2\beta)$. Recalling that $y_\nu = y$ for all ν if the solution is independent of measurement on A we obtain the condition,

$$\tan(2\theta_{B_\nu}) = \pm \tan\big(2\theta_{B_\mu}\big), \qquad \text{for all } \nu, \mu \tag{5.18}$$

Therefore (for all ν, μ) $\theta_{B_\nu} \pm \theta_{B_\mu} = n\pi/2$, where n is an integer. In the case when any of the set of $\{\theta_{B_\nu}\} = 0$, all $\theta_{B_\mu} = n\pi/2$ and Eq. (5.16) is automatically satisfied. If this is the case all ρ_ν^B and ρ_μ^B correspond to orthogonal states ($\theta_{B_\mu} = \pi/2$) or equivalent states ($\theta_{B_\mu} = 0, \pi$) in both cases the ρ^{AB} is non B-discorded independent of the set of $\{\rho_\nu^A\}$. If this is not the case then we obtain conditions such that $\Phi_{B_\nu} - \Phi_{B_\mu} = m\pi$ for all μ, ν this paired with $\theta_{B_\nu} \pm \theta_{B_\mu} = n\pi/2$ once again gives the conditions that ρ_ν and ρ_μ correspond to orthogonal states (if m/n are even/odd or

odd/even) or equivalent (if m/n are even/even or odd/odd).

The above tells us that the zeros of the visibility can *only* be made A-subspace independent if the states described by ρ_ν^B's are either orthogonal or equivalent ($\mathcal{I}(\rho^{AB}) = \mathcal{J}_B(\rho^{AB})$) OR the states described by ρ_ν^A's are equivalent ($\mathcal{I}(\rho^{AB}), \mathcal{J}_B(\rho^{AB}) = 0$); in both cases $\mathcal{D}_B(\rho^{AB}) = 0$. If the zeros of visibility are dependent on the A-subspace, the state is therefore discorded. In the following we will devise a experimentally viable protocol which makes use of this necessary and sufficient condition in order to detect when discord is present, and furthermore devise a experimentally accessible measure which is quantitatively similar to discord.

5.5 Protocol to Witness Discord

Eq. (5.14) together with Eq. (5.11) provides an explicit expression for the visibility with respect to ϕ_d. From this we may identify where the visibility (Eq. 5.14) goes to zero and therefore obtain the values of $(\beta, \phi^B) = (\beta_0, \phi_0^B)$ which diagonalise $\rho^{B|A}$ in terms of the input states denoted by Eqs. (5.7, 5.8),

$$\begin{aligned} \tan(2\beta_0) &\equiv \frac{\sum_\nu p_\nu N_\nu^A \sin(2\theta_{B_\nu}) \cos(\Phi_{B_\nu} + \phi_{B_0})}{\sum_\nu p_\nu N_\nu^A \cos(2\theta_{B_\nu})}, \\ \tan(\phi_{B_0}) &\equiv -\frac{\sum_\nu p_\nu N_\nu^A \sin(2\theta_{B_\nu}) \sin(\Phi_{B_\nu})}{\sum_\nu p_\nu N_\nu^A \sin(2\theta_{B_\nu}) \cos(\Phi_{B_\nu})}. \end{aligned} \tag{5.19}$$

To obtain zero visibility both the equations $\beta = \beta_0$ and $\phi_B = \phi_{B_0}$ *must* be met i.e Eq. (5.19) must both be satisfied simultaneously. If dependence on α (which is hidden in $N_\nu^A \equiv N_\nu^A(\alpha)$) disappears than the original density matrix was not B-discorded. Note that here we have taken to assuming ϕ_A, the Aharonov Bohm flux in MZI^A is fixed, as we only need to vary one parameter on A, without loss of generality we take $\phi_A = 0$ from now on. Our mission is therefore to check whether

the equations (5.19) are independent of α for an unknown state. We accomplish this as follows,

1. We first ensure we satisfy either $\phi_B = \phi_{B_0}(\alpha)$ or $\beta = \beta_0(\alpha)$ for some arbitrary (but fixed) α.

2. Once one of $\{\beta, \phi_B\}$ is fixed to $\{\beta_0, \phi_{B_0}\}$, we plot the other as a function of a now unconstrained α, from this plot it will be obvious whether $\{\beta_0, \phi_{B_0}\}$ is α dependent, and therefore trivial to identify whether the state is B-discorded or not.

We now proceed to illustrate how one could perform the above steps experimentally with some representative examples.

5.6 Examples of the Protocol

As an initial example we will, for simplicity, pick real in-states ($\Phi_{A_\nu}, \Phi_{B_\nu} = 0$ in Eq. (5.7,5.8) for all ν) and utilise the notation $|\theta_{A_\nu}\theta_{B_\nu}\rangle \equiv |A_\nu\rangle \otimes |B_\nu\rangle \Big|_{\Phi_{A_\nu},\Phi_{B_\nu}=0}$ and then perform our protocol on the state,

$$\rho^{AB} = 1/2\,|{+}{+}\rangle\langle{+}{+}| + 1/2\,|\theta\theta\rangle\langle\theta\theta|\,, \tag{5.20}$$

for two different choices of θ . Here the notation $|\pm\rangle \equiv \frac{1}{\sqrt{2}}(|\uparrow\rangle \pm |\downarrow\rangle)$. $|+\rangle\,, |-\rangle$ may also be expressed in θ-representation as $|\theta = \pi/4\rangle\,, |\theta = 3\pi/4\rangle$ respectively. The state given by Eq. (5.20) is *not* discorded for $\theta = \pi/4, 3\pi/4$ (as for this case $\langle B_1|B_2\rangle = 1$ and $\langle B_1|B_2\rangle = 0$ respectively i.e they are equivalent or orthogonal) and discorded for all other values of θ.

According to our scheme we must now extract the value of either β_0 or ϕ_{B_0} for a fixed α. We do so by arbitrarily choosing the value of $\alpha = \pi/3$ and then plotting

the visibility as a function of β and ϕ_B, this is shown in Fig. (5.3) using Eq. (5.19) for $\theta = 3\pi/4$ and $\theta = 0$.

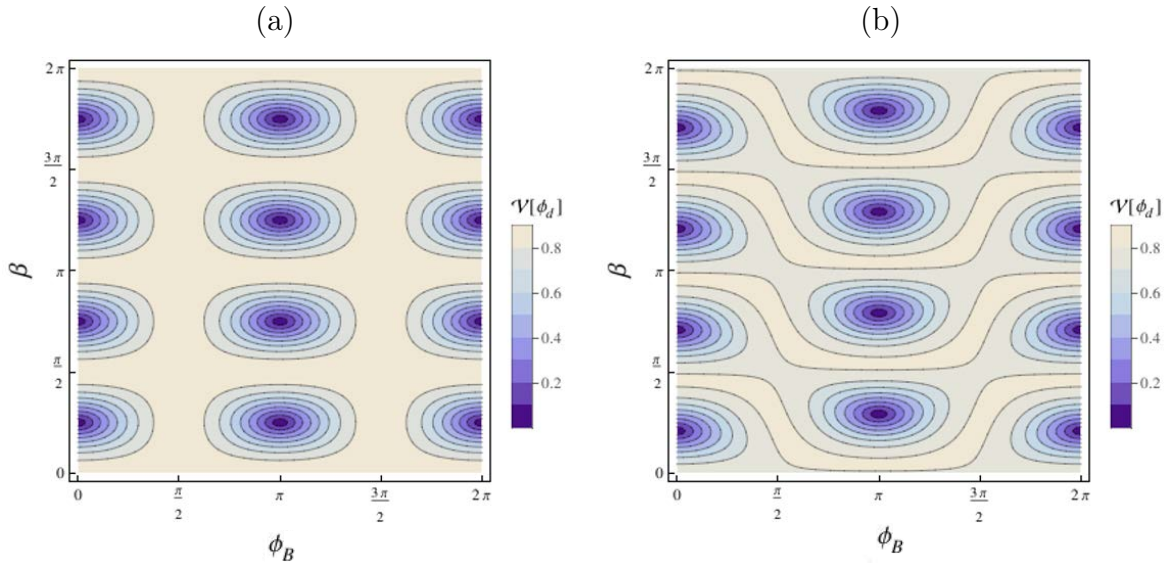

Figure 5.3: The visibility landscape for two in-states as a function of parameters β and ϕ_B controlling, respectively, the transparency of QPC_1^B and the phase difference in MZI^B. Here we keep fixed the values of corresponding parameters in MZI^A ($\alpha = \pi/3$ and $\phi_A = 0$). In this example we choose symmetric in-states with the transparencies of QPC_0^A and QPC_0^B simultaneously switching between the same values in order to give density matrices of the form Eq. (5.20), defined by the density matrices (a) $\rho^{AB} = \frac{1}{2}|{+}{+}\rangle\langle{+}{+}| + \frac{1}{2}|{-}{-}\rangle\langle{-}{-}|$, $\theta = 3\pi/4$ in Eq. (5.20 and (b) $\rho^{AB} = \frac{1}{2}|{\uparrow}{\uparrow}\rangle\langle{\uparrow}{\uparrow}| + \frac{1}{2}|{+}{+}\rangle\langle{+}{+}|$, $\theta = 0$ in Eq. (5.20. Since the states $|+\rangle$ and $|-\rangle$ are orthogonal whereas $|+\rangle$ and $|\uparrow\rangle$ are not, these density matrices describe a non-discorded state (a) and a discorded state (b).

The value of (β_0, ϕ_{B_0}) are given by the coordinates where the visibility drops to zero, we only need one of the components, we pick ϕ_{B_0} and observe this to be $\phi_{B_0} = 0, \pi$ for both choices of θ. Actually this would be the correct choice for any state within family of real states we have chosen as our examples (given by Eq. (5.20)). Since with the condition $\{\Phi_{B_\nu}\} = 0$, Eqs. (5.19) reduce to the simpler conditions given

by,

$$\tan(2\beta_0) = \pm\frac{\sum_\nu p_\nu N_\nu^A \sin(2\theta_{B_\nu})}{\sum_\nu p_\nu N_\nu^A \cos(2\theta_{B_\nu})}, \qquad \phi_{B_0} = 0, \pi. \tag{5.21}$$

where $+, -$ solutions correspond to when $\phi_{B_0} = 0, \pi$ respectively. With this being the case, if we limit ourselves to states which fall within the family of states where $\{\Phi_{B_\nu}\} = 0$, then step one of our scheme can be skipped and we can proceed with step two by choosing $\phi_B = 0, \pi$. Similarly if we choose $\{\Phi_{B_\nu}\} = \Phi_B$ then $\phi_{B_0} = \Phi_B, \Phi_B + \pi$. The protocol of course still works if we do not take the set of Φ_{B_ν} to be the same for all ν and we give example of this in Section 5.7.2. $\{\Phi_{A_\nu}\}$ prove to be almost entirely irrelevant as we are concerned only with B-discord.

As of yet we can, from Fig. (5.3), still make no statements about discord. We therefore proceed with step 2 of the protocol; we fix $\phi_B = 0$ (π would have been an equally appropriate choice for our chosen states) and plot the visibility as a function of α, β, cf. Fig. (5.4). This will allow us to extract the equation for β_0.

Figures (5.4a) and (5.4b) clearly display what we expect them to. In the case of zero discord state, Fig (5.4a), there are straight horizontal lines of zero visibility corresponding to $\beta_0 = \textit{constant}$ (note there are also vertical lines which we shall discuss in the Section 5.7.1) whilst in the discorded case, Fig (5.4b), the lines of zero visibility are clearly α-dependent. In the next section we attempt to quantify this dependence.

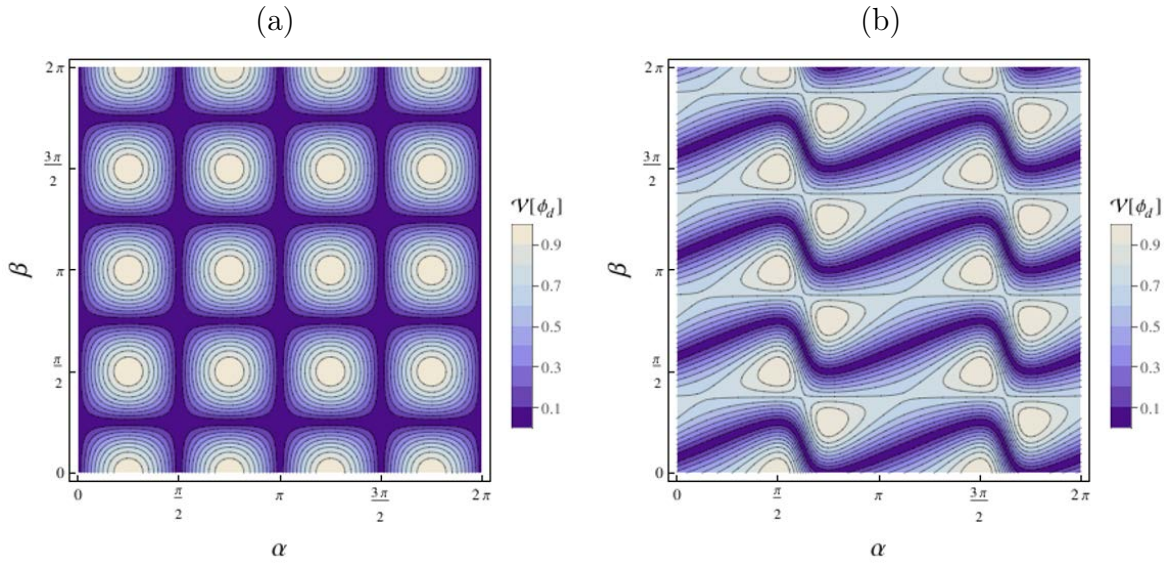

Figure 5.4: The visibility landscape for two in-states as a function of parameters β and α which control the transparencies of QPC_1^A and QPC_1^B respectively. The Aharonov-Bohm flux through MZI^B is left fixed at $\phi_B = \phi_{B_0} = 0$. We see a striking difference between (a) B-non-discorded density matrix, $\rho^{AB} = \frac{1}{2}|{+}{+}\rangle\langle{+}{+}| + \frac{1}{2}|{-}{-}\rangle\langle{-}{-}|$, and (b) the B-discorded state, $\rho^{AB} = \frac{1}{2}|{\uparrow}{\uparrow}\rangle\langle{\uparrow}{\uparrow}| + \frac{1}{2}|{+}{+}\rangle\langle{+}{+}|$. The zero visibility (dark) lines are independent of the state of subsystem A in (a) and show a strong characteristic dependence in (b). The pattern is periodic in β, with period $\pi/2$, and in α, with period π.

5.6.1 Quantifying Discord

The most obvious measure for quantifying the 'waviness' of the zero visibility lines we can see in Fig. (5.4b) is to pick one of the these curves and take the standard deviation from the mean, which will clearly be zero for a straight line and non-zero otherwise. However the $\pi/2$ periodicity of β causes issues here, as a demonstration of why this is the case, consider the visibility graphs given in Fig. (5.5).

The states for which we plot the visibility of in Fig. (5.5) have similar discord, cf. Fig. (5.6), yet appear completely different. One can see that if we were to take the standard deviation of one of the curves this measure would be much larger for Fig. (5.5b) then for Fig. (5.5a), we have not taken into account that Fig. (5.5b) is close

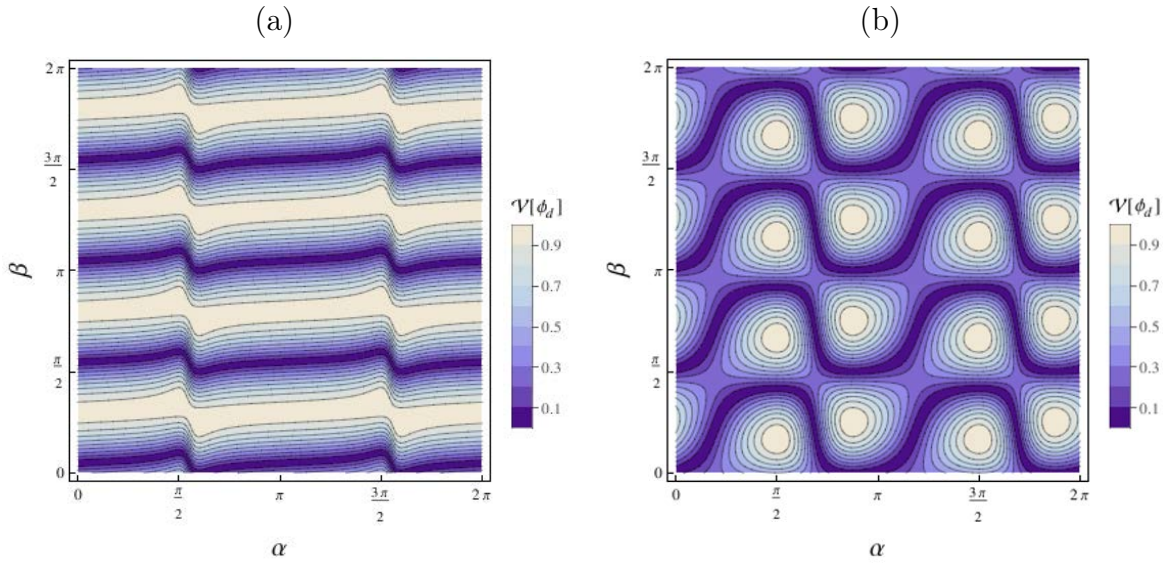

Figure 5.5: The visibility plots for $\rho^{AB} = 1/2\,|\uparrow\uparrow\rangle\,|\uparrow\uparrow\rangle + 1/2\,|\theta\theta\rangle\,\langle\theta\theta|$ (with $\phi_B = 0$) where in (a) $\theta = \pi/10$ and in (b) $\theta = 5\pi/12$. These two density matrices have similar discord, as can be seen from Fig. 5.6, yet their visibility landscapes look completely different.

to turning into the grid-like graph similar to Fig. (5.4b). Thus we wish to construct a measure which takes into account this periodicity. Since the period is given by $\pi/2$, we try the measure $f_\beta(\alpha) = \cos^2(2\beta_0)$,

$$\cos(2\beta_0) = \pm\left\{1 + \left(\frac{\sum_{\nu=1}^{n} p_\nu^{(A)} \sin(2\theta_\nu)\cos(\Phi_\nu + \phi_{B0})}{\sum_{\mu=1}^{n} p_\nu^{(A)} \cos(2\theta_\mu)}\right)^2\right\}^{-1/2},$$
$$\equiv (f(\alpha))^{1/2}. \tag{5.22}$$

The function $f_\beta(\alpha) = \cos^2(2\beta_0(\alpha))$ therefore contains all solutions for β_0 which differ by $\pi/2$, $f_\beta(\alpha)$ is again only α dependent if the state is discorded. We may therefore now consider the deviation of this quantity,

$$\Delta_\beta^2 = \int_0^{2\pi} \frac{d\alpha}{2\pi}\,\left[f_\beta(\alpha) - \overline{f}_\beta\,\right]^2, \qquad \overline{f}_\beta = \int_0^{2\pi} \frac{d\alpha}{2\pi}\,f_\beta(\alpha). \tag{5.23}$$

Such a measure is by no means unique, but it appears to work well when we contrast it to discord for the state, $\rho^{AB} = 1/2\,|\uparrow\uparrow\rangle\langle\uparrow\uparrow| + 1/2\,|\theta\theta\rangle\langle\theta\theta|$ in Fig. (5.6).

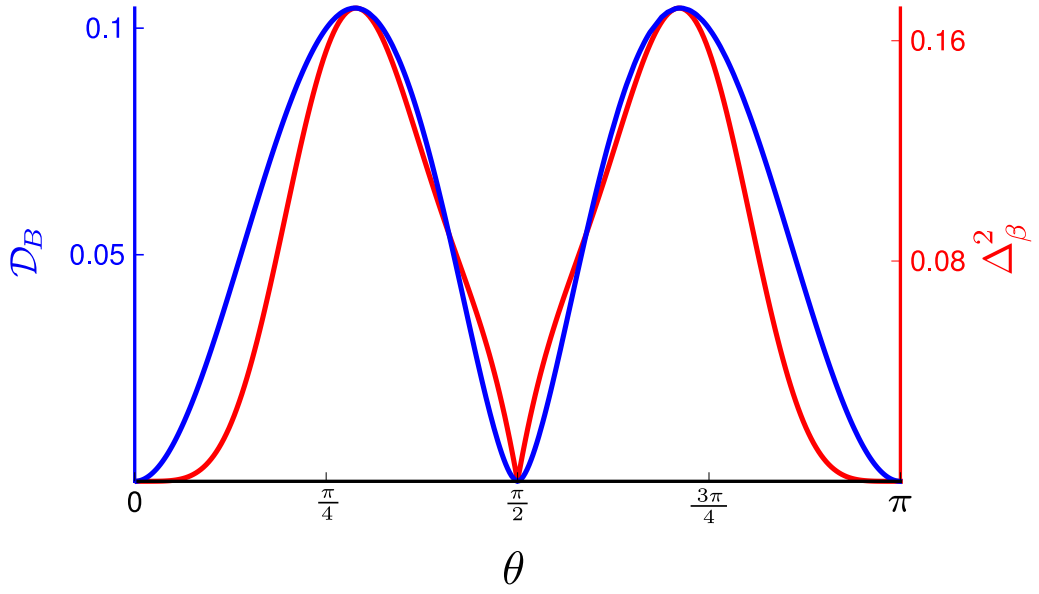

Figure 5.6: The standard definition of discord, $\mathcal{D}_B$, (blue) vs the alternative measure, Δ^2_β, (red) for the in-state with the density matrix $\rho^{AB} = \frac{1}{2}\,[\,|\uparrow\uparrow\rangle\langle\uparrow\uparrow| + |\theta\theta\rangle\langle\theta\theta|\,]$.

We may also check the measure for less symmetric states of the form,

$$\rho^{AB} = 1/2\big[\,|\uparrow\uparrow\rangle\langle\uparrow\uparrow| + |\theta_A\theta\rangle\langle\theta_A\theta|\,\big], \tag{5.24}$$

where now we chose, in general, that $\theta_A \neq \theta$. We compare this state for different θ_A $(= \pi/2, \pi/4, \pi/8)$ below in Fig. (5.7).

From Fig. (5.7) we see that, for discord, the peaks of the curves shift and the amplitude is diminished as $\theta_A \to 0$. The peaks of Δ^2_β also decrease as θ_A is reduced, though the position of the θ-dependent peaks of each function match $\mathcal{D}_B$ less well as θ_A decreases. This measure *always* matches the zeros of discord providing $\{\Phi_{B_\nu}\} = \Phi_B$ however, and thus never produces a false witness in this case.

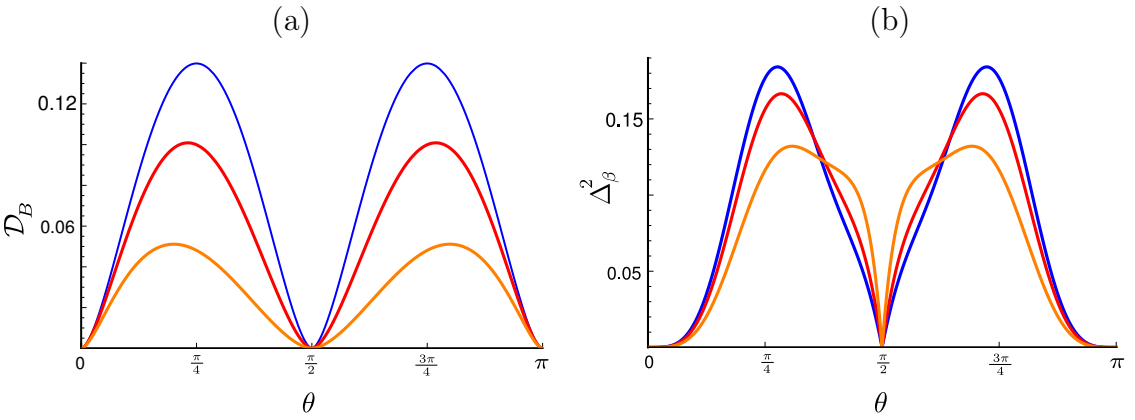

Figure 5.7: Discord (a) and our measure Δ^2_β (b) for state Eq. (5.24) with, $\theta^A = \pi/2$ (blue), $\theta^A = \pi/4$ (red), $\theta^A = \pi/8$ (orange).

For $\{\Phi^B_\nu\} \neq \Phi_B$ the measure $\Delta^2_\beta > 0$ can fail as a necessary condition for discord for some select choices. Therefore if we do not fix $\{\Phi^B_\nu\}$ to a non-zero Δ^2_β becomes only a sufficient condition for discord. This is a result of some select choices of discorded ρ^{AB} having a β_0 which is not α dependent, but a diagonalising phase, ϕ_{B_0}, which is α dependent. In such a situation we need to consider a similar function to $f(\alpha)$ but based on ϕ_{B_0} as opposed to β_0. We consider,

$$f_\phi(\alpha) \equiv \cos^2(\phi_{B_0}) = \left\{1 + \left(\sum_{\nu=1}^{n} \frac{\sin(2\theta_{B_\nu})\sin(\Phi_{B_\nu})}{\sin(2\theta_{B_\nu})\cos(\Phi_{B_\nu})}\right)^2\right\}^{-1} \tag{5.25}$$

We may then consider the standard deviation of this quantity Δ^2_ϕ (defined similarly to Eq. (5.23)) which, when it is > 0, also individually provides a sufficient condition for discord. Together with Δ^2_β, however, a necessary condition for discord is guaranteed by:

$$\Delta^2_\phi + \Delta^2_\beta > 0 \tag{5.26}$$

We give an example where Δ^2_β on it own fails as a witness later in Section 5.7.2. We hasten to add that whilst Δ_β may fail as a necessary condition for discord, the

protocol itself *never* fails, it is only this quantifier that may. In the next section, we clarify some interesting aspects of the visibility plots shown so far and give additional examples of the protocol enacted on more complicated states.

5.7 Additional Examples

5.7.1 Zero Discord: Grid or Barcode

We demonstrated that a lack of dependence on α of the lines of zero visibility (i.e the lines are straight as a function of α) means zero discord, but often in cases of zero discord we also see the emergence of vertical straight lines (zero's of visibility which are β independent). We find that the two scenarios of just horizontal lines (barcode), Fig (5.8b), or a grid-like scenario, Fig (5.8a) whilst both referring to zero discord states refer to two different routes of getting there. Horizontal lines mean the two subsystems are entirely uncorrelated, whilst grid-like (horizontal and vertical lines) means the two subsystems are correlated but only classically.

Grid-like

A gridded graph such as Fig. (5.8a) are produced when the state is *classically correlated*, that is when no information about the correlations between subsystems A and B is lost when one makes the correct measurement on subsystem-B.

A classically correlated (with respect to subsystem-B) state, means that the state described by ρ_1^B is orthogonal to the one described ρ_2^B. States of this form may always be reduced to a mixed state of the form $\sum_{\nu=1}^{2} p_\nu \rho_\nu^A \otimes \rho_\nu^B$, where ρ_ν^B are pure but ρ_ν^A are, in general, mixed and not equal ($\rho_1^A \neq \rho_2^A$). If $\rho_1^A = \rho_2^A$ the two subsystems are completed uncorrelated and we obtain the barcode images like Fig. (5.8b).

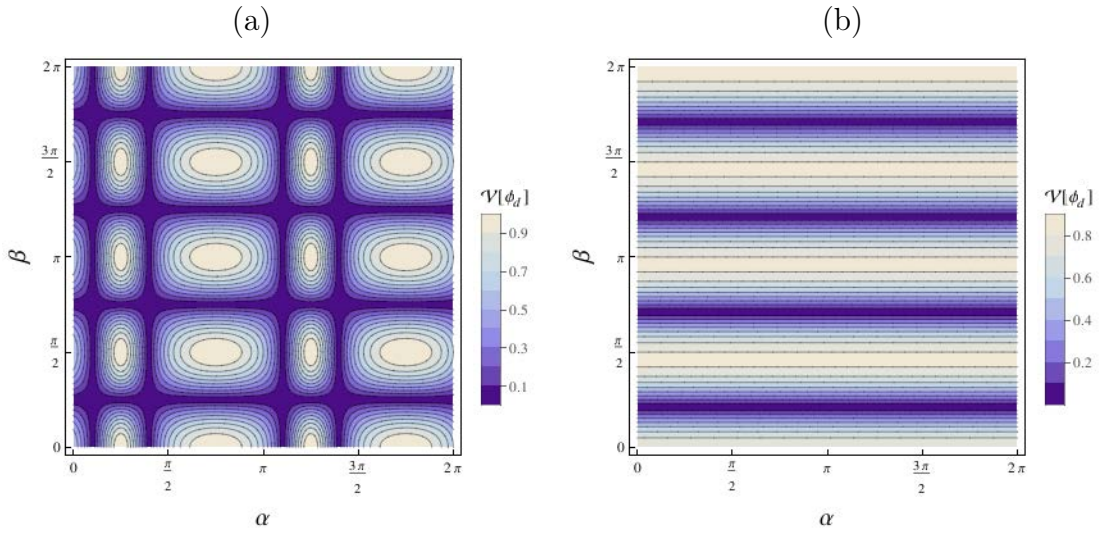

Figure 5.8: The visibility plots for (a) $\rho^{AB} = \frac{1}{5}|--\rangle\langle--| + \frac{4}{5}|++\rangle\langle++|$ and (b) $\rho^{AB} = \frac{1}{2}|00\rangle\langle00| + \frac{1}{2}|0+\rangle\langle0+|$, with $\phi_B = 0$. (a) displays the 'grid-like' visibility characteristic of a density matrix which is correlated between A and B subsystems, but undiscorded i.e the correlations are classical only. The barcode graph of (b) is a result of a density matrix which is completely uncorrelated between A and B subsystems.

In the case where the initial B states are orthogonal, and it is clear from the definition of $y_\nu(\beta, \phi_B)$ in Eq. (5.11) that $y_2(\beta, \phi_B) = -y_1(\beta, \phi_B)$. Visibility is proportional to $|Y|$ (see Eq. (5.14)), and in this case, it is therefore zero when,

$$|Y| = |y_1(\beta, \phi_B)(p_1 N_1^A(\alpha) - p_2 N_2^A(\alpha)| = 0, \tag{5.27}$$

One therefore has two possible routes to obtain zero visibility,

$$y_1(\beta, \phi_B) = 0, \qquad p_1 N_1^A(\alpha) = p_2 N_2^A(\alpha). \tag{5.28}$$

The first of these solutions is dependent only on the parameters of subsystem-B which give the horizontal lines of Fig (5.8a). The second solution is dependent only on parameters of subsystem-A which gives the vertical ones, producing the distinctive grid-like visibility plot.

Barcode-like

Lines like those shown in Fig. (5.8b) again fall into the zero B-discord category, but without the vertical lines that are necessary for classically correlated states. The 'barcode' style visibility graphs describe *uncorrelated* A and B subsystems.

For the states to be uncorrelated either $\rho_\nu^B = \rho_\mu^B$ or $\rho_\nu^A = \rho_\mu^A$ for all ν, μ, or equivalently we can write the density matrix as,

$$\rho^{AB} = \rho^A \otimes \rho^B, \tag{5.29}$$

where ρ^A and ρ^B are in general mixed states, $\rho^A = \sum_\nu p_\nu^A \rho_\nu^A$, $\rho^B = \sum_\nu p_\nu^B \rho_\nu^B$. States of the form show above lead to a visibility given by,

$$\begin{aligned} \mathcal{V}[\phi_1^b] &= \frac{|(\sum_\nu p_\nu^B y_\nu(\beta, \phi_B))(\sum_\mu p_\mu^A N_\mu^A(\alpha))|}{\sum_\iota p_\iota^A N_\iota^A(\alpha)}, \\ &= \Big|\sum_\nu p_\nu^B y_\nu(\beta, \phi_B)\Big|. \end{aligned}$$

Therefore zeros of visibility only emerge when $|\sum_\nu p_\nu^B y_\nu(\beta, \phi_B)| = 0$, which is only dependent on parameters of subsystem-B and therefore gives the characteristic barcode zero-visibility curves. Note that the sum over μ and ι in top and bottom cancel completely since both p_ν^A and N_ν^A must be real and positive.

5.7.2 States with different off-diagonal phase

Up until this point we only considered examples of our protocol for when density matrices ρ_ν^B have the same off-diagonal phase, but our protocol also works for states where the phase is different. Below we will give an example of what we would expect using our protocol for a state with off-diagonal phase on B, we will continue to assume there is no off-diagonal phase on A for the sake of simplicity. We consider

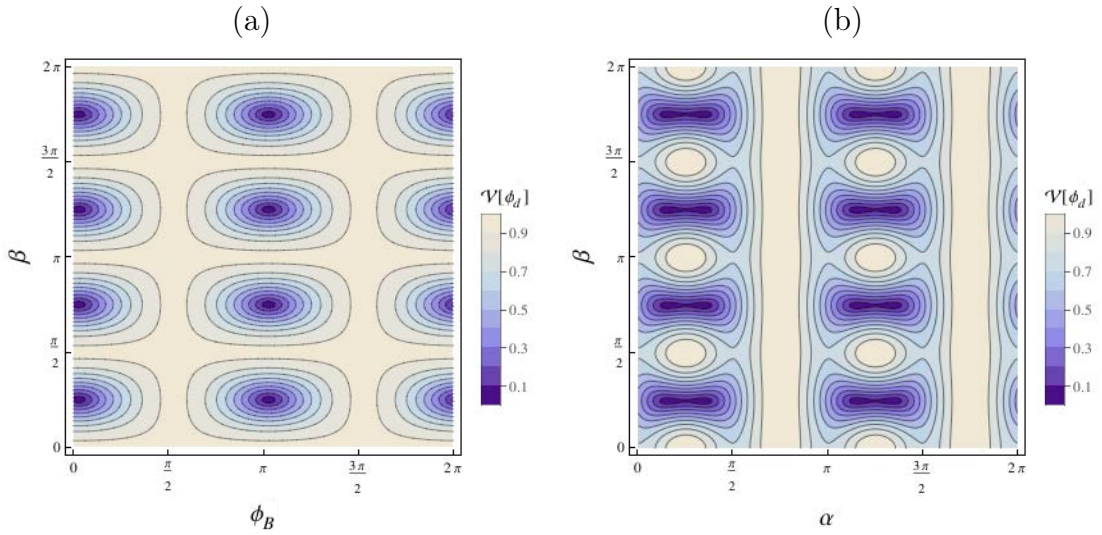

Figure 5.9: The visibility plots for the density matrix given by Eq. (5.30) with $\Phi_1 = 0$ and $\Phi_2 = \pi/2$, (a) Shows visibility as function of β, ϕ_B with $\alpha = \pi/3$, (b) gives visibility plot as function of β, α now fixing $\phi_B = \arctan\left(\frac{2-\sqrt{3}}{3}\right)$ (see Eq. (5.31).

the state,

$$\rho^{AB} = \frac{1}{2}\left|+;+,\Phi_1\right\rangle\left\langle+;+,\Phi_1\right| + \frac{1}{2}\left|-;-,\Phi_2\right\rangle\left\langle-;-,\Phi_2\right|, \tag{5.30}$$

where $|\theta_{A_\nu};\theta_{B_\nu},\Phi_{B_\nu}\rangle \equiv |\theta_{A_\nu}\rangle \otimes |\theta_{B_\nu},\Phi_{B_\nu}\rangle \equiv |A_\nu\rangle\big|_{\Phi_{A_\nu}=0} \otimes |B_\nu\rangle$ and the states $|A_\nu\rangle$ and $|B_\nu\rangle$ are given by Eq. (5.7) and (5.8) respectively. The above state has zero discord providing that $\Phi_1 = \Phi_2 + n\pi$ where n is an integer. We will arbitrarily pick $\Phi_1 = 0$ and $\Phi_2 = \pi/2$ so that the resulting state is discorded and then proceed to check this using our protocol. First we plot the visibility graph with fixed α (we choose $\alpha = \pi/3$) as function of β and ϕ_B, this is shown in Fig. (5.9a). These graphs appear similar to the ones shown earlier, but the values of ϕ_B where visibility drops to zero are now slightly shifted from zero and π. Their positions are given by,

$$\phi_{B_0} = \arctan\left(\frac{2-\sqrt{3}}{3}\right),\ \arctan\left(\frac{2-\sqrt{3}}{3}\right) + \pi. \tag{5.31}$$

Fixing ϕ_B to the first of these values we then plot the visibility as a function of β and α, this is given in (5.9b).

The difference between the state shown here and those given earlier is now apparent. It is even more stark here that the parameters β_0, ϕ_{B0} depend on α. This is due to the fact the value of ϕ_{B0} is now also α dependent (in previous examples where $\{\Phi_\nu\} = \Phi$ it was only β_0 which depended on α). This means that as α is changed we no longer have the correct value of ϕ_B which diagonalises the state, and since to diagonalise the state both $\beta = \beta_0$ and $\phi_B = \phi_{B0}$ must be true there are large regions of Fig. (5.9b) where the state can not be diagonalised and therefore visibility can not go to zero, a very clear demonstration that the state is discorded.

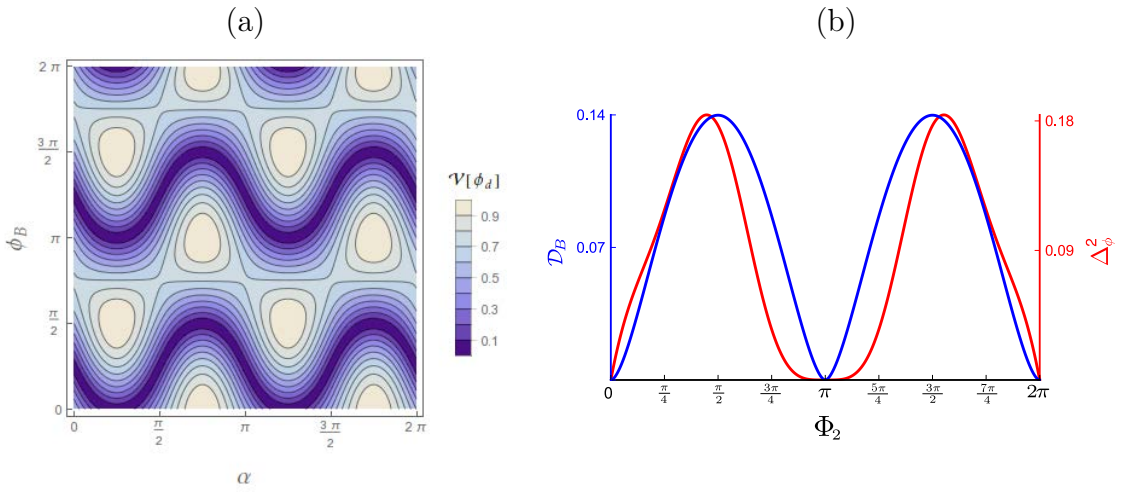

Figure 5.10: (a) Visibility plot for the density matrix given by Eq. (5.30 with $\Phi_1 = 0$ and $\Phi_2 = \pi/2$, plots are given as a function of ϕ_B and α with $\beta = \beta_0 = \pi/4$. (b) demonstrates discord and Δ^2_ϕ for the state described by Eq. (5.30 for a range of Φ_2 with $\Phi_1 = 0$.

This is an example of where if we take Δ^2_β alone we would not be able to tell the state were discorded (despite how obvious it is from Fig. (5.31), i.e our protocol succeeds as a necessary witness but since $\Delta^2_\beta = 0$, it fails as a quantifier). Δ^2_ϕ, however, may be extracted from a α, ϕ_B visibility plot (Fig. 5.10a) taking β to be

fixed at the diagonalising choice of $\beta_0 = \pi/4$ (where β_0 may be extracted from Fig. (5.9a)). Plotting Δ^2_ϕ we see it once again behaves similarly to discord as seen in Fig. (5.10b).

5.7.3 Example with three states

We have previously limited ourselves to examples with $n = 2$ in a separable density matrix described by Eq. (4.15), we briefly consider an example with $n = 3$,

$$\rho^{AB} = 1/3\,|\uparrow\uparrow\rangle\langle\uparrow\uparrow| + 1/3\,|\downarrow\downarrow\rangle\langle\downarrow\downarrow| + 1/3\,|\theta\theta\rangle\langle\theta\theta|\,. \tag{5.32}$$

Since the state is real we know that the correct choice of the diagonalising rotation is $\phi_{B_0} = 0$. Fixing ϕ_B to this value we can then plot the visibility as a function α and β. Fig (5.11a) gives a snapshot of one of these visibility graphs for $\theta = \pi/4$. We see the characteristic waviness which correctly tells us the state is discorded, Δ^2_β for this value of θ can be extracted from this graph. We plot Δ^2_β for different θ and contrast it to B-discord in Fig. (5.11b). We see that once again the most important features of discord are mirrored in Δ^2_β.

This concludes the examples of our protocol that we shall give. While it is entirely provable that our protocol demonstrates whether a state is discorded or not via the curviness (or in some cases discontinuity, see Fig. (5.9a)) of the zero visibility lines, we hope the additional examples have served to show that producing a measure which quantifies this curviness is well representative of the discord.

In the next (and final) section of this thesis we go on to show that the protocol is still valid under more realistic experimental conditions such as finite temperature and many (albeit non-interacting) bodies.

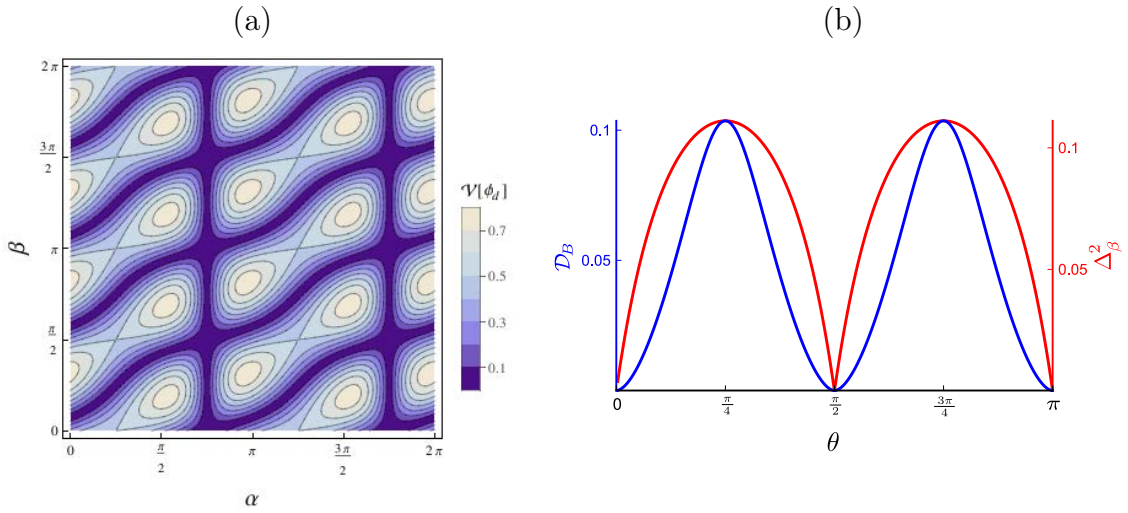

Figure 5.11: (a) Shows a visibility plot of density matrix given by Eq. (5.32) with $\theta = \pi/4$, the tell-tale signs of discord are present in the curviness of the zero-visibility lines. (b) plots the discord of Eq. (5.32) for different θ and contrasts it to the measure of curviness which can be extracted from graphs like that shown in (a).

5.8 Finite Temperature and Many Body Discord

In our previous discussion of discord we considered a single particle description. This is a valid description of an electronic MZI with a very dilute stream of electrons with spread of energies which is small compared to the intrinsic energy scales of the Mach-Zehnder (see Section 1.2), i.e both the voltage biases on the sources and the temperature of the system are small. We might expect that as these restriction are relaxed our assumptions and therefore our description will start to fail. To investigate this we first focus on a situation where a single particle is injected into the system from a thermal bath and then see it is trivial to upgrade this to a finite temperature, many-body (non-interacting) case. We do not include dephasing to the environment here.

5.8.1 Single Particle, Finite Temperature Discord

The single electron entering at S_1^A and S_1^B is replaced by a voltage bias of eV_A and eV_B. This means that the initial state (before $\mathrm{QPC}_0^{A,B}$), and as of yet uncorrelated,

state of $\rho_0^{AB} = \rho_0^A \otimes \rho_0^B = |S_1^A\rangle\langle S_1^A| \otimes |S_1^B\rangle\langle S_1^B|$ where $|S_1^{A(B)}\rangle$ were pure are replaced by a statistical distribution of the states within the energy interval ϵ_F to $\epsilon_F + eV_C$ ($C = A, B$). We use the notation $a^\dagger_{C,\uparrow,k}$ to describe creating an electron before QPC_0^C. We may then represent the density matrix which describes the electron being emitted from a thermal bath on top of the vacuum contribution as $\rho_0^C = 1/(eV_cL_c)\sum_k \big[f(\hbar v_F k - eV_c) - f(\hbar v_F k)\big] a^\dagger_{C,\uparrow,k} a_{C,\uparrow,k}$, where the normalisation before the sum ensures there is only one particle. The vectors $a^\dagger_{C,\uparrow,k}|0\rangle$ form an orthogonal basis in k-space and this (purely classical) statistical mixture of states does not impact whether the state is discorded or not. $f_{\mu_i}(x) = f(x - \mu_i)$ is the finite temperature Fermi-Dirac distribution with a chemical potential μ_i. The A and B subsystems are then correlated by the initial pair $\mathrm{QPC}_0^{A,B}$ which are controlled by a classical computer (C.C.), the C.C. changes the scattering matrix which parametrises $\mathrm{QPC}_0^{A(B)}$ to $\mathcal{S}_{0_\nu}^{A(B)}$ simultaneously with probability p_ν.

$$\begin{aligned} \rho^{AB} &= \sum_\nu p_\nu \big(\mathcal{S}^A_{0_\nu}\rho_0^A(\mathcal{S}^A_{0_\nu})^\dagger\big) \otimes \big(\mathcal{S}^B_{0_\nu}\rho_0^B(\mathcal{S}^B_{0_\nu})^\dagger\big), \qquad \mathcal{S}^C_{0_\nu} = \begin{pmatrix} r_{C_0\nu} & t_{C_0\nu} \\ -t^*_{C_0\nu} & r_{C_0\nu} \end{pmatrix}, \\ &= \sum_\nu p_\nu \rho_\nu^A \otimes \rho_\nu^B. \end{aligned} \tag{5.33}$$

This is therefore a separable state of the exact form described by Eq. (4.15), but where each individual density matrix, $\rho_\nu^{A,B}$ is described by a mixed thermal state. Similar to in the last section, we can relate the creation/annihilation operators in each section of the MZI's to those in the previous ones by the scattering matrices. The annihilation operators in the final section (after QPC^d) of MZI^d can be related to the incoming states before QPC_0^B as follows,

$$\mathbf{d}_k = \mathsf{S}_k^d \mathsf{S}_k^B \mathcal{S}^B_{0,\nu} \mathbf{a}_{B,k}, \qquad \mathbf{a}_{B,k} = \begin{pmatrix} a_{B\uparrow,k} \\ a_{B\downarrow,k} \end{pmatrix}, \tag{5.34}$$

and similarly for MZI^A we may describe the states after QPC_1^A,

$$\mathbf{c}_{A,k} = \mathsf{S}_k^A \mathcal{S}_{0,\nu}^A \mathbf{a}_{A,k}, \qquad \mathbf{a}_{A,k} = \begin{pmatrix} a_{A\uparrow,k} \\ a_{A\downarrow,k} \end{pmatrix}. \tag{5.35}$$

An important point arises here, as described in section 1.2 whilst we assume the scattering matrices are k-independent the phase acquired as result of difference between arm-lengths is not. Which means those matrices which include these phase gains, i.e $\mathsf{S}^d, \mathsf{S}^B, \mathsf{S}^A$ acquire a k-dependence. Whilst we could previously shift away any gain in phase due to arm-length differences, now they must be explicitly incorporated, $\phi_{A,k} = \phi_A + k\Delta l_A$, $\phi_{B,k} = \phi_B + k\Delta l_B$ and $\phi_{d,k} = \phi_d + k\Delta l_d$. Where $\Delta l_{A,B,d}$ describes the differences in arms lengths of up and down arms for $\mathrm{MZI}^{A,B,d}$. The number operators are then upgraded so they don't care what value of k the electron has emerged with,

$$\hat{N}^A = \sum_k c^\dagger_{A\uparrow,k} c_{A\uparrow,k}, \qquad \hat{N}^B = \sum_k d^\dagger_{B\uparrow,k} d_{B\uparrow,k}. \tag{5.36}$$

For the most part the solution will be the same as in the zero temperature case, performing the sum over k for the difference between the Fermi-Dirac distributions results in a factor of eV_C which is then killed by the normalisation. The only difference arises from the k-dependent phase accumulation factors as these are what describe the intrinsic energy scale of the MZIs. If the difference in path lengths in each sector of the Mach-Zehnders is zero, the intrinsic energy scales goes to infinity, and the answer is exactly equivalent to zero temperature, pure input state examples we have previously discussed. Experimentally, equivalent path-difference in each arm are obviously difficult to achieve; particularly since the easiest way to alter the Aharonov-Bohm phase is to alter the area enclosed within the paths which will likely affect the arm lengths. We will see that the process remains largely unaffected by

the results of the unequal path-lengths, apart from a coefficient which will reduce the resolution of the visibility from a thermal smearing of the interference pattern, this smearing can however cause our protocol to fail as a necessary condition for discord in some limits.

We pluck out the correct elements of the scattering matrix to produce the cross-correlation function,

$$\begin{aligned}
\langle \hat{N}^A \hat{N}^B \rangle &= \mathrm{Tr}\{\hat{N}^A \hat{N}^B \rho^{AB}\} \\
&= \frac{1}{e^2 V_A V_B L_A L_B} \sum_{k,q} \left[f_{eV_B}(\hbar v_F k) - f_0(\hbar v_F k) \right] \left[f_{eV_A}(\hbar v_F q) - f_0(\hbar v_F q) \right] \\
&\quad \sum_\nu p_\nu \tilde{N}^A_\nu(q) \Big(|r_d|^2 \tilde{x}_\nu(k) + |t_d|^2 (1 - \tilde{x}_\nu(k)) + |t_d r_d| \,\mathrm{Re}\{\tilde{y}_\nu(k) e^{i\phi_d}\} \Big), \\
&= \sum_\nu p_\nu N^A_\nu(V_A, T) \Big(|r_d|^2 x_\nu(V_B, T) + |t_d|^2 (1 - x_\nu(V_B, T)) \\
&\quad + 2|t_d r_d| \,\mathrm{Re}\{y_\nu(V_B, T) e^{i\phi_d}\}. \qquad (5.37)
\end{aligned}$$

In going from the second line to the third we replaced the summations over k, q with energy integrals e.g $1/L \sum_k \to \int dE$ and then performed the integration using the identities given in Appendix A. The $\tilde{N}^A_\nu$ and $\tilde{x}, \tilde{y}$ variables in Eq.(5.37) represent elements of the full scattering matrix describing the different path the electron can take from the S^A_1 to D^A_1 and the paths from S^B_1 and to the entrance of MZI^d respectively. They are given as,

$$\begin{aligned}
\tilde{N}^A_\nu(q) &= |r_{A_0\nu} r_A e^{i(\phi_A + q\Delta l_A)} + t^*_{A_0\nu} t_A|^2, \\
\tilde{x}_\nu(k) &= |r_{B_0\nu} r_B e^{i(\phi_B + k\Delta l_B)} + t^*_{B_0\nu} t_B|^2, \\
\tilde{y}_\nu(k) &= t_{B_0\nu} r_{B_0\nu} \big(|t_B|^2 e^{-i\phi_B + ik(\Delta l_d - \Delta l_B)} - |r_B|^2 e^{i\phi_B + ik(\Delta l_d + \Delta l_B)} \big) \qquad (5.38) \\
&\quad + (|t_{B_0\nu}|^2 - |r_{B_0\nu}|^2) r_B t_B e^{ik\Delta l_d}.
\end{aligned}$$

Upon integration the k/q-independent terms gain a factor of eV_A/eV_B which is then killed by the normalisation. Those with a k/q-dependent oscillatory term keep a voltage and temperature dependence after the variables are integrated. Subsequent to performing the integration the variables are given by,

$$\begin{aligned}
x_\nu(V_b,T) &= |r_{B_0\nu}|^2|r_B|^2 + |t_{B_0\nu}|^2|t_B|^2 \\
&\quad +2|r_{B_0\nu}t^*_{B_0\nu}r_Bt_B|K(\Delta l_B,V_B,T)\cos\!\left(\phi_B+\frac{\Delta l_B eV_B}{2\hbar v_F}\right), \\
N^A_\nu(V_A,T) &= |r_{A_0\nu}|^2|r_A|^2 + |t_{A_0\nu}|^2|t_A|^2 \\
&\quad +2|r_{A_0\nu}t^*_{A_0\nu}r_At_A|K(\Delta l_A,V_A,T)\cos\!\left(\phi_A+\frac{\Delta l_A eV_A}{2\hbar v_F}\right), \\
y_\nu(V_b,T) &= e^{\frac{i\Delta l_d eV}{2\hbar v_F}}\Big[\big(|t_{B_0\nu}|^2-|r_{B_0\nu}|^2\big)r_Bt_BK(\Delta l_d,V_B,T) \\
&\quad -t_{B_0\nu}r_{B_0\nu}\Big(-|t_B|^2K((\Delta l_d-\Delta l_B),V_B,T)e^{-i(\phi_B+\frac{\Delta l_B eV_B}{2\hbar v_F})} \\
&\quad +|r_B|^2K((\Delta l_d+\Delta l_B),V_B,T)e^{i(\phi_B+\frac{\Delta l_B eV_B}{2\hbar v_F})}\Big)\Big].
\end{aligned} \tag{5.39}$$

with,

$$K(\Delta l,V,T)=\frac{2\pi k_BT\sin\!\left(\frac{eV\Delta l}{2\hbar v_F}\right)}{eV\sinh\!\left(\frac{\pi k_BT\Delta l}{\hbar v_F}\right)}. \tag{5.40}$$

which describes the suppression of interference as a result of the broadening of the energy and non-pure initial state. We can then extract the visibility as a function of ϕ_d using Eq. (5.6) as follows,

$$\mathcal{V}[\phi_d]=\frac{\big|\sum_\nu p_\nu N^A_\nu y_\nu(V_B,T)\big|}{\sum_\nu p_\nu N^A_\nu}, \qquad \text{if}|t_d|^2=|r_d|^2=1/2. \tag{5.41}$$

As was the case in Section 5.4, to make $\mathcal{V}[\phi_d]$ independent of $\{N^A_\nu\}$ we require that $x_\nu(V_B,T)=\pm x_\mu(V_B,T)$ for all ν,μ (or that $N^A_\nu=N^A_\mu$). We now see there are additional voltage and temperature dependent features in Eqs. (5.39) which were

not present in Eqs. (5.11). In the following we consider in what limits these features can cause our protocol to fail as a necessary and sufficient condition for discord.

5.8.2 Conditions for False Witnesses

We first consider the case in which $\Delta l_B = 0$, but the length differences in MZI^A and MZI^d are non-zero. In which case the trivial solution for zero visibility, given by $N_{A,i} = N_{A,j}$ for all i, j, can be satisfied for non-identical ρ_ν^A if $K(\Delta l_A, V_A, T) = 0$. Similarly $\mathcal{V}[\phi_d]$ (and even more worryingly) goes to zero for any $\{\rho_\nu^B\}$ if $K(\Delta l_d, V_B, T) = 0$, this is a result of the fact that in this case the interference pattern at QPC^d is smeared so much that the dependence on ϕ_d becomes hidden. Our protocol therefore fails to be a necessary condition for discord in the case where $K(\Delta l_A, V_A, T) = 0$ and the protocol fails entirely if $K(\Delta l_d, V_B, T) = 0$. To find when this is the case, we start from the pure initial state, zero temperature limiting case and proceed to loosen the limits on the temperature T and the voltages V_A, V_B to see when false witnesses for zero discord in our protocol can occur. The pure state, zero temperature limit is given by the conditions,

$$E_A \gg \pi k_B T, eV_A \qquad \text{and} \qquad E_d \gg \pi k_B T, eV_B \tag{5.42}$$

where $E_A = \hbar v_F / \Delta l_A$ and $E_d = \hbar v_F / \Delta l_d$ and describe the intrinsic energy scales of MZI^A and MZI^d respectively. In the limits given by Eq. (5.42) both $K(\Delta l_A, V_A, T)$, $K(\Delta l_d, V_B, T) \to 1$ and therefore the protocol can't produce a false witness for zero discord in this limiting case, in agreement with our previous single particle discussions. Firstly we will loosen the thermal constraints (but keep the constraints

on V_A and V_B),

$$\lim_{eV_A \ll E_A} K(\Delta l_A, V_A, T) \rightarrow \frac{\pi k_B T}{E_A \sinh\left(\frac{\pi k_B T}{E_A}\right)}, \tag{5.43}$$

$$\lim_{eV_B \ll E_d} K(\Delta l_d, V_B, T) \rightarrow \frac{\pi k_B T}{E_d \sinh\left(\frac{\pi k_B T}{E_d}\right)}. \tag{5.44}$$

We therefore see that our protocol fails as a necessary condition in the case $\pi k_B T \gg E_A$, and fails totally for the case $\pi k_B T \gg E_d$.

In the converse scenario, where the restrictions on the voltages V_A, V_B in Eq. (5.42) are loosened but temperature constraints remain in place we obtain,

$$\lim_{T \ll E_A} K(\Delta l_A, V_A, T) \rightarrow \frac{2E_A \sin\left(\frac{eV_A}{2E_A}\right)}{eV_A}, \tag{5.45}$$

$$\lim_{T \ll E_d} K(\Delta l_d, V_B, T) \rightarrow \frac{2E_d \sin\left(\frac{eV_B}{2E_d}\right)}{eV_B}. \tag{5.46}$$

In which case we see our protocol fails as a necessary condition in the case $eV_A \gg E_A$ or $eV_A = 2n\pi E_A$, and fails totally for the case $eV_B \gg E_d$ or $eV_B = 2n\pi E_d$, where $n > 1$ and integer. Neglected here is also the effect of the decoherence to the environment, if V_B or V_A is large this is expected to play a large role as it is very energetically favourable for the electron to relax into lower energy states via interaction with the environment. This will therefore likely provide tighter restrictions on the voltages.

Finally, relaxing both the temperature and voltage constraints simultaneously and taking the full broadening function Eq. (5.40) gives us one further possibility for

$K \to 0$ (and therefore our protocol to fail) this is given by,

$$eV_A \gg 2\pi k_B T, \qquad \pi k_B T \sim E_A, \tag{5.47}$$

$$eV_B \gg 2\pi k_B T, \qquad \pi k_B T \sim E_d. \tag{5.48}$$

We again see that our witness is no longer a necessary condition if Eq. (5.47) is met and fails entirely in the case that Eq.(5.48) is satisfied. We therefore note that in current experimental set-ups in condensed matter MZI experiments, where the conditions are such that (at worse) $\pi k_B T \sim E_{MZI} > eV$ our protocol is still absolutely valid. We do stress however that optimal conditions are $E_{MZI} \gg \pi k_B T, eV$ as this has the least broadening of the interference pattern and therefore the greatest resolution of the $\mathcal{V}[\phi_d] = 0$ lines.

The above failing of the protocol are all a result of the fact the broadening function hides the interference oscillations at the detectors $D^{B,A}$. When we take the length difference Δl_B to be non-zero it affects the rotation we need to make at QPC_1^B to diagonalise the initial state so the situation becomes a little more complicated, nonetheless we may include the case where all three length $\Delta l_A, \Delta l_d$ and Δl_B are taken to be non-zero. Adding a non-zero Δl_B can only affect the protocol if both $K(\Delta l_d - \Delta l_B), K(\Delta l_d + \Delta l_B) \to 0$, in this case the protocol once again ceases to become a necessary condition for discord. Using similar logic to the previous cases we may deduce two further conditions where our protocol fails, $\pi k_B T \gg \frac{\hbar v_F}{|\Delta l_B + \Delta l_d|}, \frac{\hbar v_F}{|\Delta l_B - \Delta l_d|}$ or $eV_B \gg \frac{\hbar v_F}{|\Delta l_B + \Delta l_d|}, \frac{\hbar v_F}{|\Delta l_B - \Delta l_d|}$.

In conclusion, we find our protocol is perfectly valid within the current experimental condition for Mach-Zehnders of temperature and voltage (albeit with reduced experimental resolution when these parameters are non-zero). We have however

also ignored dephasing of the electron to environment which would provide further (though not necessarily tighter) restrictions on the total length of the Mach-Zehnders as well as the temperature and voltages, however providing the electron remains coherent at the sort of length scales we are discussing (and we see from experiment that they do [41, 13, 11]) we don't anticipate this to effect the results at experimental length scales. We proceed to consider the non-interacting many body effects.

5.8.3 Many-Body

Since our joint operator is a combination of single operators acting on the separate systems, the finite-temperature single particle case contains most of the necessary physics for a many-body, non-interacting description. Instead of the number projector $\hat{N}^A$ and $\hat{N}^B$ given in Eq. (5.36) we consider the current operators at the drains. As discussed in section 1.2, the current operator for a linear dispersion is given by $\hat{I}_{C,m}(x,t) = ev_F : \psi^\dagger_{C,m}(x,t)\psi_{C,m}(x,t) :$, where $C = A, B$ (describing current in subsystems A and B) and $m =\uparrow,\downarrow$ (describes whether measurement is taken in $\uparrow$ or $\downarrow$ arm of the Mach Zehnder). We are interested only in current measurements after QPC^d (located at $x = x_{\mathrm{QPC}^d}$) and QPC_1^A at which points the systems ψ-operators are given in the Heisenberg representation as,

$$\psi_{A,m}(x,t) = \frac{1}{\sqrt{L}}\sum_k e^{ik(x-v_F t)}c_{A,m,k}, \qquad \text{for } x > x_{\mathrm{QPC}_1^A}, \tag{5.49}$$

$$\psi_{B,m}(x,t) = \frac{1}{\sqrt{L}}\sum_k e^{ik(x-v_F t)}d_{m,k}, \qquad \text{for } x > x_{\mathrm{QPC}^d}. \tag{5.50}$$

Where the operators $\mathbf{c}_{A,k}$ and $\mathbf{d}_k$ are given by Eq. (5.35) and (5.34) respectively. Note, similarly to in Eq. (1.16) we could construct the ψ-operators in all regions of the MZIs using the scattering matrices for each QPC, but it is unnecessary for our purposes so we choose not to. Using this formalism, the joint-current correlation

expectation value at a measurement time $t = 0$ in upper arm of each MZI is given as,

$$\langle \hat{I}_{A,\uparrow}(x_A, 0)\hat{I}_{B,\uparrow}(x_B, 0)\rangle = (ev_F)^2 \langle : c^\dagger_{A,\uparrow,k} c_{A,\uparrow,k} : \rangle \langle : d^\dagger_{\uparrow,k} d_{\uparrow,k} : \rangle , \tag{5.51}$$

where x_A, x_B are the position of the detectors on subspace A and B respectively. We have used here that the electron operators on A and B subsystems are uncorrelated and therefore can be separated into separate expectation values. We may then relate the $c_{A,\uparrow,k}$ and $d_{\uparrow,k}$ operators to the corresponding subspace operators at the sources (see Eq. (5.35) and (5.34)) and relate the expectation values of these operators to the voltage bias by employing $\langle a^\dagger_{A(B),m,k} a_{A(B),m,k}\rangle = f(v_F k - \mu_{A(B),m})$. Where, since $S^A_\downarrow$ and $S^B_\downarrow$ are grounded, $\mu_{A(B)\downarrow} = 0$ and as we bias $S^A_\uparrow$ and $S^B_\uparrow$ with voltages V_A and V_B respectively, $\mu_{A(B),\uparrow} = eV_{A(B)}$. Undergoing this process we see we are returned close to the same expression given as Eq. (5.37), we define $\langle \hat{N}^A \hat{N}^B\rangle_{single} \equiv \langle \hat{N}^A \hat{N}^B\rangle$ in this expression. We obtain the joint-current expectation value as,

$$\langle \hat{I}_{A,\uparrow}(x_A, t)\hat{I}_{B,\downarrow}(x_B, t)\rangle = \left(\frac{e^2 V_A}{h}\right)\left(\frac{e^2 V_B}{h}\right) \langle \hat{N}^A \hat{N}^B\rangle_{single} , \tag{5.52}$$

Since the many-particle case is equivalent up to a factor, the investigation in the previous section is still valid (although note that we are now returned the correct zero particle limit when $V_{A,B} = 0$). We therefore conclude that even in the presence of many (non-interacting) particles at finite temperature in conditions in which current experiments are conducted, our protocol is able to identify discorded states.

Conclusion

In this thesis we have investigated the physics of edge states in the quantum Hall regime. We demonstrated that the nature of graphene's two-valley, gapless spectrum means that the PN junction in the quantum Hall regime prove to be an interesting and useful device. Experiments in this system have generated conflicting results; we provide evidence that it is the strength of disorder mediated tunnelling between chiral modes that is the likely cause of these differences. Typically in quantum mechanics quantisation is associated with purity, but, perhaps counter-intuitively, one of our key results describes how a high degree of disorder leads to the quantised conductance observed in a number of experiments [26, 28, 90]. In more ordered samples the high electron mobilities and similarity of the paths which excitations on the different sides of a PN interface are forced to take, mean coherences of an electron in a superposition of both sides of junction interface are robust [11]. The system therefore lends itself as the basis of a high-quality electronic Mach-Zehnder. We considered whether such a device in graphene may experience additional interactions as a result of how close chiral modes are to each other. We explore and catalogue interactions which are likely to be relevant along the PN interface. Then, expanding on the work of others [30, 31], we build a MZI model which incorporates these additional cross-channel terms. We calculate the Green's function of the diagonal excitations of this Hamiltonian, and make use of this propagator to calculate the oscillatory behaviour of the MZI current with the cross-channel interactions in-

cluded. We find that (within the limits we consider) there is little differences to the current found in the case of the intra-channel interactions only model.

We proceed to introduce the recently popularised concept of quantum discord [15, 16]. Discord characterises quantum correlations which go beyond entanglement. Its robustness to decoherence, as compared to entanglement [19], means that it is an attractive resource in quantum information and has had an array of suggested uses [18, 116, 115]. In spite of the interest in the topic, actual witnesses of discord have proved quite elusive. The difficulty in measuring discord stems from the fact it is an entropic measure, which means it is a complex non-linear function of the density matrix, and therefore difficult (if not impossible) to measure directly without full density matrix tomography. We propose a simple method of generating and detecting discord within a solid-state system by using an electronic MZI as the basis. This protocol enables us to construct an experimentally accessible measure for discord. The graphical form of our measure is similar to that of discord in its original definition, but forgoes the need for direct evaluation of the information entropy. Furthermore we consider more physical experimental conditions such as finite temperature and the effects of many (non-interacting) electrons. We demonstrate that our protocol remains rather robust to these conditions.

Appendices

Appendix A

Fermi-Dirac Integrals

In this appendix we give the results to all the integrals involving Fermi-Dirac functions performed in this thesis. First the integral of a Fermi function combined with a phase,

$$\int_{-\infty}^{\infty} d\epsilon\ f_\mu(\epsilon) e^{ix\epsilon} = \int_{-\infty}^{\infty} d\epsilon\ \frac{e^{ix\epsilon}}{e^{\beta(\epsilon-\mu)}+1},$$

with $\beta = k_B T$. We can compute this using a contour integral approach, the poles of the argument of the integral are given by, $\phi(\epsilon) \equiv e^{\beta(\epsilon-\mu)} + 1 = 0$, which then give us $\beta(\epsilon_n - \mu) = i\pi(2n+1)$, via the residue theorem we then obtain,

$$\begin{aligned}
\int_{-\infty}^{\infty} d\epsilon\ f_\mu(\epsilon) e^{ix\epsilon} &= 2\pi i \sum_{n=0}^{\infty} \frac{e^{-x(\pi k_B T(2n+1)+i\mu)}}{\phi'(\epsilon_n)}, \\
&= -2\pi i k_B T e^{-\pi k_B T x} e^{i\mu x} \sum_{n=0}^{\infty} e^{-2\pi k_B T x n}, \\
&= -2\pi i k_B T e^{i\mu x} \frac{e^{-\pi k_B T x}}{1 - e^{-2\pi k_B T x}}, \\
&= -2\pi i k_B T \frac{e^{i\mu x}}{\sinh\left(\pi k_B T x\right)}.
\end{aligned} \tag{A.1}$$

Typically x in this equation is of the form $\frac{\Delta l}{\hbar v_F}$ producing integrals such as,

$$\int_{-\infty}^{\infty} d\epsilon \; f_\mu(\epsilon) e^{i\frac{\Delta l}{\hbar v_F}\epsilon} = -\frac{2\pi i k_B T e^{i\frac{\Delta l e V}{\hbar v_F}}}{\sinh\left(\pi k_B T \Delta l/\hbar v_F\right)}. \tag{A.2}$$

Consider next integrals which calculate the amount of states between distributions with different chemical potentials, these return,

$$\int_{-\infty}^{\infty} d\epsilon \left[f_\mu(\epsilon) - f_0(\epsilon)\right] = \mu \tag{A.3}$$

Integrals involving combinations of Fermi-Dirac functions typically emerge from cross-correlation functions e.g. noise. An example of such a combination that we utilise in this thesis is,

$$\int d\epsilon \; f_\alpha(\epsilon)(1 - f_\beta(\epsilon)). \tag{A.4}$$

If $\alpha = \beta$ we may use $\frac{df_\alpha(\epsilon)}{d\epsilon} = -\beta f_\alpha(\epsilon)(1 - f_\alpha)$ in which case,

$$\int d\epsilon \; f_\alpha(\epsilon)(1 - f_\alpha(\epsilon)) = -\frac{1}{\beta}\int df_\alpha(\epsilon) = k_B T \tag{A.5}$$

For $\alpha \neq \beta$,

$$\int d\epsilon \; f_\alpha(\epsilon)(1 - f_\beta(\epsilon)) = \frac{\Delta\mu}{1 - e^{-\beta\Delta\mu}} \tag{A.6}$$

with $\Delta\mu = \mu_\alpha - \mu_\beta$, (A.6) correctly reproduces (A.5) when the limit $\Delta\mu \to 0$ is taken.

Appendix B

Calculation of Noise

In this appendix we consider in depth how one goes about calculating noise using the scattering formulation used throughout this theis. We use the expression for the reduced noise igven by,

$$S_{\alpha,\beta} \equiv \lim_{\tau\to\infty} \int_{-\tau/2}^{\tau/2} dt \, \langle I_\alpha(x_\alpha,t) I_\beta(x_\beta,0)\rangle - \langle I_\alpha(x_\alpha,t)\rangle \langle I_\beta(x_\beta,0)\rangle \,, \tag{B.1}$$

where current operators can then be expressed as,

$$I_\alpha(x,t) = ev_F : \psi_\alpha^\dagger(x,t)\psi_\alpha(x,t) : . \tag{B.2}$$

Evaluating the reduced current noise at $D1$, given by S_{11}.

$$\begin{aligned} S_{\alpha\beta} &= (ev_F)^2 \int dt \Big[\langle : \psi_\alpha^\dagger(x_0,t)\psi_\alpha(x_0,t) :: \psi_\beta^\dagger(x_0,0)\psi_\beta(x_0,0) : \rangle \\ &\quad - \langle : \psi_\alpha^\dagger(x_0,t)\psi_\alpha(x_0,t) : \rangle \langle : \psi_\beta^\dagger(x_0,0)\psi_\beta(x_0,0) : \rangle \Big], \\ &= (ev_F)^2 \int dt \Big[\langle \psi_\alpha^\dagger(x_0,t)\psi_\alpha(x_0,0)\rangle \langle \psi_\beta(x_0,t)\psi_\beta^\dagger(x_0,0)\rangle \Big]. \end{aligned} \tag{B.3}$$

In going from the first line to the second we use Wick's theorem to expand the two-body correlator, the first term in the expansion is then killed by the $\langle I_\alpha \rangle \langle I_\beta \rangle$ term. We then describe the field operators in terms of electron operators with a free fermion time dependence,

$$\psi_\alpha(x_0,t) = \frac{1}{\sqrt{L}} \sum_k e^{ik(x_0 - v_F t)} c_k \tag{B.4}$$

In the scattering theories used throughout this thesis the implicit assumption is that although we don't immediately know the distribution function of the c_k operators, we are able to deduce how these operators relate back to electrons states which are in thermal equilibrium and are therefore described by known distribution functions. The process of solving the Hamiltonian for its eigenstates is then finding the matrices which relate these operators together. Two examples of these mappings are given by Eq. (1.17) and Eq. (3.17). We can define a general tranfer matrix, $\mathcal{A}$, which describes a_k propagation towards c_k, $\mathbf{c}_k = \mathcal{A}\mathbf{a}_k$ In the case of Eq. (1.17), with $x_0 > l_{1,2}$, the transfer matrix is given by $\mathcal{A} = \left(\mathcal{S}_B \mathcal{S}_A\right)$ where the scattering matrices $\mathcal{S}_{A,B}$ are defined by Eq. (1.18). In the case of Eq. (3.17) for $x_0 > L$ the transfer matrix is given by $\mathcal{A} = \mathcal{S}$, where $\mathcal{S}$ is defined by Eq. (3.16). We may therefore rewrite Eq. (B.3) in terms of the elements of $\mathcal{A}$

$$\begin{aligned}
S_{\alpha\beta} &= (ev_F)^2 \int dt\, \frac{1}{L^2} \sum_{\substack{k_1,k_2 \\ k_3,k_4}} \sum_{\substack{i,j, \\ l,m}} e^{iv_F(k_1-k_3)t} \mathcal{A}^\dagger_{i\alpha} \mathcal{A}_{\alpha j} \mathcal{A}_{l\beta} \mathcal{A}^\dagger_{\beta m} \left\langle a^\dagger_{i,k_1} a_{j,k_2} \right\rangle \left\langle a_{l,k_3} a^\dagger_{m,k_4} \right\rangle , \\
&= (ev_F)^2 \int_{-\tau/2}^{\tau/2} dt\, \frac{1}{L^2} \sum_{k_1,k_3} \sum_{i,j} |\mathcal{A}_{i\alpha}|^2 |\mathcal{A}_{j\beta}|^2 e^{iv_F(k_1-k_3)t} \left\langle a^\dagger_{i,k_1} a_{i,k_1} \right\rangle \left\langle a_{j,k_3} a^\dagger_{j,k_3} \right\rangle , \\
&= (ev_F)^2 \frac{1}{L^2} \sum_{k_1,k_3} \frac{2\sin((k_3-k_1)v_F\tau/2)}{v_F(k_1-k_2)} \sum_{i,j} |\mathcal{A}_{i\alpha}|^2 |\mathcal{A}_{\beta j}|^2 e^{i\hbar v_F(k_1-k_3)} \\
&\quad \left\langle a^\dagger_{i,k_1} a_{i,k_1} \right\rangle \left\langle a_{j,k_3} a^\dagger_{j,k_3} \right\rangle .
\end{aligned}$$

In going from the first to the second line we used that a-operators are uncorrelated for different arm indices and different momenta, we proceeded to perform the time integral to obtain the third line. In the limit that $\tau \gg L/v_F$ the τ-dependent part tends to δ_{k_1,k_3}, which we may use to perform one of the momentum summations. Additionally we finally make use of our assumption that a-operators originate from thermal reservoirs meaning that we may represent their expectation value as $\langle a^\dagger_{i,k} a_{i,k}\rangle = f_{\mu_i}(v_F k)$ to obtain,

$$\begin{aligned} S_{\alpha\beta} &= e^2 v_F \frac{1}{L}\sum_k \sum_{i,j} |\mathcal{A}_{i\alpha}|^2 |\mathcal{A}_{\beta j}|^2 f_{\mu_i}(v_F k)\big[1 - f_{\mu_j}(v_F k)\big], \\ &= \frac{e^2}{h}\sum_{i,j}\int dE\ |\mathcal{A}_{i\alpha}|^2 |\mathcal{A}_{\beta j}|^2 f_{\mu_i}(E)\big[1 - f_{\mu_j}(E)\big]. \end{aligned}$$

This formula is a general formula of noise for any number of (equal number) inputs and outputs with different voltage biases. We generally restrict ourselves to 2 inputs and 2 ouputs where only one input is biased ($\mu_1 = eV$, $\mu_2 = 0$) in this case, expanding the sum out gives.

$$\begin{aligned} S_{\alpha\beta} = \frac{e^2}{h}\int dE \Big(&|\mathcal{A}_{1\alpha}|^2 |\mathcal{A}_{\beta 1}|^2 f_{eV}(E)\big[1 - f_{eV}(E)\big] + |\mathcal{A}_{1\alpha}|^2 |\mathcal{A}_{\beta 2}|^2 f_{eV}(E)\big[1 - f_0(E)\big] \\ &+ |\mathcal{A}_{2\alpha}|^2 |\mathcal{A}_{\beta 1}|^2 f_0(E)\big[1 - f_{eV}(E)\big] + |\mathcal{A}_{2\alpha}|^2 |\mathcal{A}_{\beta 2}|^2 f_0(E)\big[1 - f_0(E)\big] \Big). \end{aligned}$$

The integrals can then be performed with the help of the identities in Appendix A to obtain,

$$\begin{aligned} S_{\alpha\beta} = \frac{e^2}{h}\Bigg(&\Big[|\mathcal{A}_{1\alpha}|^2 |\mathcal{A}_{\beta 1}|^2 + |\mathcal{A}_{2\alpha}|^2 |\mathcal{A}_{\beta 2}|^2\Big] k_B T + |\mathcal{A}_{1\alpha}|^2 |\mathcal{A}_{\beta 2}|^2 \frac{eV}{1 - e^{-\beta eV}} \\ &+ |\mathcal{A}_{2\alpha}|^2 |\mathcal{A}_{\beta 1}|^2 \frac{eV}{1 - e^{\beta eV}} \Bigg). \end{aligned} \tag{B.5}$$

The above formula can be used to calculate the cross-correlation of noise between any two outputs where the system determines how we define $\mathcal{A}$. With the correct

parameters put in, this formula gives Eq. (3.24) describing the noise along a PN junction with a hybridisation region and Eq. (3.29) which describes the noise in an electronic Mach-Zehnder interferometer.

Appendix C

Bosonic Correlation Functions

Determination of $S_m(x,t)$ as defined Eq. (3.48) comes down to evaluation of a combination of bosonic expectation values of the form $\langle\phi_m(x,t)\phi_m(x',t')\rangle$, these may be evaluated by writing the field operators ϕ_m explicitly in terms of bosonic creation and annhilation operators using Eq. (1.33) using standard bosonic commutation relations this then gives,

$$\langle\phi_m(x,t)\phi_m(x',t')\rangle = \sum_{q>0}\frac{1}{n_q}\left[e^{iq(x-x'-u_m(t-t'))} + 2\cos\left[q(x-x'-u_m(t-t')\right]\langle b^\dagger_{q,m}b_{q,m}\rangle\right].$$

As the statistics is bosonic the expectation value is given by the standard Bose-Einstein distribution, $\langle b^\dagger_{q,m}b_{q,m}\rangle = (e^{\beta\hbar u_m q}-1)^{-1}$. Eq. (3.48) can then be determined using this expression to be,

$$S_m(x,t) = -\ln\epsilon - \sum_{q>0}\frac{1}{n_q}\left(\coth\left(\frac{\hbar u_m q}{2}\right)\left[1+\cos(qx-u_m qt)\right] - i\sin(qx-u_m qt)\right), \tag{C.1}$$

We proceed to take the zero temperature limit,

$$\lim_{T\to 0} S_m(x,t) = -\ln\epsilon - \sum_{q>0}\frac{1}{n_q}e^{-\epsilon q}\big[1-e^{-iq(x-u_m t)}\big], \tag{C.2}$$

and then directly evaluate this sum by changing variables to $n_q = Lq/2\pi$ and making use of the identity $-\sum_{n=1}^{\infty}\frac{x^n}{n} = \ln(1-x)$.

$$\begin{aligned}
-\sum_{q>0}\frac{1}{n_q}e^{-\epsilon q}\big[1-e^{-iq(x-u_m t)}\big] &= -\sum_{n_q=1}\frac{1}{n_q}(e^{-\frac{2\pi}{L}\epsilon})^{n_q} + \sum_{n_q=1}\frac{1}{n_q}\big(e^{\frac{2\pi}{L}(-i(x-u_m t)-\epsilon)}\big)^{n_q},\\
&= \ln\Big(1-e^{-\frac{2\pi}{L}\epsilon}\Big) - \ln\Big(1-e^{\frac{2\pi}{L}(-i(x-u_m t)-\epsilon)}\Big),\\
\lim_{L\to\infty} &= \ln\left(\frac{2\pi}{L}\epsilon\right) - \ln\left(\frac{2\pi}{L}\big[\epsilon+i(x-u_m t)\big]\right),\\
&= \ln(\epsilon) - \ln\big[\epsilon+i(x-u_m t)\big].
\end{aligned} \tag{C.3}$$

This finally gives us $S_m(x,t)$ in the zero temperature, $L\to\infty$ limit as,

$$S_m(x,t) = -\ln\big[i(x-u_m t)+\epsilon\big]. \tag{C.4}$$

Bibliography

[1] B. I. Halperin, Phys. Rev. B **25**, 2185 (1982). 1

[2] X. G. Wen, Phys. Rev. B **43**, 11025 (1991). 1

[3] C. L. Kane and M. P. A. Fisher, *Edge-State Transport* in *Perpectives in Quantum Hall Effects* (Wiley, 1996). 1, 8

[4] D. C. Tsui, H. L. Stormer, and A. C. Gossard, Phys. Rev. Lett. **48**, 1559 (1982). 1

[5] R. B. Laughlin, Phys. Rev. Lett. **50**, 1395 (1983). 1

[6] X.-G. Wen, *Quantum Field Theory of Many-Body Systems* (Oxford Univ. Press, Cambridge, 2004). 1, 11

[7] J. Jain, *Composite Fermions* (Cambridge Univ. Press, Cambridge, 2007). 1

[8] B. I. Halperin, Phys. Rev. Lett. **52**, 1583 (1984). 1

[9] A. K. Geim and K. S. Novoselov, Nature Materials **6**, 183 (2007). 2, 25

[10] Y. Zhang *et al.*, Physical Review Letters **96**, 136806 (2006). 2, 3, 47, 70

[11] D. S. Wei *et al.*, Science Advances **3** (2017). 2, 3, 26, 49, 53, 60, 66, 68, 69, 70, 125, 127

[12] Y. Ji *et al.*, Nature **422**, 415 (2003). 2, 3, 5, 11, 69

[13] I. Neder, M. Heiblum, Y. Levinson, D. Mahalu, and V. Umansky, Physical Review Letters **96**, 016804 (2006). 2, 3, 11, 16, 125

[14] R. F. Werner, Phys. Rev. A **40**, 4277 (1989). 2, 89

[15] H. Ollivier and W. H. Zurek, Physical Review Letters **88**, 017901 (2001). 2, 4, 85, 87, 89, 128

[16] L. Henderson and V. Vedral, Journal of Physics A: Mathematical and General **34**, 6899 (2001). 2, 4, 85, 88, 89, 128

[17] B. P. Lanyon, M. Barbieri, M. P. Almeida, and A. G. White, Phys. Rev. Lett. **101**, 200501 (2008). 2

[18] A. Datta, A. Shaji, and C. M. Caves, Phys. Rev. Lett. **100**, 050502 (2008). 2, 91, 128

[19] L. Mazzola, J. Piilo, and S. Maniscalco, Physical Review Letters **104**, 200401 (2010). 2, 92, 128

[20] R. Rahimi and A. SaiToh, Phys. Rev. A **82**, 052101 (2010). 2, 83, 92

[21] J. Luttinger, J. Math. Phys. **4**, 1154 (1963). 3, 9, 18

[22] S.-i. Tomonaga, Progress of Theoretical Physics **5**, 544 (1950). 3, 9

[23] F. D. M. Haldane, Journal of Physics C: Solid State Physics **14**, 2585 (1981). 3, 19, 22, 23

[24] J. von Delft and H. Schoeller, Annalen der Physik **7**, 225 (1998). 3, 18, 22, 80

[25] A. H. Castro Neto, F. Guinea, and N. M. R. Peres, Physical Review B **73** (2006). 3, 70

[26] J. R. Williams, L. DiCarlo, and C. M. Marcus, Science **317**, 638 (2007). 3, 26, 52, 61, 64, 68, 69, 127

[27] B. Özyilmaz *et al.*, Physical Review Letters **99**, 166804 (2007). 3, 26, 52

[28] N. Kumada, F. D. Parmentier, H. Hibino, D. C. Glattli, and P. Roulleau, Nature Communications **6**, 8068 (2015). 3, 52, 61, 64, 65, 66, 68, 69, 127

[29] F. Amet, J. Williams, K. Watanabe, T. Taniguchi, and D. Goldhaber-Gordon, Physical Review Letters **112**, 196601 (2014). 3, 26, 53, 60, 68, 69, 70

[30] J. T. Chalker, Y. Gefen, and M. Y. Veillette, Physical Review B **76**, 085320 (2007). 3, 12, 16, 17, 70, 76, 78, 80, 127

[31] I. P. Levkivskyi and E. V. Sukhorukov, Physical Review B **78**, 045322 (2008). 3, 17, 70, 127

[32] K. Modi, A. Brodutch, H. Cable, T. Paterek, and V. Vedral, Reviews of Modern Physics **84**, 1655 (2012). 4, 88, 90

[33] K. v. Klitzing, G. Dorda, and M. Pepper, Phys. Rev. Lett. **45**, 494 (1980). 5

[34] D. Yoshioka, *The Quantum Hall Effect* (Springer Series in Solid-State Science, 2002). 6

[35] R. B. Laughlin, Phys. Rev. B **23**, 5632 (1981). 6

[36] L. Landau and E. Lifshitz, *Quantum Mechanics Non-Relativistic Theory* (Pergamon Press, 1958). 6

[37] M. O. Goerbig, arXiv preprint arXiv:0909.1998 (2009). 7

[38] B. I. Halperin, Phys. Rev. B **25**, 2185 (1982). 11

[39] X. G. Wen, Phys. Rev. Lett. **64**, 2206 (1990). 11

[40] X.-G. Wen, Physical Review B **50**, 5420 (1994). 11

[41] P. Roulleau *et al.*, Physical Review Letters **100**, 126802 (2008). 11, 16, 69, 125

[42] D. Leibfried *et al.*, Nature **422**, 412 (2003). 11, 70

[43] C. L. Kane and M. P. Fisher, Physical Review B **56**, 15231 (1997). 12

[44] V. Shpitalnik, Y. Gefen, and A. Romito, Physical Review Letters **101**, 226802 (2008). 13, 83

[45] O. Zilberberg, A. Romito, and Y. Gefen, Physical Review B **93**, 115411 (2016). 13

[46] L. V. Litvin, H.-P. Tranitz, W. Wegscheider, and C. Strunk, Phys. Rev. B **75**, 033315 (2007). 16

[47] R. C. Ashoori, H. L. Stormer, L. N. Pfeiffer, K. W. Baldwin, and K. West, Phys. Rev. B **45**, 3894 (1992). 16

[48] P. Roulleau *et al.*, Phys. Rev. B **76**, 161309 (2007). 16

[49] I. Gurman, R. Sabo, M. Heiblum, V. Umansky, and D. Mahalu, Physical Review B **93**, 121412 (2016). 16, 70

[50] D. L. Kovrizhin and J. T. Chalker, Physical Review B **81**, 155318 (2010). 17, 70, 80

[51] M. J. Rufino, D. L. Kovrizhin, and J. T. Chalker, Physical Review B **87**, 045120 (2013). 17, 70

[52] S. Ngo Dinh and D. A. Bagrets, Phys. Rev. B **85**, 073403 (2012). 17

[53] M. Schneider, D. A. Bagrets, and A. D. Mirlin, Phys. Rev. B **84**, 075401 (2011). 17, 70

[54] D. C. Mattis and E. H. Lieb, J. Math. Phys. **6**, 304 (1965). 18

[55] K. D. Schotte and U. Schotte, Phys. Rev. **182**, 479 (1969). 18

[56] I. E. Dzyaloshinskii and A. I. Larkin, Sov. Phys. JETP **38**, 202 (1974). 18

[57] A. Luther and I. Peschel, Phys. Rev. B **9**, 2911 (1974). 18

[58] F. D. M. Haldane, J. Phys. C. **12**, 4791 (1979). 18

[59] A. Altland and B. Simons, *Condensed Matter Field Theory* (Cambridge Univ. Press, Cambridge, 2010). 20

[60] K. S. Novoselov *et al.*, Science **306**, 666 (2004). 25

[61] C. Lee, X. Wei, J. W. Kysar, and J. Hone, Science **321**, 385 (2008). 25

[62] L. A. Ponomarenko *et al.*, Science **320**, 356 (2008). 25

[63] A. H. Castro Neto, F. Guinea, N. M. R. Peres, K. S. Novoselov, and A. K. Geim, Reviews of Modern Physics **81**, 109 (2009). 25, 26, 29, 31, 32, 36, 37

[64] M. O. Goerbig, Reviews of Modern Physics **83**, 1193 (2011). 25, 27, 47, 48, 70

[65] Y. Zhang, Y.-W. Tan, H. L. Stormer, and P. Kim, Nature **438**, 201 (2005). 25

[66] K. S. Novoselov *et al.*, Nature **438**, 197 (2005). 25

[67] P. R. Wallace, Phys. Rev. **71**, 622 (1947). 28

[68] M. O. Goerbig, R. Moessner, and B. Douçot, Physical Review B **74**, 161407 (2006). 31, 70

[69] K. S. Novoselov *et al.*, Science **315**, 1379 (2007). 32

[70] N. N. Klimov *et al.*, Physical Review B **92**, 241301 (2015). 33, 34

[71] O. Klein, Zeitschrift für Physik **53**, 157 (1929). 35

[72] M. I. Katsnelson, K. S. Novoselov, and A. K. Geim, Nature Physics **2**, 620 (2006). 35

[73] A. F. Young and P. Kim, Nature Physics **5**, 222 (2009). 35

[74] M. O. Goerbig, Comptes Rendus Physique **12**, 369 (2011). 36

[75] L. Brey and H. A. Fertig, Physical Review B **73**, 195408 (2006). 36, 37

[76] A. F. Young *et al.*, Nature Physics **8**, 550 (2012). 47, 70

[77] V. Meyer *et al.*, Nature **446** (2007). 48

[78] D. A. Abanin, P. A. Lee, and L. S. Levitov, Physical Review Letters **98** (2007). 48, 70

[79] M. Kharitonov, Phys. Rev. B **85**, 155439 (2012). 48

[80] Y. Barlas, K. Yang, and A. H. MacDonald, Nanotechnology **23**, 052001 (2012). 48

[81] J. Alicea and M. P. Fisher, Solid State Communications **143**, 504 (2007). 48

[82] J. Alicea and M. P. A. Fisher, Phys. Rev. B **74**, 075422 (2006). 48

[83] L. Sheng, D. N. Sheng, F. D. M. Haldane, and L. Balents, Phys. Rev. Lett. **99**, 196802 (2007). 48

[84] K. Nomura and A. H. MacDonald, Phys. Rev. Lett. **96**, 256602 (2006). 48

[85] K. Yang, S. Das Sarma, and A. H. MacDonald, Phys. Rev. B **74**, 075423 (2006). 48

[86] M. O. Goerbig, R. Moessner, and B. Douçot, Phys. Rev. B **74**, 161407 (2006). 48

[87] J. Jung and A. H. MacDonald, Phys. Rev. B **80**, 235417 (2009). 48

[88] J. G. Checkelsky, L. Li, and N. P. Ong, Phys. Rev. Lett. **100**, 206801 (2008). 48

[89] D.A. Abanin and L.S. Levitov, Science **317**, 641 (2007). 52, 53

[90] S. Matsuo *et al.*, Nature Communications **6**, 8066 (2015). 52, 68, 69, 127

[91] T. Giamarchi, *Quantum physics in one dimension*Internat. Ser. Mono. Phys. (Clarendon Press, Oxford, 2004). 57, 72, 77

[92] Y. V. Nazarov and B. M. Yaroslav, *Quantum transport: introduction to nanoscience* (Cambridge Univ. Press, Cambridge, 2009). 62, 63

[93] Y. Blanter and M. Büttiker, Physics Reports **336**, 1 (2000). 64

[94] E. Weisz *et al.*, Science **344**, 1358 (2014). 69, 83

[95] S. Ngo Dinh, D. A. Bagrets, and A. D. Mirlin, Phys. Rev. B **87**, 195433 (2013). 70

[96] J. Alicea and M. P. A. Fisher, Physical Review B **74** (2006). 70

[97] K. Nomura and A. H. MacDonald, Physical Review Letters **96** (2006). 70

[98] H. Fertig and L. Brey, Solid State Communications **143**, 86 (2007). 70

[99] I. V. Yurkevich, *Strongly Correlated Fermions and Bosons in Low-Dimensioanl Disordered Systems,* edited by I.V Lerner, B.L Althsuler, V. I Fal'ko, T. Giamarchi (Springer, 2002). 71

[100] K. Kang, Physical Review B **75** (2007). 83

[101] A. A. Vyshnevyy, A. V. Lebedev, G. B. Lesovik, and G. Blatter, Physical Review B **87** (2013). 83

[102] K. Kang and K. Ho Lee, Physica E: Low-dimensional Systems and Nanostructures **40**, 1395 (2008). 83

[103] K. Modi, A. Brodutch, H. Cable, T. Paterek, and V. Vedral, Rev. Mod. Phys. **84**, 1655 (2012). 83

[104] J. Maziero and R. M. Serra, International Journal of Quantum Information **10**, 1250028 (2012). 83, 92

[105] C. Zhang, S. Yu, Q. Chen, and C. H. Oh, Physical Review A **84**, 032122 (2011). 83, 92

[106] R. Auccaise *et al.*, Phys. Rev. Lett. **107**, 070501 (2011). 83

[107] I. A. Silva *et al.*, Phys. Rev. Lett. **110**, 140501 (2013). 83

[108] M. A. Nielsen and I. L. Chuang, Quantum computation and quantum information, 2000. 84, 86

[109] W. Zurek, Annalen der Physik **9**, 855 (2000). 85, 87, 88, 89

[110] J. V. Neumann, *Mathematical Foundations of Quantum Mechanics* (Princeton University Press, 1971). 86

[111] A. Wehrl, Rev. Mod. Phys. **50**, 221 (1978). 88

[112] A. Ferraro, L. Aolita, D. Cavalcanti, F. M. Cucchietti, and A. Acín, Phys. Rev. A **81**, 052318 (2010). 90

[113] B. Dakić, V. Vedral, and i. c. v. Brukner, Phys. Rev. Lett. **105**, 190502 (2010). 90

[114] B. Dakić *et al.*, Nature Physics **8**, 666 (2012). 91

[115] A. Streltsov and W. H. Zurek, Phys. Rev. Lett. **111**, 040401 (2013). 91, 128

[116] F. G. S. L. Brandão, M. Piani, and P. Horodecki, Nature Communications **6**, 7908 (2015). 91, 128

[117] C. Benedetti, A. P. Shurupov, M. G. A. Paris, G. Brida, and M. Genovese, Phys. Rev. A **87**, 052136 (2013). 92

[118] J. F. Clauser, M. A. Horne, A. Shimony, and R. A. Holt, Phys. Rev. Lett. **23**, 880 (1969). 92

[119] A. Aspect, P. Grangier, and G. Roger, Phys. Rev. Lett. **49**, 91 (1982). 92

[120] R. Auccaise *et al.*, Phys. Rev. Lett. **107**, 070501 (2011). 92